Fabrication and Optoelectronic Characterization of Nanoscale Resonance Structures

William Theodore Rieger Jr.

Dissertation submitted to the Faculty of the
Virginia Polytechnic Institute and State University
in partial fulfillment of the requirements for the degree of

Doctor of Philosophy
in
Physics

Jean J. Heremans, Chair
Xiaoting Jia
Mark Pitt
Victoria Soghomonian

March 24th, 2020
Blacksburg, Virginia

Keywords:Nanoantenna, Hot Carriers

Fabrication and Optoelectronic Characterization of Nanoscale Resonance Structures

William Theodore Rieger Jr.

(ABSTRACT)

Resonance structures have long been employed by RF and microwave devices ranging from antennas, to wave guides. These resonance structures have exhibited an enormous amount of control over the wavelength selectivity, polarization, and directivity of the electromagnetic radiation which couples to the structure. Traditional geometrical optics has alternatively used discrete optical components such as lenses, gratings, and polarizers to accomplish equivalent control over optical radiation. This dissertation contributes to the larger body of literature that applies lessons learned in RF and microwave resonance structures, to nanoscale resonance structures. Optoelectronic nanoscale resonance structures were fabricated and characterized using both experimental and numerical methods. Two nanoscale resonance structures were investigated: an antenna inspired Yagi-Uda array, and a metasurface inspired interdigitated structure. Experimental devices containing the nanoscale resonance structures were fabricated on semiconducting substrates forming metal-semiconductor-metal photodiodes. The spectral response of the nanoscale resonance photodiode was determined by measuring the photocurrent or photovoltage resulting from incident monochromatic light which was swept through wavelengths from 400 nm to 2000 nm. The previously mentioned Yagi-Uda based device exhibited two maxima in photoresponse at 1110 nm and 1690 nm. Effective wavelength scaling was applied to the Yagi-Uda nanoantenas, and consistency was demonstrated between the theoretical effective wavelength and experimental photoresponse maxima. The spectral response of the interdigitated structure demonstrated good qualitative agreement with the finite element modeled absorbance in an equivalent structure. Analysis of the modeled absorbance suggests that hot electron injection contributes to the photoresponse, and the spectral response of the detector device may be tuned by varying the geometrical parameters of the device. An optimized device was proposed that could improve photodetection efficiency using nanoscale resonance devices. Antenna inspired nanoscale resonance structures may be used to probe fundamental physical phenomena such as hot carrier generation, hot carrier transport, and surface plasmon resonances. Combined optical and electrical-optoelectronic devices exploiting these phenomena may be realized for a variety of applications, eliminating some or all of the discrete optical components required for optoelectronic systems and hence significantly reducing the SWaP cost of optoelectronic systems.

That this work received support from the U.S. Navy under Contract No. N68335-13-C-0184 and NASA under Contract No. NNX17CC63P.

Fabrication and Optoelectronic Characterization of Nanoscale Resonance Structures

William Theodore Rieger Jr.

(GENERAL AUDIENCE ABSTRACT)

Resonance structures have long been employed by RF and microwave devices ranging from antennas, to wave guides. These resonance structures have exhibited an enormous amount of control over radio waves. Traditional optics has alternatively used discrete components such as lenses, gratings, and polarizers to accomplish equivalent control over light waves. This dissertation contributes to the larger body of literature that applies lessons learned in RF and microwave resonance structures, to nanoscale resonance structures. Optoelectronic nanoscale resonance structures were fabricated and characterized using both experimental and computational methods. Two nanoscale resonance structures were investigated: an antenna inspired Yagi-Uda array, and a metasurface inspired interdigitated structure. The ability of both devices to detect light of a particular wavelength was then tested. The photoresponse of the device containing a Yagi-Uda array is consistent with RF Yagi-Uda antennas when considered in accordance with the concept of effective wavelength. The experimental response of the interdigitated structure demonstrated good qualitative agreement with the computational modeled absorbance in an equivalent structure. Analysis of the modeled absorbance suggests that the spectral response of the detector device may be tuned by varying the geometrical parameters of the device. An optimized device was proposed that could improve photodetection efficiency using nanoscale resonance devices. Antenna inspired nanoscale resonance structures may be used to probe fundamental physical phenomena such as hot carrier generation, hot carrier transport, and surface plasmon resonances. Combined optical and electrical-optoelectronic devices exploiting these phenomena may be realized for a variety of applications, eliminating some or all of the discrete optical components required for optoelectronic systems and hence significantly reducing the SWaP cost of optoelectronic systems.

Dedication

To my family.

Acknowledgments

Over the past 6 years I have received support from a great number of people. First and foremost, I would like to acknowledge Dr. Jean J. Heremans who has been a great advisor, mentor, colleague, and friend. I would like to thank my dissertation committee members, Dr. Xiaoting Jia, Dr. Mark Pitt, and Dr. Victoria Soghomonian, for their support throughout my graduate education. I would like to specifically thank Dr. Jean J. Heremans and Dr. Victoria Soghomonian for their encouragement and support during my first two years at Virginia Tech when my academic future seemed uncertain. I am especially thankful for the flexibility demonstrated by all members of my dissertation committee, the Physics Department, and the Graduate School allowing me to defend my dissertation without delay despite the ongoing COVID-19 pandemic. I would like to thank my colleagues in the measoscopic physics group, Dr. Shaola Ren, Dr. Yuantao Xie, Zijian Jiang, and Adbhut Gupta. I would like to thank Tigran Asryan for his contributions to ongoing modeling efforts. I would also like to acknowledge my mentors and colleagues at NanoSonic Inc., Dr. Hang Ruan, Dr. Yuhong Kang, Dr. Richard Claus, Elizabeth Gladwin, and Michelle Homer. I would like to thank Amanda Hammett for her ongoing love and support. Finally, I would like to thank my parents, William Rieger Sr. and Mary Rieger for the great many personal sacrifices they have made so that both of their children could receive the highest quality of education.

Contents

List of Figures

List of Tables

Chapter 1

Introduction

Nanoscale resonance structures have been of interest since the development of nanofabrication techniques has allowed experimental realization of structures with characteristic length scales equal to an optical wavelength [1–5]. Nanoscale resonance structures fit broadly into two categories: subwavelength nanoantennas [6–26], and metasurfaces which consist of subwavelength structures [27–29]. Nanoantennas offer to apply lessons learned in RF and microwave antennas to optical wavelengths [12–26]. Even the concept of impedance matching can be applied to nanoantennas [30]. RF and microwave antennas offer control of directivity, polarization, and wavelength selectivity while operating at high efficiencies [31]. Equivalent control of directivity, polarization, and wavelength selectivity in optics currently requires a system of discrete optical components such as lenses, polarizers, and filters [32]. Innovations such as fiber optic communication, LIDAR, and satellite imagery require optoelectronic devices with reduced size, weight, and power (SWaP) costs [33]. Nanoantennas such as the Yagi-Uda nanoantennas studied in this dissertation show promise to reduce the SWaP cost of optoelectronic devices as discussed below. Metasurfaces are periodic surfaces, consisting of a unit cell containing subwavelength features [34, 35]. Metasurfaces offer control over macroscopic physical properties such as the index of refraction, by controlling the geometry in the unit cell [3, 27, 36–43]. Such surfaces have been demonstrated at RF and optical wavelengths [3, 27, 34–43]. The interdigitated device discussed in this dissertation is metasurface inspired. Nanoscale resonance structures have been primarily investigated through purely optical techniques, where the nanoscale resonance structure is placed between a light source and detector [6, 8, 12, 15, 17–22, 26]. The reflectance, transmittance, and absorbance may be measured through purely optical methods. Practical use of nanoscale resonance structures is based on the ability of these nanoscale structures to confine electric or magnetic fields [44]. Confined electromagnetic fields may be used

(1) to produce an electrical response as exploited in this dissertation,

(2) to interact with an object in a highly localized way such as is used in scanning tunneling

microscopy [45, 46],

③ or to catalyze a chemical reaction [47, 48].

There are two main difficulties in applying lessons learned in RF and microwave structures to nanoscale resonance structures: the material properties of the nanoscale resonance structure and surrounding material play a significant role in antenna behavior, and the necessity to develop new ways to interact with the antenna due to the length scales involved. RF and microwave antennas allow oscillating electric currents to exist in antenna elements which are typically made of metal wire lengths [31]. These oscillating electric currents couple to traveling electromagnetic waves. If the skin depth in the metal antenna element is much smaller than the radius of the wire cross section, then the coupling between oscillating currents and traveling waves can be analytically deduced by approximating the antenna elements as one dimensional perfect conductors [31]. This approximation results in a wavelength scaling which is only dependent on the free space wavelength. The skin depth at typical RF and microwave wavelengths (of order 0.1 µm - 10 µm in copper) is much shorter that the cross sectional radius of the wire in standard cases (406 nm µm for 20 gauge wire) [31]. However, the skin depth at optical frequencies (25 nm to 45 nm in Au [49]) is not negligible relative to the cross sectional radius of the nanoantennas investigated in this dissertation (25 nm). As a result of the non-negligible skin depth, the scaling of resonance wavelength with free space wavelength fails. In nanoscale resonance structures, conduction electrons oscillate in or on the surface of the metal structure, and are called plasmons [50, 51]. The specific behavior of plamsons in a nanoscale resonance device is dependent on both the structure geometry and materials properties [52]. Plasmons occurring at a metal-dielectric interface are called surface plasmons. Because the electric field associated with a surface plasmon extends into both the metal and dielectric, the permittivity of both materials affect the plasmon behavior. There are two types of surface plasmons that are of particular importance to nanoscale reasonance structures: Surface Plasmon Waves (SPW) and Localized Surface Plasmons (LSP). Surface plasmon waves [50, 51] exist on a metal-dielectric interface which has a characteristic length scale larger than the plasmon wavelength (Fig. 1.1a). Localized surface plasmons exist on subwavelength nanostructures such as nanospheres or nanorods [44], and are depicted in Fig. 1.1b. The Yagi-Uda nanoantennas discussed below support LSP modes. The interdigitated structure discussed in Chapter 5 supports LSP or SPW depending on the frequency of incident light. The main thrust of this dissertation is fabrication and characterization of antenna inspired nanoscale resonance structures to probe fundamental physical phenomena such as hot carrier generation, hot carrier transport, and surface plasmon resonances, and to realize combined optical and electrical-optoelectronic devices exploiting these phenomena for a variety of applications.

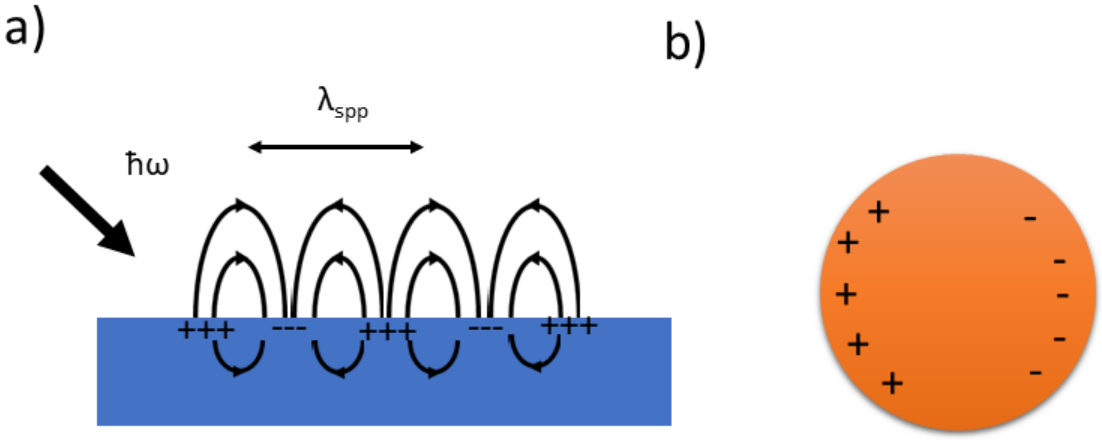

Figure 1.1: Two types of surface plasmons: a) A surface Plasmon Wave (SPW) on an infinite metal-dielectric interface. Black lines denote electric field. b) A Localized Surface Plasmon (LSP) on a metal nanosphere. (Figure inspired by [53]).

1.1 Applications

Optical nanoscale resonance structures have been used extensively for chemical and biological sensing applications [54, 55]. Additionally, nanoscale resonance structures have been used as beam steers [22, 28, 56]. Potential optoelectronic uses for nanoscale resonance devices are widespread and are largely focused on bringing the level of control achieved in RF and microwave structures to optical wavelengths. Current optoelectonic systems which achieve a level of control comparable to RF and microwave antennas require discrete optical components such as lenses, polarizers, and detectors made from exotic materials such as PbSe, PbS, InGaN, and GaN [32, 57, 58]. The key advantage of nanoscale resonance structured optoelectronic devices is the relaxation of the requirements for material properties (i.e. electronic band structure), and the increased control of polarization, selectivity, and directivity [26, 59, 60]. Energy harvesting devices are a specific area that would benefit from nanoscale resonance optoelectronic devices [61, 62]. Semiconductor energy harvesting devices are able to collect photons with energy equal to or greater than the band gap energy of the semiconductor. The nanoscale resonance optoelectronic devices presented in Chapter 5 of this dissertation rely on hot carrier injection to generate electrical energy from photons. The energy of photons collected through hot carrier injection is dependent on the height of the Schottky barrier formed at the interface of the metal nanoscale resonance structure, and the semiconducting substrate. The Schottky barrier can be tuned through selection of materials or doping [63]. The process of energy harvesting through hot carrier injection is elaborated in Section 1.2.2. The applications of nanoscale resonance structures are vast and not limited to optoelectronic detection devices discussed in this dissertation. For example, nanoscale resonance structures have been demonstrated as photonic sources when driven

electrically [64,65]. Nanoresonant structures have been used to replace traditional antireflection coatings [66], to replace traditional lenses with flat lenses [28,60], or to couple light to detectors via creation of a cavity [67,68]. Nanoscale resonance structures may also be used as waveguides, making photonic integrated circuits possible [69].

1.1.1 Efficiently Harvesting Energy

Optoelectronic nanoscale resonance devices have the possibility to increase efficiency of energy harvesting devices by broadening the bandwidth to which a photodiode is sensitive [24,62,70]. Commercial photovoltaic devices require the excitation of an electron hole pair in an intrinsic semiconductor, and thus the optical bandwidth to which they are sensitive is limited by the electronic band structure of the semiconductor [62]. Alternatively, nanoscale resonance structure based energy harvesting devices such as those investigated in this dissertation collect energy through hot carrier injection, and are hence able to collect energy from photons with energies below the band gap energy of the semiconducting substrate [61]. The lowest energy photon a hot carrier injection based energy harvesting device can collect is equal to the height Schottky barrier at the interface of the metal nanoscale resonance structure, and the semiconducting substrate. More efficient energy harvesting may be achieved by combining hot carrier injection with intrinsic electron hole pair production [61,62]. Increasing the efficiency of nanoscale resonance optoelectronic energy harvesting devices can be accomplished by increasing the efficiency of optical absorbance from surface plasmon resonance [15–22] (discussed in Section 1.3), or by more efficiently generating hot carriers [61,62,71] (discussed in Section 6.2). Further improvements to both the quantum and overall efficiencies of nanoscale resonance structure based devices benefits from focusing on efficiently generating hot carriers, and efficiently transporting them across a metal semiconductor interface. The future modeling work proposed in Section 6.1 addresses both of these potential improvements pathways.

1.1.2 Polarization, Selectivity, and Directivity Control

RF and microwave antennas and resonance structures (i.e. waveguides) are often designed to have an optimized response to a particular polarization, wavelength or directivity [72]. However, in optics, it is often necessary to use lenses, gratings, apertures, and exotic materials to accomplish an equivalent response [32]. Nanoscale resonance structure based optoelectronic devices can realize polarization, wavelength selectivity, and directivity intrinsically through careful control of the structure geometry. Directivity and wavelength selectivity are realized in Yagi-Uda nanoantennas [15–23], and have been observed in the optoelectronic nanoantennas presented in this thesis. The intrinsic control of polarization, wavelength selectivity, and directivity allow applications traditionally requiring a system of discrete optical components to be realized on a chip [73,74]. Based on my dissertation work, as an example I

propose a spectrometer on a chip. A standard spectroscopy system requires as a minimum a light source, a slit, a diffraction grating, and an angularly resolved photodetector as seen in Fig. 1.2a. Alternatively, my proposed spectrometer on a chip is shown in Fig. 1.2b. A white light source and an array of nanoscale resonance structures are fabricated on a single semiconductor substrate; the nanoscale resonance structure array eliminates the need for both the diffraction grating, and the angularly resolved photodetector. Over one hundred

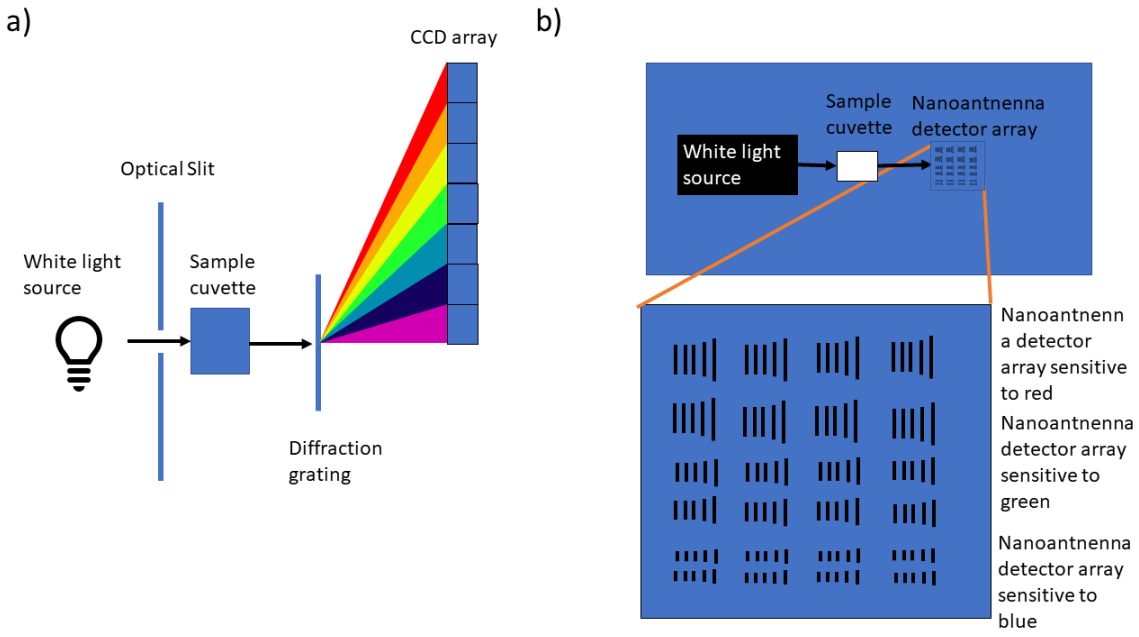

Figure 1.2: Schematic representation of nanoscale resonator based spectrometer on a chip. a) A standard spectrometer setup including a light source, cuvette, optical slit, diffraction grating, and sensor array. b) The proposed spectrometer on a chip where the requirements consist of only the device and sample cuvette.

years ago, Wood reported observation of light transmitted through sub wavelength slits in a metallic optical grating [1]. Enhanced transmission though subwavelength apperatures in metal films has since been observed [75]. The far reaching implications of the anomalous behavior originally reported by Wood was not fully realized until it was understood that the anomalous behavior in metallic grating emerges from surface plasmon resonance [76]. In addition to subwavelength apertures, surface plasmon resonance also occurs in subwavelength nanostructures, such as metal nanorods or nanoparticles [4, 8, 55]. Nonlinear optical effects can be observed using arrangments of metal nanorods to double or triple the frequency of incident light [22, 77–79]. Photodetectors using frequency doubling have been demonstrated in the mid and long IR range [79]. Plasmonic antenna behavior has been observed in sodium chains [80]. Additionally, nanoantennas have been realized in heavily doped Si [81], and bear similarities to the metallic nanoantennas studied in this dissertation.

1.1.3 Optical Measurements and Geometries

The largest collection of literature on the topic of nanoscale resonance structures is focused on purely optical measurements [15–22]. Purely optical measurements offer the simplest way to examine nanoscale resonance structures. Moreover, purely optical techniques have been used to optimize surface plasmon resonance in nanoscale structures. A possible experimental setup for transmittance and reflectance measurements is shown in Fig. 1.3. The nanoscale resonance structures are fabricated on a transparent substrate. The sample containing the resonance devices is placed on an integrating sphere for transmittance (Fig. 1.3a) or reflectance (Fig. 1.3b) measurements. The absorbance may be computed from the experimental transmittance and reflectance values by using conservation of energy.

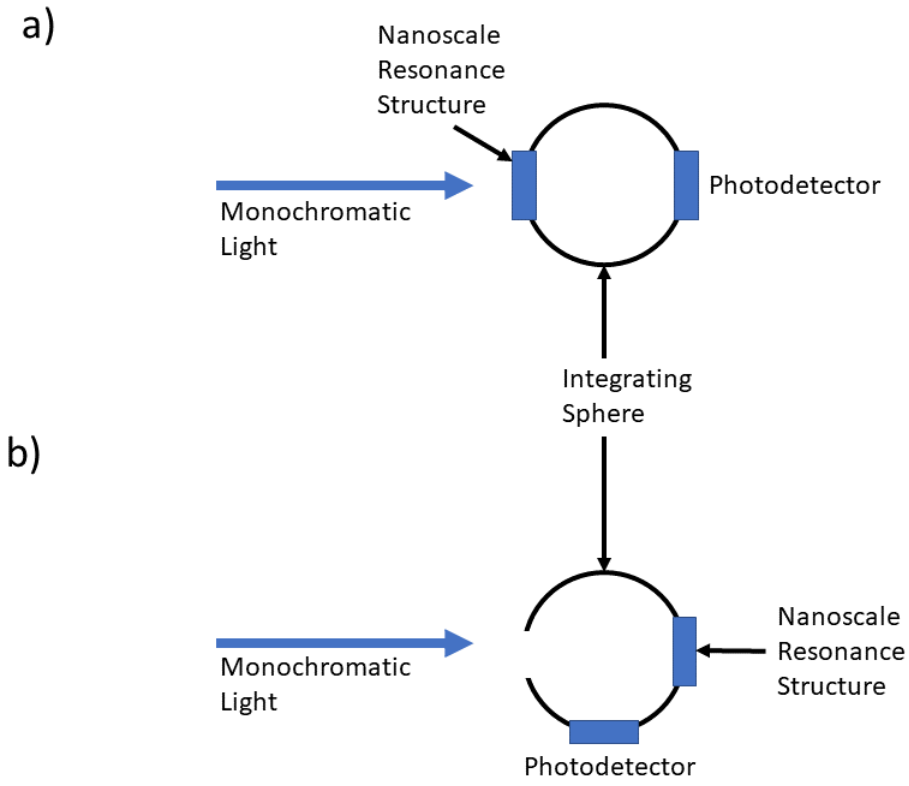

Figure 1.3: Possible experimental setup to measure a) transmittance, and b) reflectance. The sample of resonance structures on a transparent substrate is placed on an integrating sphere along with a photodetector. The integrating sphere collects light that is reflected from the sample at any angle.

Grating Structure

Optical gratings are frequently used to diffract light into angularly resolved monochromatic light. Evidence of the first surface plasmon resonance in the form of Wood's anomaly was originally observed over one hundred years ago [1]. Since then, gratings have been used in plasmonic structures to enable coupling between surface plasmons and free space photons when a momentum mismatch exists [82, 83]. The grating-like structure investigated in this dissertation consists of two interdigitated comb-like structures as described in Chapter 2, and is inspired by geometries used in the THz portion of the spectrum [84–93].

Yagi-Uda Nanoantenna

Yagi-Uda antennas are commonly used for high gain applications because they exhibit strong polarization, directivity, and wavelength selectivity [31]. Yagi-Uda nanoantennas are also well suited to monolithic nanofabrication techniques, making them a popular design choice for nanoantennas [15–23]. Yagi-Uda antennas consist of a single detector/driving element, one or more reflectors, and one or more directors [31]. Yagi-Uda nanoantennas have been well characterized optically [15–22]. An experimental optoelectronic characterization of Yagi-Uda nanoantennas is discussed in Chapter 5, and optoelectronic measurements are described in Section 1.2.2.

1.1.4 Optoelectronic Measurement

Optoelectronic measurements in the literature make use of hot carrier injection to generate a photoresponse in one of two ways. A metal-semiconductor-metal (MSM) photodiode with nanostructured electrodes has been shown to have a photoresponse dependent on the nanostructure [7, 29, 94–100]. Alternatively, a method has been demonstrated where nanoscale resonance structures are sandwiched between a transparent conductor and semiconductor [42,61,62,101,102]. In the sandwiched method, a single Schottky barrier is formed at the metal-semiconductor interface and an ohmic contact is made to the semiconductor and the metal. Hot electrons can overcome the Schottky barrier and cause a measurable photocurrent. Both methods are shown in Fig. 1.4.

1.1.5 Surface Plasmon Polariton Background and Definitions

The ensuing discussion of Surface Plasmon Polaritons is heavily inspired from the seminal reports Zayats *et al.* [50] and Pitarke *et al.* [51].

The nanoscale optoelectronic devices investigated in this dissertation are based on surface plasmon polaritons (SPP) and hot carrier injection [3,27]. SPP are composite quasi-particles

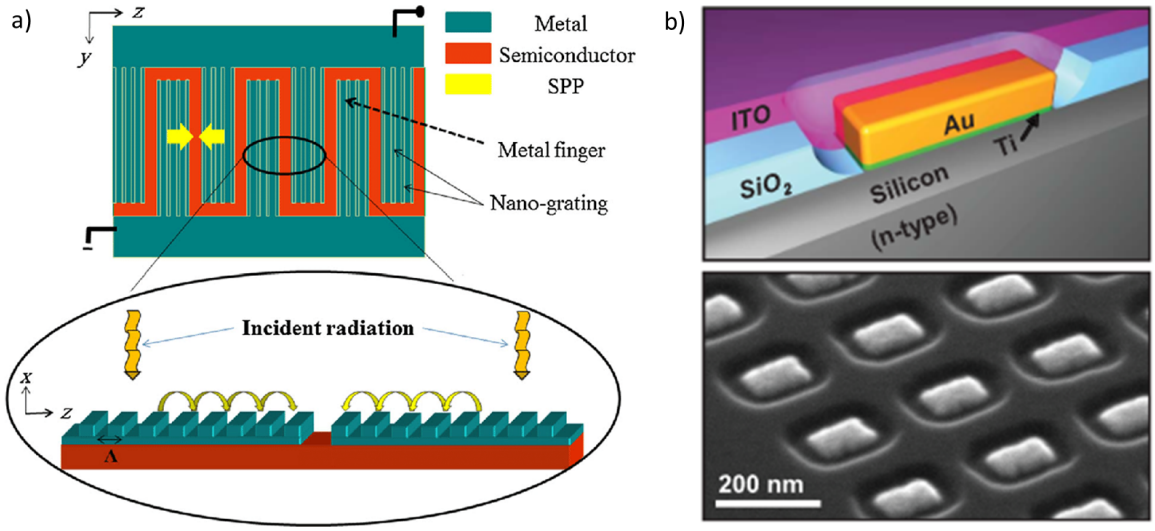

Figure 1.4: Two optoelectronic methods used in the literature. a) A periodic structure is presented on MSM photodiode electrodes, modified from [94], where the periodic structuring influences the observed photocurrent. b) Schematic depiction of sandwiched optoelectronic device consisting of an ITO coated Au nanoantenna on an Si substrate (top), and SEM micrograph of an array of these sandwiched antennas (bottom), modified from [61].

consisting of a coupled surface plasmon and a photon. Hot carrier injection occurs when a hot carrier is first excited, via a concentrated electric field existing in the nanoscale resonance structure, and then injected across a Schottky barrier formed at the interface of the metal resonance structure and a semiconductor substrate [62].

Surface Plasmon Polariton Defined

Surface plasmons are electromagnetic waves that exist at a conductor-dielectric interface [50, 51]. These may exist as surface plasmon waves (SPW) such as in Fig. 1.1a. or localized surface plasmons (LSP) such as in Fig. 1.1b. A uniform infinite plane interface has a continuum of possible plasmon excitations. In an optoelectronic nanoscale resonance structure it is not the surface plasmons themselves that are important, but rather the coupling that exists between the surface plasmon and another particle or quasi-particle. For example, transmission maxima have been observed in Au coated glass [103] where there are three coupling effects that are important:

- Photon-surface plasmon coupling at top air-gold interface
- Surface plasmon-surface plasmon coupling between top and bottom interface
- Surface plasmon-photon coupling at bottom glass-gold interface.

The first and last of these couplings are in a class of couplings called surface plasmon polaritons (SPP) and are of primary importance to the work presented in this dissertation. (See for example Chapter 5). Surface plasmon-surface plasmon coupling is of lesser importance for photodetection; however the role of surface plasmon-surface plasmon interactions in suppressing or enhancing surface plasmon resonance is important to the development of resonance devices. Appendix A has a derivation of the conditions for the existence of a surface plasmon polariton on an infinite metal-dielectric interface [50, 51].

Surface Plasmon Polariton Geometry Effects

Surface plasmon resonance (SPR) is strongly dependent on the geometry of the nanoscale resonance structure. The relationship between geometry and SPR is what makes it possible to realize strong wavelength selectivity, polarization and directivity in nanoscale resonance structures. Introducing a periodic structure to an infinite metal-dielectric surface causes a band gap in the SPP dispersion [3, 27]. The interdigitated device investigated in Chapter 5 of this dissertation is inspired by band gaps originating from a periodic surface.

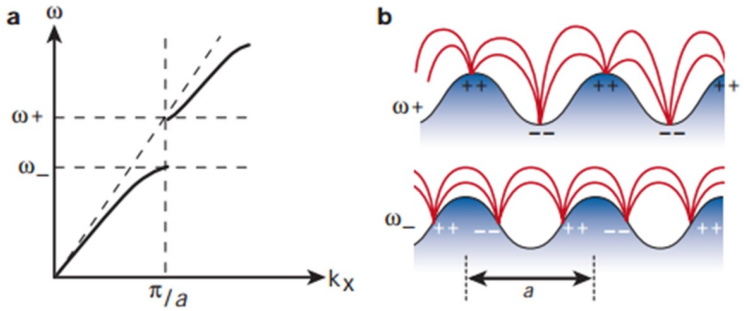

Figure 1.5: Periodic structure leading to the rise of a band gap in the surface plasmon polariton (SPP) dispersion. a) SPP dispersion on a corrugated metal-semiconductor interface. b) Surface geometry, and electrical field lines (red) of two resonance modes ant the upper and lower band edge. Reproduced with permission from [3]

1.2 Optoelectronic Characterization Method

This dissertation presents a novel optoelectronic characterization method for nanoscale resonance structures. As discussed earlier, previous nanoantenna optolectronic devices are complex, requiring multiple processing and alignment steps. Photodetectors based on nanoscale resonance structures utilize hot electron injection to provide a measurable photoreponse. The process for generating, transporting, and collecting hot carriers into a photoresponse

is multi-step, and there is the potential to optimize each step, creating a class of efficient next generation nanoscale resonance devices. SPR causes locally high electromagnetic fields to exist in and around resonance structures. Hot carriers are generated when concentrated electric fields in the nanoscale resonance structure excite a carrier (electron or hole) into a more energetic state in the conduction band [104]. The newly generated hot carrier has an initial momentum, and propagates through the metal structure until it is incident on a surface or a scattering event occurs. The occurrence of a scattering event such as electron-electron scattering or electron-phonon scattering will change the hot carrier state through exchanging energy and momentum. If the newly scattered carrier is still hot, it will continue to propagate until ultimately it is incident on a surface of the nanoscale resonance structure. If the hot carrier is incident on the surface where the resonance structure contacts the semiconductor substrate, and has sufficient energy to overcome the Schottky barrier then it contributes to the photoresponse. The energy required for hot electron generation/injection is a function of the resonator geometry as well as the Schottky barrier height between the semiconductor and metal. Application of this optoelectronic characterization method to nanoscale resonance structures probes fundamental physical phenomena such as hot carrier generation, hot carrier transport, and surface plasmon resonances. Further, combined optical and electrical-optoelectronic devices may be realized that exploit these phenomena for a variety of applications.

Chapter 2

Fabrication

The nanoscale optoelectronic resonant devices discussed in this dissertation are fabricated using standard nanofabrication processes, and are delineated in detail in the various sections of Chapter 2.

2.1 Photolithography

Device fabrication requires subjecting a particular region of a wafer to processes. The region of the wafer to be processed may yield a complex pattern. If the smallest feature size of the pattern is larger than approximately 1 μm, photolithography is the standard method to transfer the pattern to the wafer; smaller feature sizes require shortened wavelength lithographies of which electron beam lithography is one (discussed in the next section). A typical positive photolithography process (Fig. 2.1) begins by spin coating a photosensitive polymer (photoresist) onto the wafer. Spin coating is a process where a viscous liquid, in this case photoresist polymer, is poured onto a wafer, and the wafer is rotated about an axis normal to the surface so that a uniform thin layer of the viscous liquid remains. This results in a uniform layer of photoresist on the entire wafer surface, as depicted in Fig. 2.1b. The photoresist layer thickness varies depending on the specific photoresist and spin speed, but is typically on the order of a few μm. The photoresist coated wafer is then baked to remove the solvent, leaving a crosslinked polymer layer. A mask, which consists of an opaque (Cr or FeO_x) pattern on a glass plate is placed over the wafer as shown in Fig. 2.1c. The masked wafer is then exposed to an ultraviolet light source. The areas of the photoresist not covered by the opaque part of the mask undergo a photochemical response whereby the crosslinking is broken. The wafer is then removed from the light source, and soaked in a developer (typically a weak base) which selectively dissolves the photoresist in areas where the crosslinking has been broken. The final result is a wafer that is partially coated with a protective photoresist layer which is a copy of the mask used. The exposed area of

the wafer may be processed, leaving the unexposed area unaffected. After the processing step, the photoresist is removed by dissolution in a solvent, or plasma etching. A negative photolithography process instead forms an inverted copy of the mask.

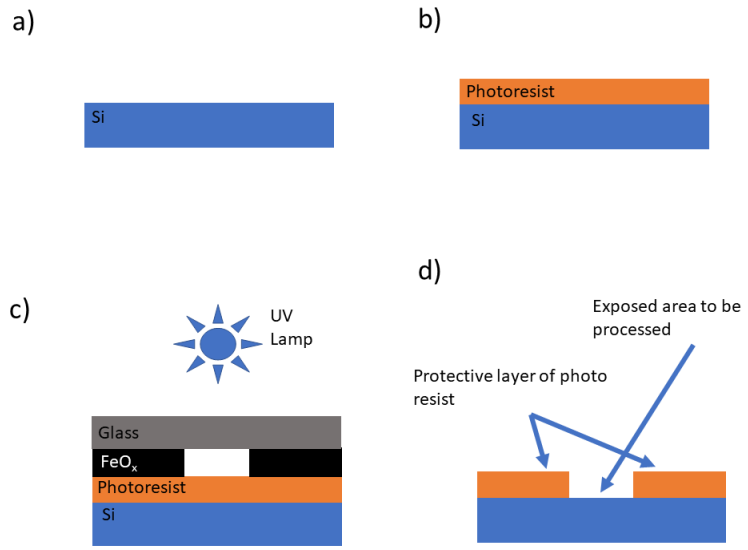

Figure 2.1: Main steps in a typical photolithography process. a) A clean and dry wafer ready for photolithography. b) Wafer with a uniform photoresist layer which has been baked to remove solvent. c) Typical photolithography exposure: the masked wafer is placed under an ultraviolet light source. d) The wafer after completion of the photolithography process. The wafer is selectively covered in a protective photoresist layer in a pattern identical to the mask used.

2.2 Electron-beam Lithography

When sub-micron feature sizes are required, it is necessary to use electron beam (e-beam) lithography rather than photolithography. A typical e-beam lithography process begins by spin coating a wafer with an e-beam resist in a similar manner as done with a photoresist. The e-beam resist coated wafer is then baked to remove the solvent, leaving a uniform layer as shown in Fig. 2.2b. The wafer is then placed in a scanning electron microscope (SEM) for e-beam exposure as depicted in Fig. 2.2c. The exposure differs from photolithography in that a direct writing procedure is used instead of a mask. In typical scanning electron microscopy for imaging an electron beam is rastered across the entire sample from left to right and top to bottom. Sweeping motion is driven by a system of beam steering coils as pictured in Fig. 2.2c. The beam steering coils provide a variable magnetic field, which steers the electron beam via the Lorentz force. Direct writing is accomplished by controlling these coils with

a computer program which reads a two-dimensional Computer Aided Drawing (CAD) file, and scans the electron beam over only a portion of the wafer according to the CAD file. The computer also controls a beam blanker that blanks and unblanks the electron beam to provide an exact electron dose for each exposed pixel. Exposure to the electron beam breaks crosslinking in the e-beam resist in a similar manner to ultraviolet light in photoresist. E-beam resist that has been exposed is dissolved in a developer, with the unexposed e-beam resist left intact. The majority of the patterns produced in this work were fabricated using a solution of polymer chains of polymethyl methacrylate (PMMA) (molecular weight of 950 kg/mol in a 3% by weight solution of chlorobenzene) as e-beam resist. In this case, the electrons break the long polymer chains. The shorter chains have increased solubility in the chosen developer, which is a mixture of methyl isobutyl ketone and isopropanol. Another e-beam resist used in related work was ZEP520A, a high-resolution resist formulated to show higher dry-etching resistance than PMMA. The final result is a wafer selectively covered in a protective layer of e-beam resist that may be processed further by etching or deposition as depicted in Fig. 2.2d.

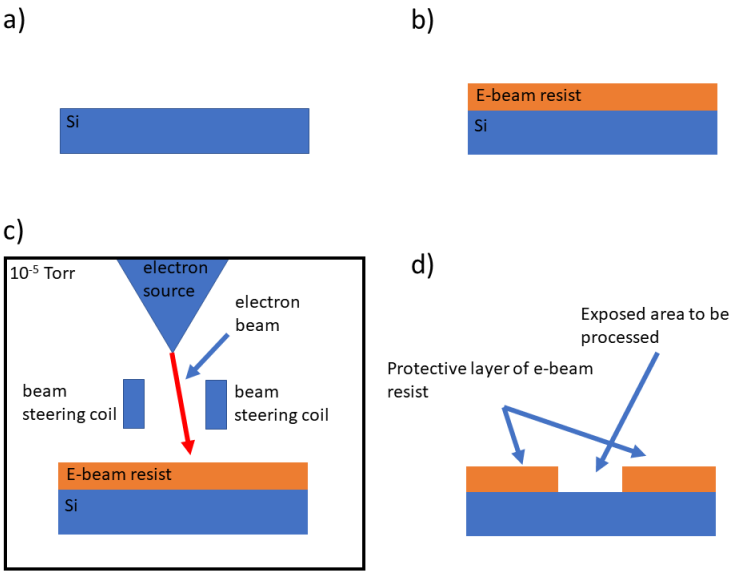

Figure 2.2: Main steps in a typical electron beam lithography process. a) A clean and dry wafer ready for electron beam lithography. b) Wafer with a uniform electron beam resist layer which has been baked to remove solvent. c) Typical electron beam exposure: the wafer is selectively exposed by driving the beam steering coils with e-beam lithography software. d) The wafer after completion of the electron beam lithography process. The wafer is selectively covered in a protective electron beam resist layer identical to the CAD file used during exposure.

Because e-beam lithography is optimized for high resolution patterns consisting of sub-micron features, it is often necessary to combine e-beam lithography with photolithography. Photolithography may be used to pattern macroscopic features, such as solder pads, and

e-beam lithography to pattern finer features, such as nanoantennas. A multi-step process requires the use of an alignment technique. The alignment technique used for e-beam lithography in this dissertation works by opening windows where the electron beam is rastered (hence the e-beam resist is inadvertently exposed) away from the active writing area. Figure 2.3 outlines this process. First, a two layer CAD drawing is constructed, with each layer containing a window, and an outline of an alignment mark as shown in Fig. 2.3a. Then, photolithography is used to define large features of the device; this includes features which will be used in the alignment process. The features used in the alignment process may be dedicated alignment marks, or device features such as macroscopic solder pads. Figure 2.3b shows example alignment marks. After the photolithography process, the wafer is prepared for e-beam lithography and placed in the SEM. The e-beam lithography software first opens the alignment CAD file, and rasters the electron beam according to the windows defined in the file. The user then uses the arrow keys on the computer running the lithography software to bring the alignment marks and the outline on the screen together as shown in Fig. 2.3c. The final, aligned result is shown in Fig. 2.3d. The e-beam lithography software calculates a transformation (translation and rotation) matrix, whereby the direct writing coordinates are transformed to write the pattern in the correct position and orientation relative to the alignment marks.

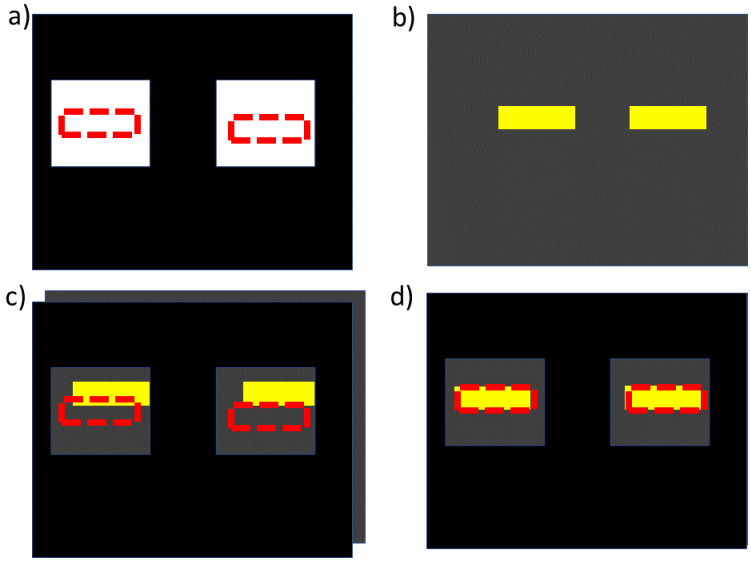

Figure 2.3: Overview of electron beam alignment procedure. a) Two layer CAD file with windows (in white) and alignment mark outlines (red dashed lines). b) Substrate (grey) with alignment marks (yellow). c) Initial view of substrate through windows as seen in the e-beam lithography software. d) Final aligned image, used by the e-beam software to perform coordinate transform that will be used to write pattern in the correct position and orientation relative to the alignment marks.

2.3 Thermal Evaporation

Thermal evaporation is a method whereby material, such as elemental metals, are deposited as a thin uniform film on a substrate. This process, along with either photolithography or e-beam lithography is used in this dissertation to produce a patterned metallic layer on a substrate. Thermal evaporation is accomplished by heating the material to be deposited until it melts and boils or sublimes; vapors from the material to be deposited then condense fairly uniformly on the substrate. Thermal evaporation must be performed in a vacuum chamber. The thermal evaporation processes used in this dissertation took place at pressures below 10^{-6} Torr. The material to be deposited is in a crucible at the bottom of the vacuum chamber. There are two standard methods to heat the material to be deposited—by forming the crucible into a filament (this is depicted in Fig. 2.4), and passing a heating current through the filament, or by directing a high energy electron beam into a grounded crucible. Filament evaporators are suitable for materials with low melting temperatures, but e-beam evaporators must be used for materials requiring higher temperatures. The typical thermal evaporation process is shown in Fig. 2.4. First the material to be deposited is placed in the crucible, and the wafer is loaded into the low pressure chamber as shown in Fig. 2.4a. The low pressure chamber is evacuated. The crucible is then heated until the material to be deposited melts as seen in Fig. 2.4b. The material is heated further until it's vapor pressure is sufficiently high for a thin film to be deposited on a substrate as depicted in Fig. 2.4c. Some materials directly sublime from the solid state. Figure 2.4d shows the final result, with a uniform layer of material deposited on the substrate.

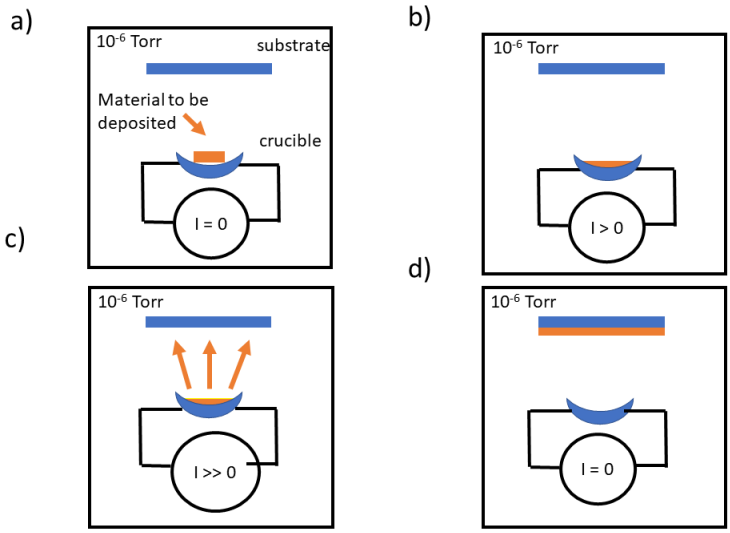

Figure 2.4: Main steps in a typical thermal evaporation process. a) the substrate (blue) and material to be deposited (orange) are loaded into the low pressure chamber, and the chamber is evacuated. b) The crucible is heated until the material to be deposited melts. c) The crucible is heated more until the material to be deposited boils. d) The material do be deposited condenses to form a uniform layer on the substrate.

2.4 Total Process

The typical process for fabricating an optoelectronic nanoscale reasonant device is outlined below and is shown in Fig. 2.5.

- A 5mm x 5mm piece was cleaved from an n-type 1-10 Ω/cm Si <100>wafer which was coated with a 1000 Å protective thermally grown oxide (Fig. 2.5a).
- The wafer piece was cleaned in 6:1 Buffered Oxide Etch (BOE) for 10 min to remove the protective oxide layer (Fig. 2.5b).
- The Si piece was confirmed to be hydrophobic, indicating the oxide layer was completely removed.
- maP1210 photoresist was then spun on to the Si wafer piece for 30 seconds at 3000 rpm.
- The photoresist was baked for 30 min at 100°C (Fig. 2.5c).
- The photoresist coated wafer was covered with a photomask exposing a pattern which will become the macroscopic electrodes.
- The masked sample was exposed to the UV light source for 4 seconds, and developed for 30 seconds in 1:8 MicroChem 303A developer:DI water (Fig. 2.5d).
- Thermal evaporation was used to deposit 10 nm Cr and 50 nm of Au on the sample (Fig. 2.5e).
- The excess metal is lifted off by soaking overnight in acetone, and gentle sonication (Fig. 2.5f).
- PMMA with a molecular weight of 950 kg/mol in a 3% by weight solution of chlorobenzene is spun on to the wafer piece at 7000 rpm for 40 sec.
- The sample is then baked for 5 hours at 160°C (Fig. 2.5g).
- Electron beam lithography is performed following an alignment procedure as outlined in the preceding section (Section 2.2).
- The sample is developed in 3:1 IPA:MIBK for 70 sec and rinsed in IPA for 40 sec (Fig. 2.5h).
- 10 nm Cr and 50 nm Au are deposited on the substrate using thermal evaporation (Fig. 2.5i).
- The excess metal is lifted off using the same procedure as before, but taking extra care to prevent damage to small features (Fig. 2.5j).

- Au wires are physically and electrically attached to the macroscopic electrodes using H20E EPO-TEK silver epoxy, and then baked at 105°C for 3 hours (Fig. 2.5k).
- The completed device was attached to a DIP header with a small amount of vacuum grease.

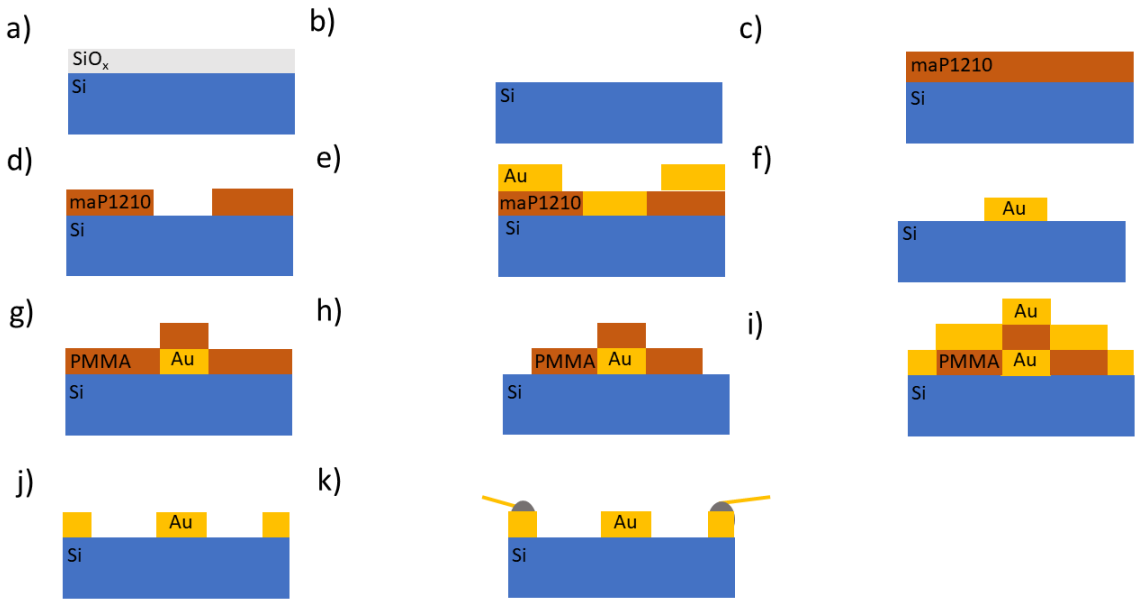

Figure 2.5: An overview of the typical fabrication process for a nanoscale resonant opto-electronic device. a) A 5mm x 5mm wafer piece with protective coating. The wafer piece after: b) soaking in BOE to remove oxide, c) coating with photoresist, d) photolithography to define macroscopic electrodes, e) thermal evaporation of Cr/Au, f) first lift off, g) coating with e-beam resist, h) e-beam lithography to define nanoscale details, i) second thermal evaporation of Cr/Au, j) second lift off, k) attaching Au wires with silver epoxy.

Chapter 3

Characterization Method

The characterization method employed in this dissertation places the nanoscale resonant structures, which are to be studied, on an optoelectronic device for characterization. This method is the result of combining two existing methods—an optoelectronic method using a multilayer heterostructure, and a standard metal-semiconductor-metal (MSM) photodiode. The former has shown promise to increase the efficiencies of both solar power generation and optical photodetectors by allowing collection of photons below the band gap energy of the semiconductor substrate [61]. The existing multilayer heterostructure method is based on hot carrier injection which produces an electronic photoresponse. Hot carrier injection is the mechanism used in this dissertation as well, but a simpler scheme for the collection of hot carriers into a measurable photocurrent is used. This simplification is inspired by the MSM photodiode. Standard MSM photodiodes are monolithic metal structures on the surface of semiconductor substrates. Often the metallic monolayer consists of two interdigitated comb structures as depicted in Fig. 3.1a, but the interdigitated structure is often of a period much longer then an optical wavelength. The MSM photodiode consists electrically of two back to back Schottky diodes. This gives an IV characteristic as shown in Fig. 3.1b. The two Schottky diodes of each device fabriated in this thesis are identical. During measurements, one of the Schottky diodes is forward biased and the other is reverse biased. At bias of 1 V DC, such as is used in the Yagi-Uda device measurements, the applied voltage is higher than the built in voltage of the diodes, but is not high enough to cause complete breakdown in the reverse biased diode.

If the MSM photodiode is exposed to light, the IV curve changes as seen in Fig. 3.1b, resulting in a measurable photoresponse [105]. An MSM photodiode can be used to characterize nanoscale resonant structures in two ways, the MSM electrodes themselves can be structured to support a surface plasmon resonance, as in the case of the interdigitated device in Fig. 3.1d or, a plasmonic resonant structure can be placed between the electrodes, as in Fig. 3.1c.

The optical portion of the characterization was accomplished by retrofitting a spectrometer (Newport Model 77700) such that the device being tested now replaces the commercial

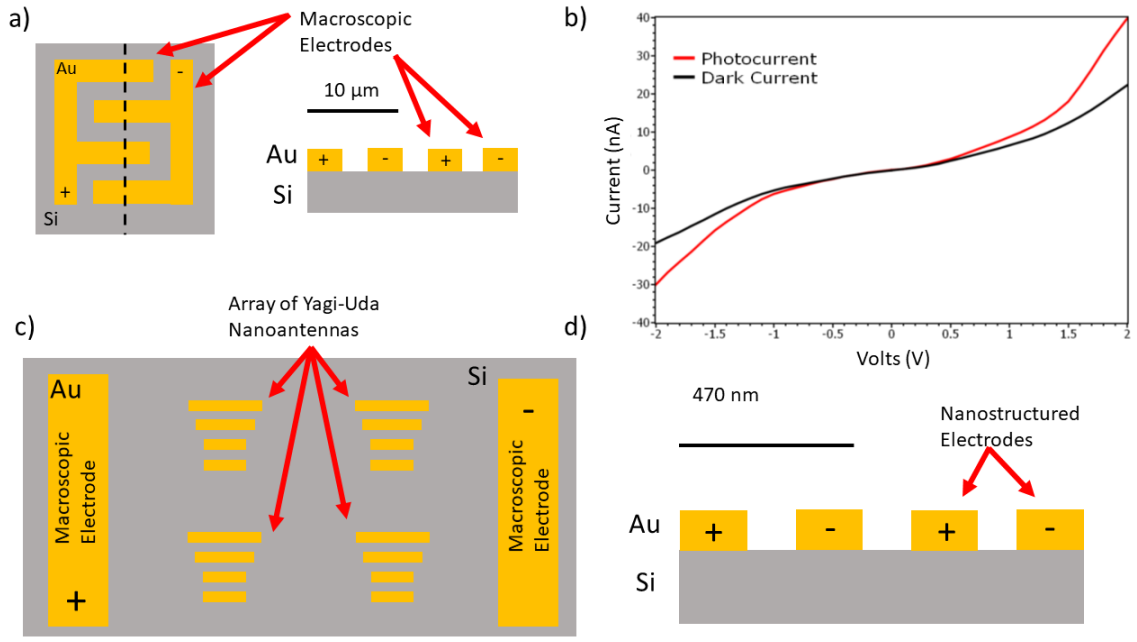

Figure 3.1: Metal-semiconductor-metal (MSM) inspired characterization method for nanoscale optical resonators. a) A standard MSM photodiode, a real view (left), and a cross section taken at the black dotted line (right). Positive and negative bias voltages are denoted on the Au electrodes. b) IV curve of a MSM photodiode fabricated for this dissertation. c) Yagi-Uda nanoantenna device; the nanoantennas are arranged in an array between two macroscopic electrodes which form an MSM. d) Cross section of interdigitated grating device; this is essentially identical to the standard MSM photodiode shown in a), but with a grating period equal to the wavelength of incident light.

photodetector. The optoelectronic characterization setup is depicted in Fig. 3.2. A white light source in a metal enclosure is the source of illumination. The white light exits an aperture in the enclosure (shown as a black line in Fig. 3.2). A chopper driven at 16 Hz is positioned immediately in front of the aperture; chopped light is shown as a dotted line in Fig. 3.2. A series of lenses placed in the optical path after the chopper collimate the white light. This collimated light is incident on an aperture that exists on the spectrometer enclosure. Inside the enclosure, a mirror redirects the white light onto a diffraction grating. The light reflected from the diffraction grating is angularly resolved by wavelength, and exits the spectometer enclosure through a narrow slit as monochromatic light. The wavelength of the light exiting the slit is dependent on the angle of the diffraction grating relative to the incident optical path, α; this angle is controlled by a computer program that drives the spectrometer. The MSM device is placed beyond the exit slit of the spectrometer enclosure, and on a rotatable sample stage that allows the angle of incidence, θ, of the monochromatic light to be varied. The measurement of the interdigitated device (see Section 5.1) utilized an optical fiber placed between the spectrometer exit slit and the device to decrease the spot

size of the light, emphasizing the photoresponse of the nanoresonant structure relative to that of the background.

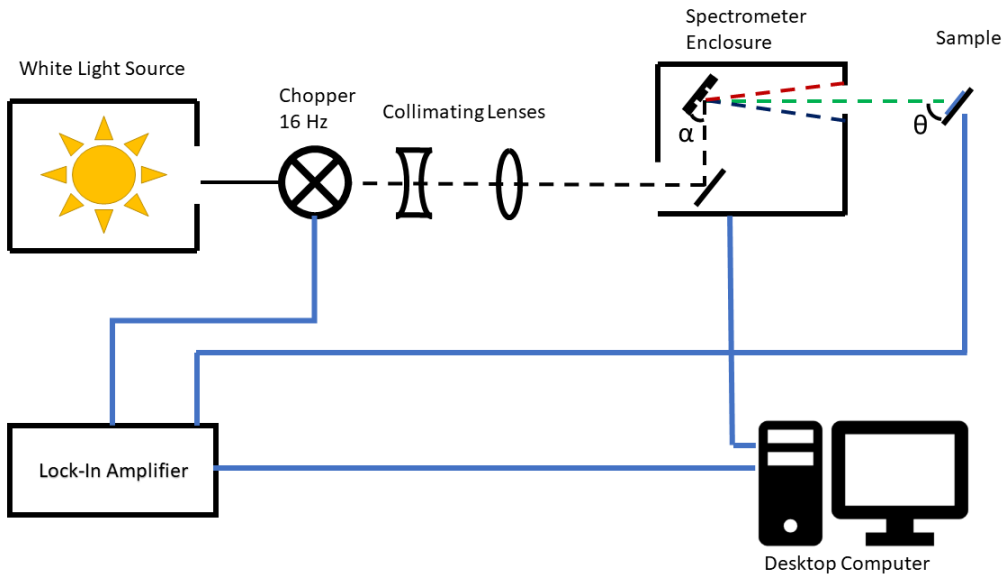

Figure 3.2: Optoelectronic experimental setup. The optical portion of the experimental setup is a modified spectrometer optimized for specific measurements. The electrical portion of the experimental setup utilizes a lock-in detection scheme. The entire experiment including data logging is controlled via custom software modified from the spectrometer control software source code.

The electrical portion of the characterization made use of a computer for data logging and spectrometer control, as well as a lock-in detection scheme. The computer controlled both the wavelength of the monochromatic light and the lock-in amplifier via serial commands. Lock-in detection is a noise reduction scheme whereby a periodic stimulus, in this case chopped monochromatic illumination, is applied and only the portion of the response having the same period and phase is considered. The Yagi-Uda device (see Sections 5.3 and 5.4) was measured by applying a 1 V DC bias and measuring the photocurrent directly with the lock in amplifier. Measurement of the interdigitated structure took place before lock-in detection was implemented; the open circuit photovoltage was instead measured with a voltmeter.

Chapter 4

Simulation

The use of simulation to predict surface plasmon behavior, particularly resonances, reduces the time and material needed for a comprehensive investigation of nanoscale resonant optoelectronic devices. This would be achieved most effectively by a model based on first principles and capable of quantitatively predicting experimentally observable electrical responses—photovoltages, or photocurrents. Such a solution is still under development [71]. A suitable alternative is the use of RF and microwave antenna designs as inspiration for nanoscale resonators. An analytical prediction making this connection has been previously developed for structures consisting of rod-like elements [52, 106]. This prediction maps the wavelength of free space photons to an effective wavelength which is related to plasma oscillations in a rod-like element. For devices with geometries that either differ from traditional antenna designs or are not made of rod-like elements, the wavelength of the surface plasmon wave that couples to light of a given free space wavelength may be calculated on an infinite metal-dielectric interface. This is the characteristic length relevant to designing resonant structures. Both mentioned methods are employed in this dissertation, and provide useful insight to the design of experimental devices as well as to the interpretation of experimental results. A more robust (and computationally expensive) solution is to use finite element methods (FEM) to solve the electrodynamic wave equation directly within a two or three dimensional domain representing the nanoscale resonant device and its immediate environment. This approach was implemented in this dissertation using COMSOL Multiphysics®. Alternatively, literature reports that nanoantennas have been simulated using mode analysis [107].

4.1 Analytical Effective Wavelength Calculations

A surface plasmon polariton (SPP) is a coupled photon and plasmon, (see Chapter 1 for a more detailed description). The wavelength of the surface plasmon, λ_{sp}, that couples to a

photon of free space wavelength, λ_0, is the characteristic length used in designing resonant structures. A concise analytical solution to the surface plasmon polariton modes supported at a metal-dielectric interface is well established [50] and a detailed derivation can be found in Appendix A. A Mathematica® source code implementing this relationship is in Appendix B. The condition required for existence of a SPP is:

$$\lambda_{sp} = \lambda_0 \sqrt{\frac{\varepsilon^{(d)} + \varepsilon^{(m)}(\omega)}{\varepsilon^{(d)}\varepsilon^{(m)}(\omega)}} \tag{4.1}$$

where $\varepsilon^{(d)}$ is the relative permittivity of the dielectric material. In our case $\varepsilon^{(d)} = 3.5$ for Si, and $\varepsilon^{(d)} = 1.5$ for generic glass (actual values for glass depend on glass type but are approximately 1.5). The small imaginary part of $\varepsilon^{(d)}$ is neglected. $\varepsilon^{(m)}(\omega)$ is the relative permittivity of the metal, and is both complex and frequency dependent. The Drude model [108] is used to determine the complex metallic permittivity expressed as:

$$\varepsilon^{(m)}(\omega) = 1 - \frac{\omega_p^2}{\omega(\omega + i\gamma)} \tag{4.2}$$

where ω_p is the plasma frequency, and γ is the intraband damping term. Specific values of the last two parameters for the metals used in our work are found in Table 4.1. In the

Table 4.1: Material parameters used to calculate metal permittivities according to the Drude model [108].

Metal	$\hbar\omega_p$ [eV]	γ [eV]
Au	8.89	0.07088
Al	12.04	0.1287

infrared and visible region of the spectrum, the choice of the metal is of little consequence to the SPP dispersion whereas the choice of dielectric is not. The significant effect of the dielectric material on SPP dispersion is shown in Fig. 4.1a. This dielectric sensitivity is what makes plasmonic resonant detectors useful as chemical and biological detectors [59, 109]. In the present context, dielectric sensitivity requires nanoscale resonant devices be designed according to the environment in which they will be used—including consideration of protective or anti-reflective coatings. Figure 4.1b shows the negligible impact of the metal on SPP dispersion, with a notable exception at shorter wavelengths. At shorter wavelengths the energies of the associated photons are sufficiently high to excite interband transitions—causing the Drude model to fail.

A metallic thin film on a substrate hosts SPP modes at the air-metal and substrate-metal interfaces. These modes are coupled to each other by evanescent electric fields existing in the metal, but may be treated independently for sufficiently thick films. The general expression

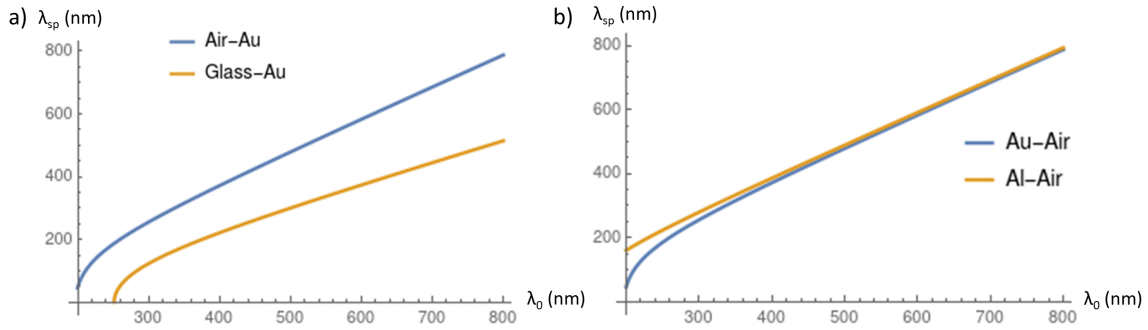

Figure 4.1: a) Surface plasmon wavelength, λ_{sp}, vs. free space wavelength, λ_0, of SPP allowed at an infinite metal-dielectric interface. The dielectric is air; both Au and Al are considered to demonstrate the metal permittivity dependence. Note that for visible and longer wavelengths, the choice of metal is not critical. b) Surface plasmon wavelength, λ_{sp}, vs. free space wavelength, λ_0, of SPP allowed at an infinite metal-dielectric interface. The metal is Au; both air and glass are considered to demonstrate the dielectric permittivity dependence. Note that the λ_{sp} vs. λ_0 relationship is very sensitive to the dielectric permittivity.

for the dispersion relation for these coupled modes as derived in Appendix A is:

$$\left[\frac{\varepsilon^{(m)}(\omega)}{\varepsilon^{(d)}}\frac{\kappa_z^{(d)}}{\kappa_z^{(m)}}+1\right]\left[\frac{\varepsilon^{(m)}(\omega)}{\varepsilon^{(s)}}\frac{\kappa_z^{(s)}}{\kappa_z^{(m)}}+1\right]=\left[\frac{\varepsilon^{(m)}(\omega)}{\varepsilon^{(d)}}\frac{\kappa_z^{(d)}}{\kappa_z^{(m)}}-1\right]\left[\frac{\varepsilon^{(m)}(\omega)}{\varepsilon^{(s)}}\frac{\kappa_z^{(s)}}{\kappa_z^{(m)}}-1\right]e^{-2\kappa_z^{(m)}T} \tag{4.3}$$

where $\varepsilon^{(s)}$ is the relative permittivity of the substrate, and $\kappa_z^{(d)}, \kappa_z^{(s)}, \kappa_z^{(m)}$ are the decay coefficients of the evanescent field into the dielectric (above the film), metallic film, and substrate (below the film) respectively. T is the thickness of the film. The coupling factor between the SPP modes above and below the film can be seen as $e^{-2\kappa_z^{(m)}T}$. For $T \to \infty$ the coupling can be neglected, and SPP modes existing on each interface may be written separately as:

$$\left[\frac{\varepsilon^{(m)}(\omega)}{\varepsilon^{(d)}}\frac{\kappa_z^{(d)}}{\kappa_z^{(m)}}+1\right]=0,\left[\frac{\varepsilon^{(m)}(\omega)}{\varepsilon^{(s)}}\frac{\kappa_z^{(s)}}{\kappa_z^{(m)}}+1\right]=0 \tag{4.4}$$

In Fig. 4.2 we delineate the two decoupled modes. The coupling is frequently destructive in thinner films where strong fields from the SPP modes at each interface overlap. This destructive response is negligible for films with thickness, T, much greater than the decay coefficient, $\kappa_z^{(m)}$. For this reason increased photoresponse has been observed in devices with thicker films [42]. Figure 4.2a & c, show the charge distribution and SPP dispersion respectively of SPP on the surface of bulk Au. Figure 4.2b & d, show the charge distributions and SPP dispersions respectively of decoupled SPP on both interfaces of an Au thin film.

For rod-like nanoantenna structures, an effective wavelength, λ_{eff}, may be defined which maps RF antenna designs to nanoantenna devices [52]. A rod-like nanoantenna consists of one or more elements as pictured in Fig. 4.3. These elements are cylinders of length $L - 2R$

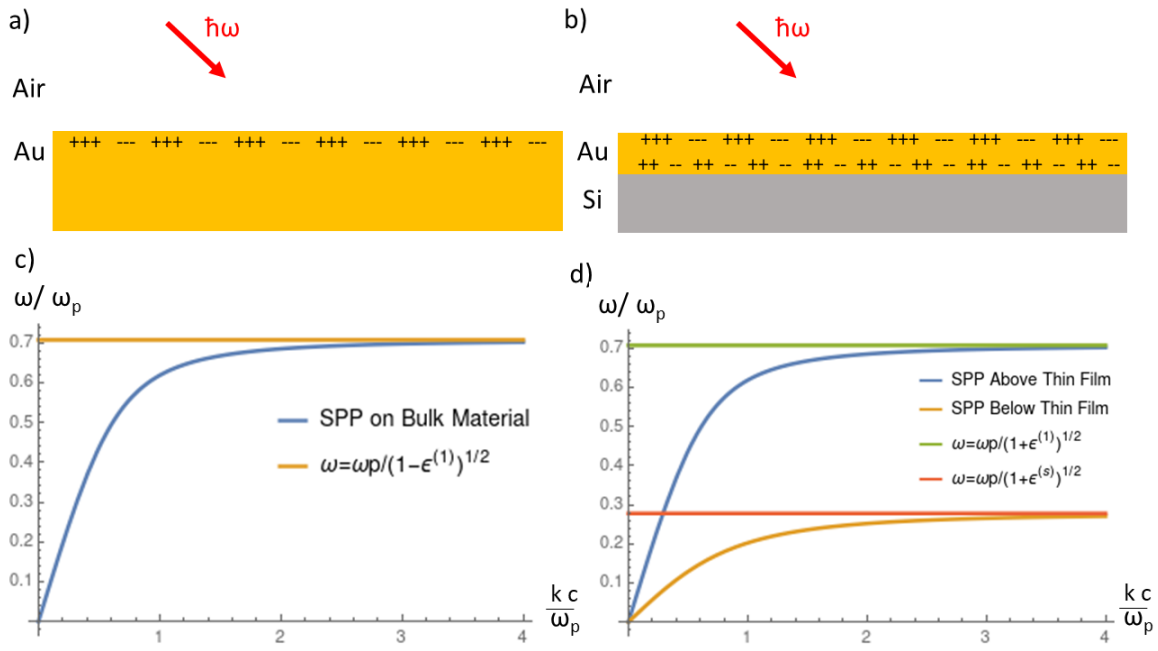

Figure 4.2: a) Infinite metal-air interface on bulk Au. Red arrows indicate the photon half of an SPP, and spatial charge distribution indicates the presence of the surface plasmon half of SPP. b) Same as a), but for a thin Au film on a Si substrate. c) SPP dispersion on bulk Au as pictured in a). d) SPP dispersion for thin Au film as pictured in b). SPP modes above and below the film are assumed to be decoupled.

where R is the radius of the hemispherical rod ends. $R << L$ is required for rod-like behavior. Additionally, the effective wavelength theory requires the antenna structure be encased in a uniform dielectric [52]. The simplest expression connecting the effective wavelength to its free space counterpart is given as [52]:

$$\lambda_{eff} = a + b\frac{\lambda_0}{\lambda_p} \tag{4.5}$$

where a and b are parameters which depend on material and geometry, and λ_p is the plasma wavelength (a material property of the metal). Consistency with macroscopic antenna design is confirmed by noting that for $\frac{\lambda_0}{\lambda_p} >> \frac{a}{b}$, $\lambda_{eff} \propto \lambda_0$ [52]. For the metallic rod-like elements previously described the effective wavelength relation may be analytically expressed as:

$$\lambda_{eff} = \frac{\lambda_0}{\sqrt{\varepsilon^{(d)}}}\sqrt{\frac{4\pi\varepsilon^{(d)}(R^2/\lambda_0^2)\tilde{z}(\lambda_0,\varepsilon^{(m)})^2}{1-4\pi\varepsilon^{(d)}(R^2/\lambda_0^2)\tilde{z}(\lambda_0,\varepsilon^{(m)})^2}} - 4R \tag{4.6}$$

with $\tilde{z}(\lambda_0, \varepsilon_{(m)})$ a function related to both the geometry, and the permittivity of the metal (see ref [52] for a detailed derivation). Note that the second term, $4R$, causes a vertical offset, and is derived from the capacitive contribution of the rod ends. This capacitive contribution

to the effective wavelength may be used as a fitting parameter as described below, and is indicated symbolically as λ_c. The Drude model [108] was again used to calculate $\varepsilon^{(m)}$ (with λ_0 dependence implicit). $\varepsilon^{(m)}$ again has a much smaller impact on the effective wavelength than the $\varepsilon^{(d)}$. A Yagi-Uda antenna is an array of rod-like dipole antennas, and is well char-

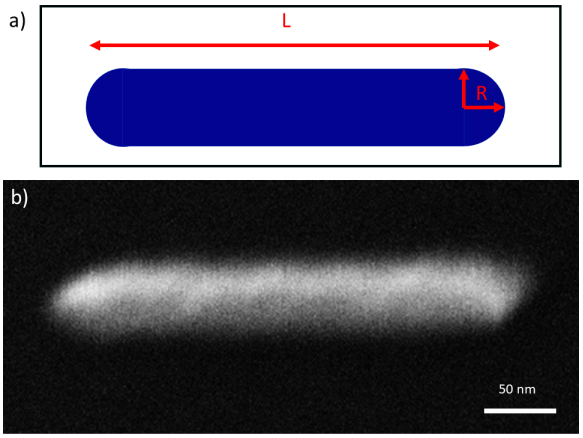

Figure 4.3: Rod-like nanoantenna: a) The theoretical geometry used to calculate effective wavelength analytically. The blue region is the metallic region, and the white background a uniform dielectric. b) SEM micrograph of single element from the experimental Au Yag-Uda nanoantenna device on Si substrate. Note the slight geometrical discrepancies due to equipment resolution. Measured: $L = 406$ nm, and $R = 28$ nm. Design:$L = 388$ nm, and $R = 25$ nm.

acterized in the RF portion of the spectrum. For this reason it is an excellent candidate for effective wavelength theory [52]. However, the optoelectronic devices studied in this dissertation differ from the ideal case in two ways: they exist on a semiconducting substrate, and they differ slightly in geometry (i.e. they are not perfect cylinders and hemispheres) as seen in Fig. 4.3. Their existence on a semiconducting substrate is intrinsic to the optoelectronic characterization technique. This is accounted for by defining an effective relative permittivity, K, which is bounded above and below by the relative permittivity of the semiconducting substrate and air, respectively. The difference in geometry is due to the resolution of the fabrication equipment, and is considered by treating λ_c as a fitting parameter. Reasonable values of λ_c are of magnitude $4R$. The value of both K and λ_c must be determined by fitting the calculated effective wavelength to the experimentally observed resonances. An example of this procedure can be found in Chapter 5. Results.

4.2 Finite Element Method

Finite Element Method may be used to calculate the SPP behavior for any arbitrary shape [110]—not just rod-like elements as above. In this dissertation, COMSOL Multiphysics®

wave optics module was used to implement FEM. Because of the increased computational requirements, FEM calculations took place on the high performance computing clusters provided by Virginia Tech's Advance Research Computing group. While our and other experimental works measure photovoltage or photocurrent, it is not yet possible to compute these quantities directly. However, based on conservation laws, it is possible to relate these to absorbance which can be quantitatively modeled. Absorbance (α) is the integral of the power loss density, Q, within the applicable region divided by the incident light power, P_0, and is expressed as:

$$\alpha = \frac{1}{P_0} \iiint_V Q \, dx \, dy \, dz \tag{4.7}$$

the absorbance is independently calculated in both the metal, α_{metal}, and semiconductor, $\alpha_{substrate}$, regions. Their sum total, α_{total}, is also calculated. The total observed photocurrent, I_{ph}, is a result of both effects, though the correct relative weighting (a_1, a_2) is yet to be determined, and will be a topic of future investigation. This is expressed algebraically as:

$$I_{ph} = a_1 \alpha_{metal} + a_2 \alpha_{substrate}. \tag{4.8}$$

a_1 and a_2 may be determined by fitting to experimentally measured photocurrents, or through a more developed modeling method that accounts for carrier generation and transport of excited carriers in both the metal and the semiconductor this is a goal of the total model presented in Chapter 6.

4.2.1 COMSOL Multiphysics®

A complete COMSOL® model is comprised of four essential elements called nodes: Global Definitions, Component, Study, Results. Each node has multiple subnodes that vary depending on the model requirements.

Global Definitions: Parameters that affect the component geometry, mesh, or require global scope for other reasons are defined here.

Component: This is where most of the physics is defined. Equations, such as equation 4.7 are defined in the definitions subnode. The structure in terms of the parameters listed in the Global Definitions node is defined in the geometry subnode. In the materials subnode a material for each domain is either defined or selected from the built-in materials library. The physics subnode, in this case "electromagnetic wave: frequency domain", defines both the physical equations to be solved, and the way in which they are to be solved i.e. frequency domain, time domain, or eigenvalue. Additionally, initial conditions, boundary conditions, and excitations are defined in the physics subnode. Finally, the mesh subnode defines a finite set of discrete points where the equations will be solved.

Study: The study node defines the solver, the parameteric sweep, and acceptable error.

Results: The results node includes post processing tools for data reduction, and visualization.

The COMSOL® models for nanoscale resonant optoelectronic devices have many commonalities independent of the geometry. All models included three materials—Au, Si, and air. The complex indices of refraction for Au and Si assume experimental values from literature sources [111, 112] and are shown in Fig. 4.4. Note that they are both complex and frequency dependent. The incident light for all models is launched from a domain backed port. The exterior boundaries of the model were either periodic, simulating an infinite device, or perfectly matched layers to prevent reflections that could cause artifacts.

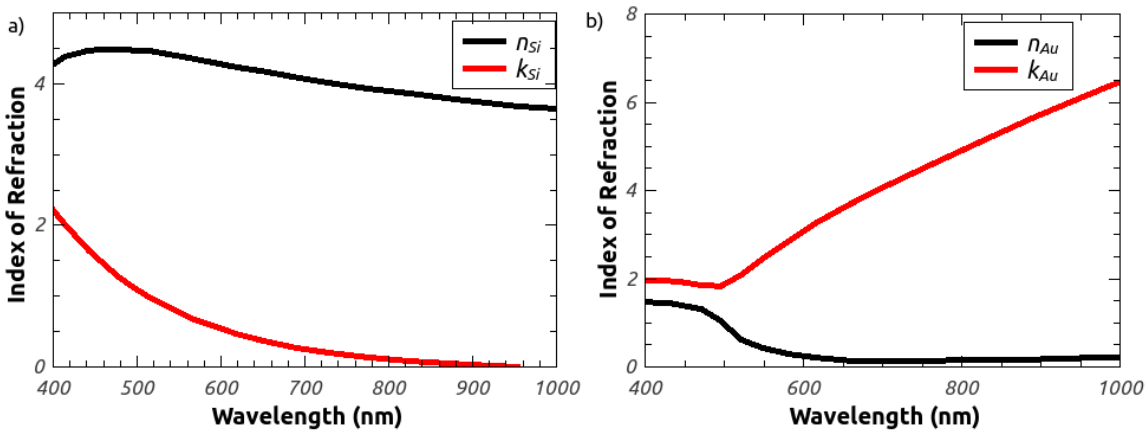

Figure 4.4: Experimental complex indices of refraction. a) Real part, n_{Si}, (black) and imaginary part, k_{Si}, (red) of complex Si index of refraction from literature [112]. b) Real part, n_{Au}, (black) and imaginary part, k_{Au} (red) of complex Au index of refraction from literature [111].

The model has been corroborated using two methods: applying it to a simplified transmittance measurement, and comparing it to literature measured photocurrents. Additionally, the sum $\alpha + \rho + \tau = 1$ for all models, where ρ and τ are the reflectance and absorbance, respectively. The simplified transmittance measurement was accomplished by depositing a Cr/Au layer on a glass slide cover in the same fashion as on the experimental devices. The transmittance was measured using UV-visible spectrometry. Figure 4.5 shows the qualitative agreement between the measured and numerically calculated transmittance of our Cr/Au coated glass slide cover. There are maxima in both transmittances slightly above 500 nm. SPP may exist at both the Au-Air and Au-glass interfaces at this wavelength. The electric fields associated with the SPP are evanescent into the metal. The 50 nm thick Au layer is thin enough to allow the SPP at the two interfaces to couple. Evidence of this coupling may be observed in Fig. 4.5 inset. Note that the occurrence of a single minimum in electric field intensity is consistent with opposing evanescent fields. The sharp spike occurring exactly at 25 nm is in the exact center of the metallic region and is understood to be an artifact of

the model. The quantitative difference between the measured and modeled transmission is likely due to the difference in thickness of the glass substrate and modeled glass region, 160 μm and approximately 0.5 μm, respectively.

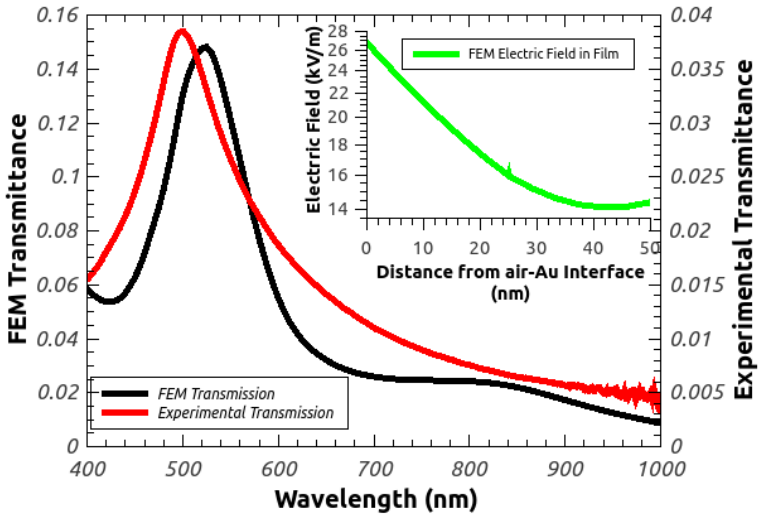

Figure 4.5: Experimental (red) and FEM modeled (black) transmittance through a 50 nm Au layer on a glass substrate. The qualitative agreement corroborates the model validity. The inset shows electric field intensity in the metal film. Evanescent fields decaying exponentially from both the air-Au interface (0 nm) and the Si-Au interface (50 nm) suggest SPP at both interfaces, coupled via the evanescent fields.

Experimentally observed photocurrents [42] were compared to our modeled α_{metal}. (note: since the permittivity of Si is real for wavelengths longer than approximately 1000 nm, $\alpha_{metal} = \alpha_{total}$ in this region of the spectrum). The technical details of the model used to calculate these absorbances differ from the interdigitated model discussed in Subsection 4.2.2 only in the geometry, which was chosen to match the experimental device. The experimental device used in the literature [42] consisted of an Au grating (L given in Fig. 4.6 legend, $W = L + 250\ nm$, and $T = 250\ nm$, L, T, and W defined in Subsection 4.2.2) formed directly on a Si substrate; an ohmic contact was made elsewhere on the Si. This differs from the experimental method used in the interdigitated device discussed in this dissertation because the literature device [42] forms only a single Schottky diode, and operates at a wavelength where $\alpha_{substrate}$ can be neglected. However, both devices rely on hot carrier injection to generate a photoresponse. Figure 4.6a shows the experimental photocurrents from the literature [42] with dashed lines, and the modeled FEM absorbances with solid lines for seven different grating aspect ratios. The agreement between experimental photocurrent maxima and FEM absorbance maxima is shown in Fig. 4.6b. The demonstrated agreement between the literature device [42], and our FEM modeled absorbances confirms our modeled absorbance gives a good first approximation to the optoelectronic response.

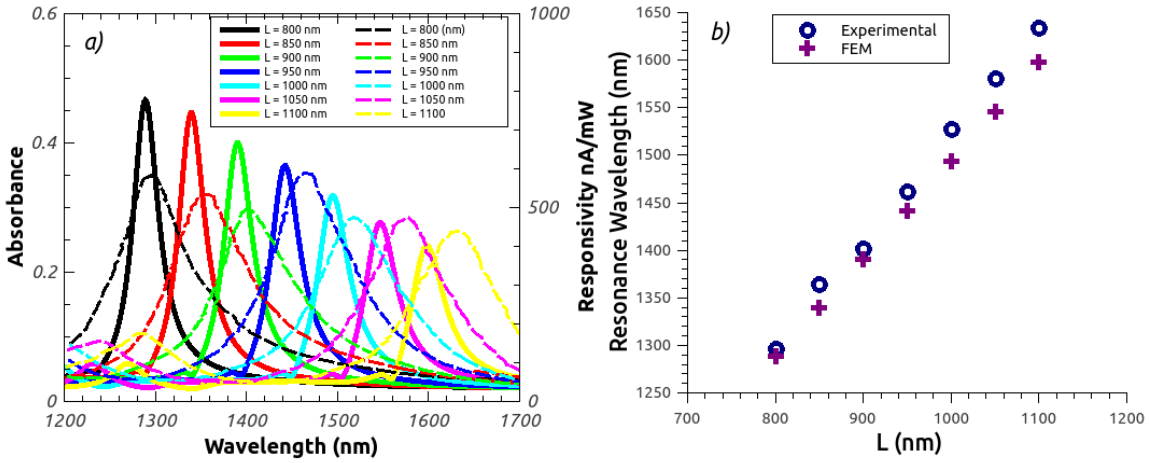

Figure 4.6: Experimental responsivity and our FEM modeled absorbance for a grating nanoscale resonant optoelectronic device: a) Experimental (dashed) responsivity [42] and FEM modeled (solid) absorbance show strong qualitative agreement. b) Resonant wavelengths for experimental responsivity (circles), and FEM absorbances (crosses).

4.2.2 Interdigitated Structure

The spectral response of an interdigitated device (see Chapter 3) was modeled by computing the total absorbance, α_{total}, in the metallic and semiconducting regions of a one-dimensional infinite grating. We will treat the interdigiatated device effectively as a grating. We consider one-dimensional infinite grating formed by defining a two-dimensional unit cell, and imposing periodic boundary conditions on the left and right boundaries. Perfectly matched layers are defined above and below the unit cell to prevent reflections at these boundaries; reflections at the model boundary can cause artifacts. Figure 4.7 shows the two-dimensional unit cell comprised of three regions: an upper air region (light grey), a central metallic region (yellow), and a lower semiconductor region (dark grey). The geometry of each region is defined in terms of parameters W, L, and T as indicated in Fig. 4.7 (W: the grating periodicity; L: the width of the metallic region; T: the thickness of the metallic region). A port is defined at the upper boundary which is used to excite the incident monochromatic polarized plane wave, which is incident normal to the grating plane. The incident light is polarized with the electric field along the direction of periodicity. Lines are defined near the top and bottom of the unit cell. The Poynting vector is integrated along these lines, and the transmittance, τ, is:

$$\tau = -\frac{1}{P_0}\int_{bottom\ line} |\vec{P}_{avg}(x)|dx \tag{4.9}$$

and the reflectance, ρ, is:

$$\rho = \frac{1}{P_0}\int_{top\ line} |\vec{P}_{avg}(x)|dx - P_0 \tag{4.10}$$

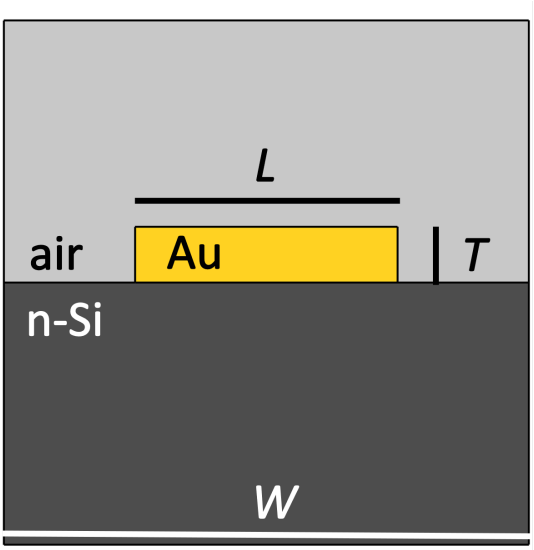

Figure 4.7: Geometry of interdigited device used in two-dimensional finite element modeling. The upper and lower boundaries are ports with monochromatic light originating at the upper port and incident on the sample perpendicular to the structured surface. Periodic boundary conditions exist at the left and right boundaries.

note the minus sign exists because the coordinate system is defined such that the incident light wave travels along the negative y axis. Conservation of energy requires [113]:

$$\alpha_{total} + \tau + \rho = 1 \tag{4.11}$$

An example case is demonstrated in Figures 4.8 and 4.9, with device parameters indicated.

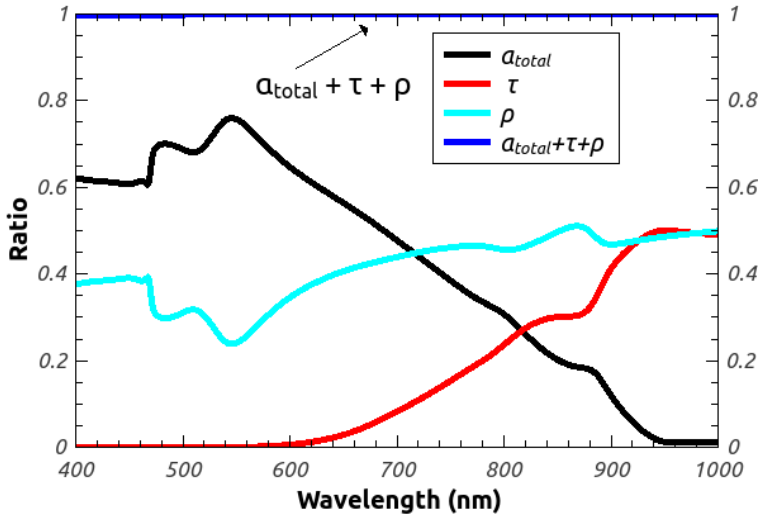

Figure 4.8: FEM modeled absorbance, α_{total}, transmittance, τ, and reflectance, ρ, for an example case of the interdigitated device with $W = 470$ nm, $L = 187$ nm, and $T = 50$ nm. Conservation of energy requires $\alpha_{total} + \tau + \rho = 1$ as shown at the top of the plot.

In Fig. 4.9 a triangular mesh was defined for the entire model domain and a swept mesh was defined for the perfectly matched layers. The mesh size was chosen so that there are at a minimum six mesh points per wavelength, and the mesh was more dense in and around the metal region where field gradients are highest. The FEM modeled total absorbance, transmittance, and reflectance are plotted in 4.8.

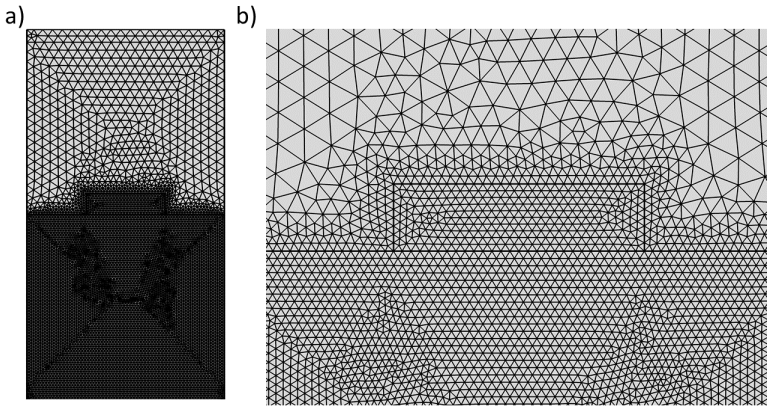

Figure 4.9: An example mesh used for model with parameters $W = 470$ nm, $L = 187$ nm, $T = 50$ nm. The mesh density was held constant resulting in the number of mesh points (and hence degrees of freedom) being variable.

4.2.3 Yagi-Uda Nanoantenna

The spectral response of a Yagi-Uda antenna was also modeled using FEM. Many of the methods described previously in the interdigitated model also apply to the Yagi-Uda model. There exist two complications when using FEM to model the absorbance of our Yagi-Uda nanoantennas devices. The first complication is the necessity of using a three-dimensional model domain. The second is the inability to treat the model as a unit cell in an infinite periodic structure. Both of these issues are addressed by decomposing the model into two steps. First, a model domain is defined lacking the metallic nanoantenna. The boundary at the top and bottom of the model domain are ports that allow the excitation of an electromagnetic plane wave. The four horizontal boundaries are subjected to periodic boundary conditions, simulating a semi-infinite Si slab. The electric and magnetic fields calculated in this way are background fields, and form the input to the second step of the model. The second step replaces the metal nanoantenna, takes the previously calculated fields as initial conditions, and defines all six boundaries with perfectly matched layers. The electric and magnetic fields calculated in this second step are the scattered fields. The absorbance, α_{metal}, is calculated based on the scattered fields. Note that $\alpha_{metal} = \alpha_{total}$ for the same reasons as discussed in Subsection 4.2.1. Figure 4.10 shows the three-dimensional model geometry. Four metal bars (yellow) make up the Yagi-Uda antenna. The air-Si interface is shown in grey. The region below the grey plane is Si, above is air. Not shown are the perfectly matched layers surrounding the entire physical domain. Since the incident light originates

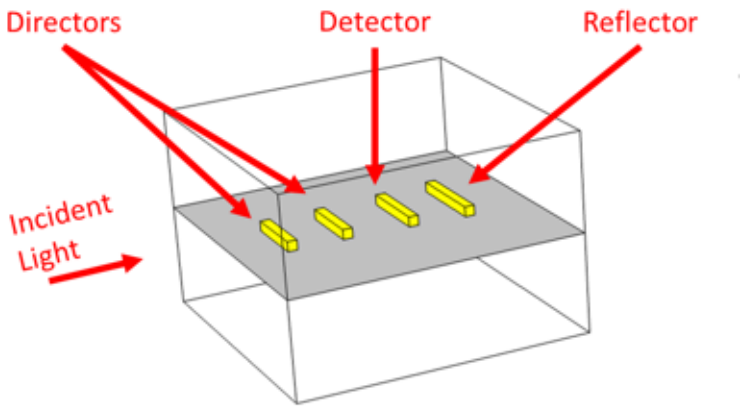

Figure 4.10: Three-dimensional modeling domain for Yagi-Uda nanoantennas. Four metal regions (yellow) make up the nanoantenna. The Si (below) and air (above) interface is indicated with a grey plane. Incident light travels at a glancing angle as pictured.

at the port on the upper boundary, it is not possible to model perfectly horizontal incident light. However, arbitrarily shallow angles of incidence may be modeled. Figure 4.11 shows

the model absorbance at a glancing angle with insets depicting the power loss density, Q, profiles at the two resonance modes. Comparison of these resonances with experimentally observed photocurrents is discussed in the Chapter 5.

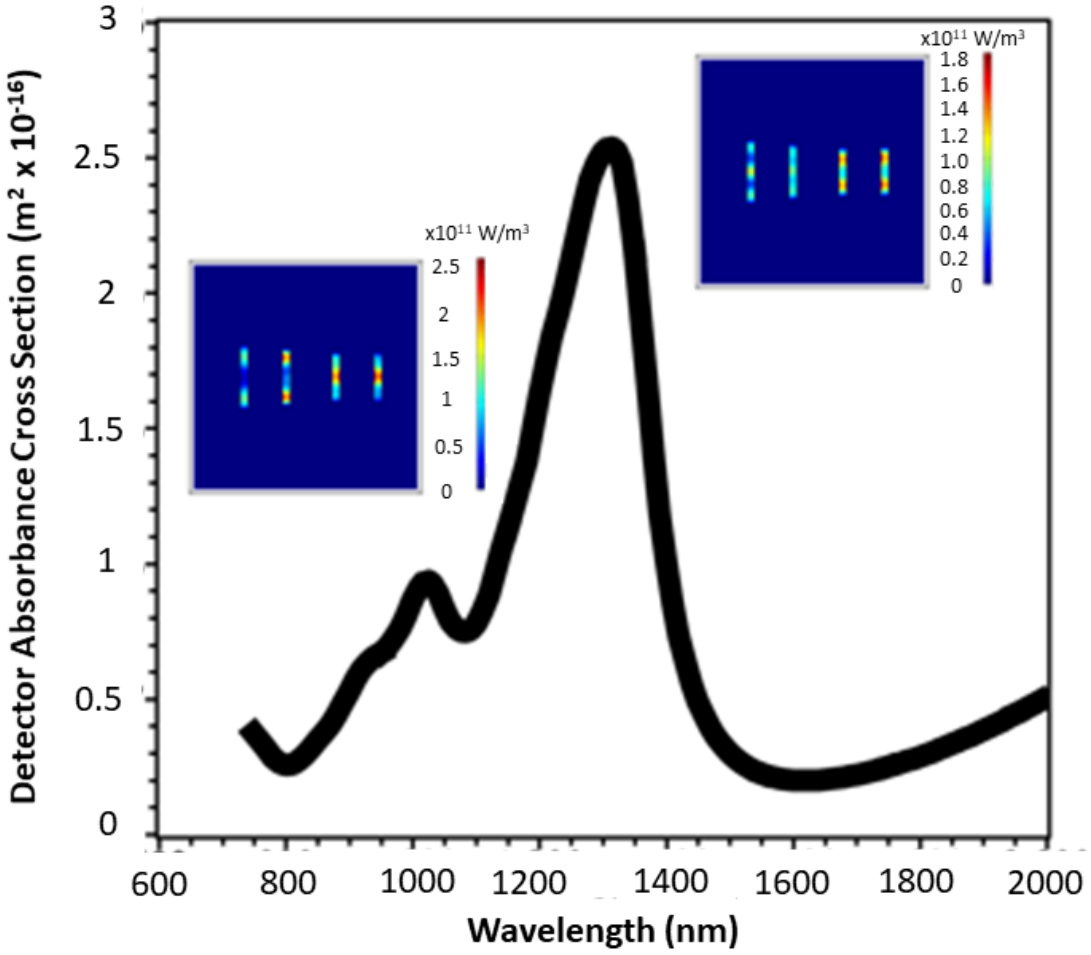

Figure 4.11: FEM modeled absorbance in a Yagi-Uda nanoantenna with incident light at a glancing angle. Insets depict power loss profile at two observed resonances.

Chapter 5

Results and Analyses

5.1 Electronic Detection of Photonic Band Gaps in Nanolithographic Metal Gratings

This section has been submitted to the editors of *Journal of Quantum Electronics* and is under review as: "Electronic Detection of Photonic Band Gaps in Nanolithographic Metal Gratings"

William Rieger was the primary author; as such he was primarily responsible for drafting the manuscript, fabricating devices, characterizing devices, and performing modeling.

Electronic Detection of Photonic Band Gaps in Nanolithographic Metallic Gratings

William Rieger, Yuhong Kang, Jean J. Heremans and Hang Ruan

***Abstract*—In nanolithographic metallic gratings we investigate the dependence of photonic band gaps on geometrical parameters. Finite element modeling was used to develop a model for an optoelectronic device with periodicity of 470 nm and concomitantly the electronic response of a nanofabricated metal-semiconductor-metal photodetector grating was experimentally studied under a sweeping monochromatic light source. The grating spectral response increased in the region between 470 nm and 520 nm, corroborating the computational results. This increase is understood to occur because photons with wavelength shorter than approximately 520 nm are energetic enough to excite interband transitions in the Au, but the period of the structure acts as a cutoff where incident photons with wavelength shorter than the period are less likely to form surface plasmon polaritons. This cutoff originates from a photonic band gap. Magnetic field intensity profiles at the 3 dB cutoff indicate that a surface plasmon wave exists where each finger interacts with the next through overlapping magnetic fields, suggesting that the cutoff is a surface plasmon wave effect. Localized surface plasmon effects were observed at longer wavelengths in the modeled absorbance. The effects of three geometrical parameters on the spectral dependence of modeled absorbance were investigated.**

***Index Terms*—plasmon, optoelectronic devices, metallic grating, photonic band gap.**

I. Introduction

SUBWAVELENGTH structures are of interest due to their ability to engineer material properties beyond the limits of naturally occurring compounds. Current nanofabrication techniques allow the development of geometry-enhanced devices operating in the visible and infrared region of the spectrum. Specifically, hyperbolic metamaterials[1], [2], [3], negative indices of refraction[4], [5], second harmonic generation[6], [7], and photonic crystals[8], [9], [10], [11], [12] have all been of interest. The metallic grating studied here functions as a 1-dimensional (1D) photonic crystal. Metallic gratings with sub-wavelength slits have been studied previously using optical techniques.[13], [14], [15] The present work presents an electrical characterization based on our previously reported technique.[16] By comparing the electrical measurement with modeled plasmonic excitations we highlight the mechanisms that contribute to the electronic signal. We report an electrical detection of photonic band gaps and computational analysis of a metallic grating fabricated on a semiconductor surface where Schottky barriers are formed at the structure-semiconductor interface. Such a structure is a metal-semiconductor-metal (MSM) electronically rectifying detector device that exhibits an open circuit voltage, V_{oc}, when the metallic grating is photoexcited. Spectral response of traditional MSM detectors is determined by the material properties of the semiconducting substrate. In metallic gratings on the other hand, if the surface structure interacts with incident light wavelength comparable to its periodicity, then the spectral response is a function of this periodicity, yielding a modifiable spectral response characteristic of a 1D photonic crystal. Previous work indicates that the dispersion relation of a surface plasmon polariton (SPP) exhibits a band gap.[8], [9], [10], [11], [12], [17], [18], [19], [20] The wavelengths marking the edge of the band gap are expressed as [9]:

$$\left(\frac{2\pi}{\lambda_{\mp}}\right)^2 = \left(\frac{2\pi}{\lambda_0}\right)^2 [1-(Kd)^2] \pm 2(Kd)\frac{K^2}{\sqrt{-\epsilon_m\epsilon_d}}[1-(Kd)^3] \quad (1)$$

where $2K$ represents the Bragg wave vector, d the amplitude of the surface corrugation (equivalent to $T/2$ as defined below), λ_0 the wavelength of the free space photon, $\lambda_{\mp}$ the upper and lower band edges as wavelengths, ϵ_m, and ϵ_d relative permittivity of the metal and dielectric respectively. This analytical expression suggests the existence of a band gap, but cannot be readily solved for our device due to a discontinuity in the Au permittivity at approximately 500 nm.[21] We hence use computational techniques to ascertain the location of the band gap. Further, electrical measurements provide experimental evidence of the band gap through the following process. Monochromatic light couples to surface plasmon modes forming SPPs on the metal structure. Surface plasmon waves (SPW) on a uniform thin metal film may exist freely, and it is the relative permittivities of the two materials that determine the conditions necessary for an SPP. Alternatively, localized surface plasmons (LSP) can exist on nanostructures such as nanospheres, nanorods, and nanoantennas; these may also couple with incident photons forming an SPP. Both SPW and LSP exist in the present grating. Overall periodicity has a larger impact on SPW; structural details at the cross sections have a larger role in LSP. The effect of the grating dimensional parameters on both SPW and LSP are considered. We relate measured V_{oc} to modeled absorbance; this is justified

William T. Rieger Jr. was with the Department of Physics, Virginia Tech, Blacksburg, VA 24061, and NanoSonic Inc., Pembroke, VA 24136.

Yuhong Kang was with NanoSonic Inc., Pembroke, VA 24136.

Jean J. Heremans was with the Department of Physics, Virginia Tech, Blacksburg, VA 24061.

Hang Ruan was with NanoSonic Inc., Pembroke, VA 24136, and the Department of Mechanical Engineering, Virginia Tech, Blacksburg, VA 24061. Email:hruan@nanosonic.com

This work is based on support by the U.S. Navy under Contract No. N68335-13-C-0184.

Manuscript received September 10, 2019; revised September ?, 2019.

by comparison to literature experimental data, discussed in modeling section. The injected electrons contribute to a current within the semiconductor, facilitating charge imbalance at the alternating metal-semiconductor interfaces. The charge imbalance results in a measured V_{oc}, and hence a 3 dB cutoff in V_{oc} indicates the presence of a photonic band gap at the wavelength of the incident monochromatic light. We present a study of photonic band gaps in the SPP dispersion relation and their dependence on variations in the device geometry.

II. Nanolithographic Metallic Grating

Figure 1 outlines the nanolithographic metallic grating device and the characterization technique. Figure 1(a) represents a top view of the Au grating on n-Si substrate. The 1D periodicity W, leading to photonic band gaps, lies along the vertical direction of Fig. 1(e). Figure 1(b-c) show the optical and electrical aspects of the experiment, while Fig. 1(d) shows a simplified picture of the resonance at the upper-band-edge (λ_+) with electric field lines shown in red. Parameters W, L, and T define the device period, metal crossection length and metal thickness respectively, and are discussed in more detail below. Parameter values W = 470 nm, L = 187 nm, and T = 50 nm were used in the initial model and experimental device. The present grating design is similar to previous approaches for THz detectors, yet can omit the voltage biasing.[22]

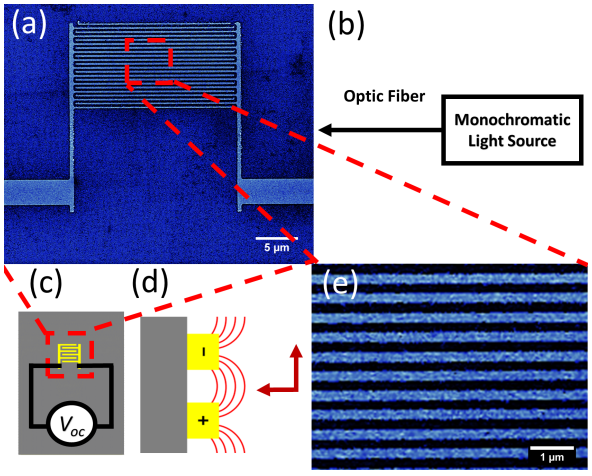

Fig. 1. Nanolithographic metallic grating device and characterization technique. a) Nanolithographic metallic grating and macroscopic electrodes. b) Experimental measurement setup. c) Electrical characterization schematic. The open circuit voltage (V_{oc}) is measured between any two adjacent interdigitated fingers. d) Illustration of one selected resonance leading to an increased open circuit voltage e) Scanning electron micrograph of the nanolithographic metallic grating.

III. Modeling

The spectral response of the MSM structure was calculated by finite element modeling (FEM) using COMSOL Multiphysics. Plasmonic gratings can be effectively modeled using FEM to solve Maxwell's equations.[23] A two-dimensional (2D) modeling domain was defined according to parameters W, L, and T as defined in the introduction and depicted in Fig. 2(a). The modeling domain is comprised of three regions: an upper air region (light gray), a central metallic Au region (yellow) representing a cross-section of one electrode, and a lower semiconducting Si region (dark gray). Au and Si regions use literature material properties while the upper air region uses free space permittivity and permeability values.[24], [21] A periodic boundary condition is imposed on left and right boundaries simulating an infinite 1D structure; top and bottom boundaries are perfectly matched layers to prevent reflection at the boundary; monochromatic light is incident from above, normal to the patterned surface. Incident light is *p*-polarized. Transmitted power measured at the bottom of the modeling domain is approximately zero confirming that the modeled Si region is sufficiently thick. The sum of the modeled transmittance, absorbance, and reflectance was confirmed to be unity for all modeled results. Figure 2(b) depicts the magnetic field intensity profile at an incident wavelength of 470 nm, with false color representing the magnetic field. Note the spatially oscillating wave in intensity that has the same periodicity as the grating. Absorbance (α) denotes the integral of the power

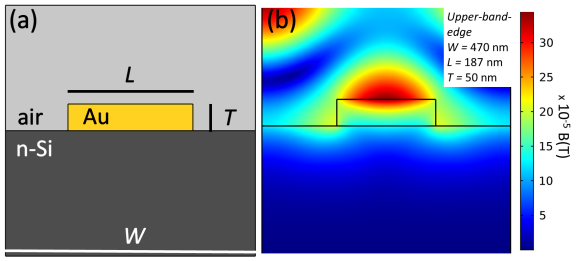

Fig. 2. 2D finite element modeling using COMSOL software. (a) Geometry for the 2D finite element modeling. Ports exist at the upper and lower boundaries with monochromatic *p*-polarized light originating at the upper boundary and normally incident on the grating. Periodic boundary conditions are used at the left and right boundaries. (b) Total magnetic field intensity profile at upper-band-edge. False color is magnetic field intensity.

loss density (Q) within the applicable region divided by the incident light power (P_0) and is expressed as:

$$\alpha = \frac{1}{P_0} \iiint_V Q \, dx \, dy \, dz \tag{2}$$

Figure 3 shows α for a thin film and grating structure and experimental V_{oc} for a device using parameters W = 470 nm, L = 187 nm and T = 50 nm (Dashed black line: absorbance in a uniform metal film; solid black line: absorbance in the metal grating; solid red line: absorbance in Si beneath the grating; solid pink line: the sum total absorbance in the metal grating and Si). FEM absorbance in a uniform thin film is calculated by choosing geometrical parameters W = 470 nm, L = 470 nm and T = 50 nm. From the inset magnetic field intensity profiles, we see that a long range SPW is indicated at 470 nm, whereas LSP are indicated on the Au-Si interface at both 804 nm and 878 nm. Incident radiation is swept over the visible spectrum from wavelengths 400 nm to 1000 nm. Results of the model suggest maxima in the total absorbance, in agreement with a maximum in V_{oc} at approximately 500 nm, as illustrated in Fig. 3. High α is an indication of hot carrier

generation.We understand the measured V_{oc} to be primarily caused by both the generation of hot carriers in the metal grating, and electron-hole pair creation in the Si. Note that the total absorbance displays α contributions from both Au and Si regions. However, a more detailed investigation than aimed in the present work, is required to determine the correct relative weighting of the two effects. The correct weighting may be determined *a priori* through a method of nonequilibrium scattering in space and energy [25] and will be the focus of continuing work. The validity of the FEM is further confirmed

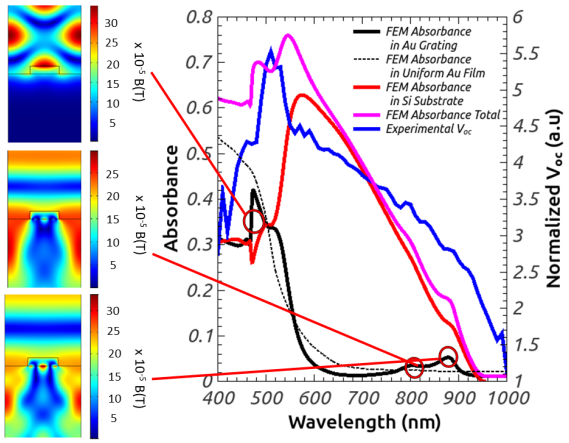

Fig. 3. Comparison of FEM absorbances (left axis) and experimental V_{oc} (right axis). The incremental incident wavelength step in experimental results is 10 nm. FEM absorbances are calculated in a grating structure with geometrical parameters W = 470 nm, L = 187 nm and T = 50 nm (Dashed black line: absorbance in a uniform metal film; solid black line: absorbance in the metal grating; solid red line: absorbance in Si beneath the grating; solid pink line: the sum total absorbance in the metal grating and Si). FEM absorbance for a uniform thin film is calculated by choosing geometrical parameters W = 470 nm, L = 470 nm and T = 50 nm. Note the sharp increase in absorbance of the uniform film below a wavelength of 520 nm due to the interband transition in Au. However, the introduction of the periodic grating cuts off this increase in absorbance. Additionally, two LSP modes are observed in the FEM absorbance at wavelengths 804 nm and 878 nm. Insets show the magnetic field profiles at 470 nm, 804 nm, and 878 nm as indicated.

by comparison with experimental photoresponse from the literature in Fig. 4.[11] Modeled absorbance is shown for L= 800 nm, 850 nm, 900 nm, 950 nm, 1000 nm, 1050 nm, 1100 nm, and W = L + 250 nm and T = 200 nm. The agreement between our FEM modeled absorbance (crosses) and the measured photoresponse (circles) of Ref. [11] is depicted in Fig. 4 inset. These resonance modes are understood to originate from LSPs in the individual grating finger cross sections. The validity of the model is additionally corroborated by comparison to optical transmittance experiments. A 50 nm thick Au film was deposited on a glass microscope slide cover using an identical method to the grating device. The transmittance of the Au-coated glass slide cover was measured using UV-visible spectrometry. Transmittance was modeled for a uniform 50 nm Au film on a glass substrate using the same modeling procedures outlined above. Strong qualitative agreement between our FEM transmittance and our measured transmittance can be seen in Fig. 5. The quantitative difference can be is likely due to the difference in thickness of the glass

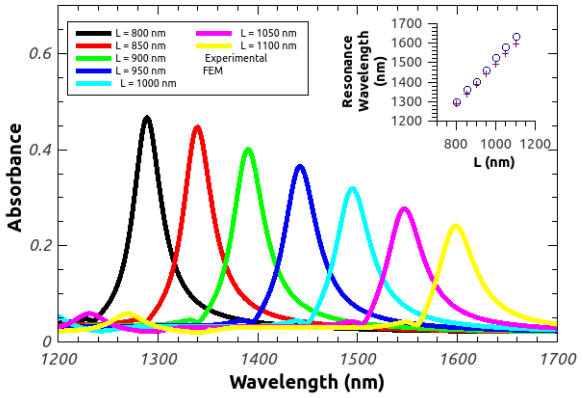

Fig. 4. Comparison of our FEM modeled metallic absorbance to literature measured experimental photoresponse. [11]Modeled absorbances are shown for 7 values of L as listed, with W = L + 250 nm and T = 200 nm. Inset shows the agreement with experimental photoresponse of devices with identical geometrical parameters.

in the experimental device (≈160 μm) and model (≈0.5 μm). The maximum in transmittance at ≈500 nm would be due to coupling of SPWs at respectively the air-Au interface and the glass-Au interface (analogous to electron tunneling through an oxide interface). Evidence of this plasmon coupling can be observed in Fig.5 inset.

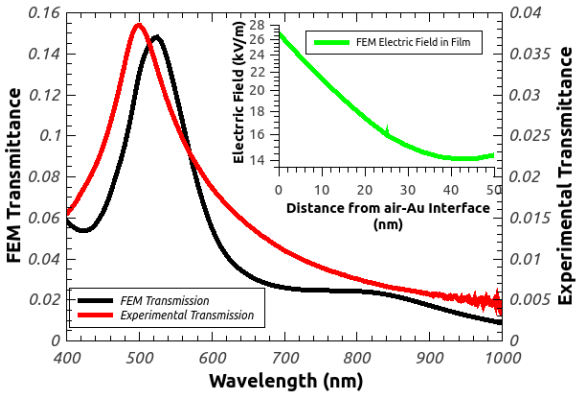

Fig. 5. FEM modeled transmittance, and experimentally measured transmittance of 50 nm Au on glass. The quantitative difference between the modeled and experimental transmittance can be attributed to the FEM model domain not including the total thickness of the glass. Inset shows the evanescent electric field from the air-metal interface. The "turn-around" positive slope between 45 nm and 50 nm (near the metal-glass interface) is characteristic of the presence of a surface plasmon wave at the metal-glass interface. The small spike in electric field occuring at 25 nm in the exact center of the grating cross section is believed to be an artifact.

IV. Results

Experimental and FEM data indicate a maximum in V_{oc} centered at an incident wavelength approximately 500 nm. Generation of V_{oc} is a multi-step process. Plasmons may in general decay along a number of pathways. They may reradiate a photon, they may generate a hot electron, or they

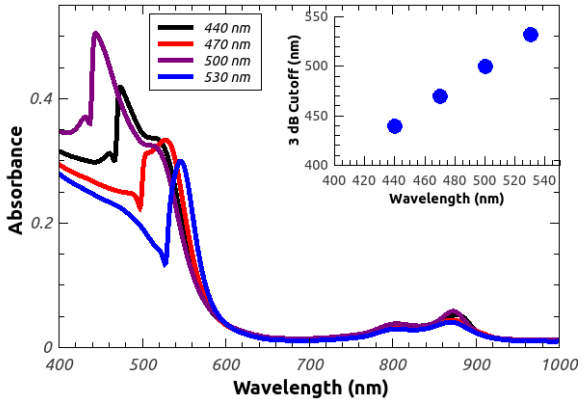

Fig. 6. Dependence of the upper-band-edge (λ_+) on geometrical parameter W. The FEM modeled metallic absorbances for W = 440 nm, 470 nm, 500 nm, 530 nm, and ,L = 187 nm and T = 50 nm are shown. The inset shows the linear dependence of upper-band-edge vs periodicity. Note that the wavelengths of LSP resonances are unaffected by parameter W.

may transfer energy to a crystal lattice. Geometrical and material properties affect the likelihood of plasmons decaying along any given pathway.[25] Because FEM results are obtained in steady-state, reradiated photons present themselves as electromagnetic field oscillations, and do not contribute to the modeled absorbance. The FEM absorbance can then be understood to be entirely due to hot carrier generation and phonon mode excitation. These can be due to intraband excitations or interband transitions. Interband transitions can excite hot holes in addition to hot electrons. The electronic response is dependent not only on the hot carrier generation, but also on the likelihood that hot carriers will reach the Au-Si interface. This is dependant on not only the distance from the interface where the hot carrier is generated, but also the likelihood of electron-electron and electron-phonon scattering. Hot electron injection as a primary contributor to V_{oc} is in agreement with the literature.[26], [27] Electron-hole creation in the Si substrate is also a non negligible contributor to V_{oc}. However, this is well understood and hence we emphasize the metallic contribution. The metallic gratings discussed are understood to have two types of plasmonic effects: SPW effects where wavelengths shorter than the upper-band-edge (λ_+) are suppressed, and LSP effects where a dipole moment is excited along the length of the finger cross section. Three design parameters W, L and T affect the behavior of SPW and LSP uniquely. Figure 6 shows the upper-band-edge(λ_+) dependence on W. The inset shows the linear relationship between upper-band-edge (λ_+) and the period. The two LSP resonance modes occur at the same wavelength independent of W. This supports the understanding that the cutoff is due to the long range aspect of the SPW while the resonances at 804 nm and 878 nm are due to LSP resonances, and are thus primarily affected by L and T. Figure 7 shows the L dependence of the absorbance, which further supports this picture. Two identified LSP resonance modes shift towards longer wavelengths with longer L, showing a linear trend. Figure 8 shows that the overall spectral response is independent of T. However, the magnitude is affected by T, due to both the increase in the total volume of the absorbing material, as well as the decoupling of surface plasmons at the Au-Si interface and the Au-air interface. The Au width L has the most significant

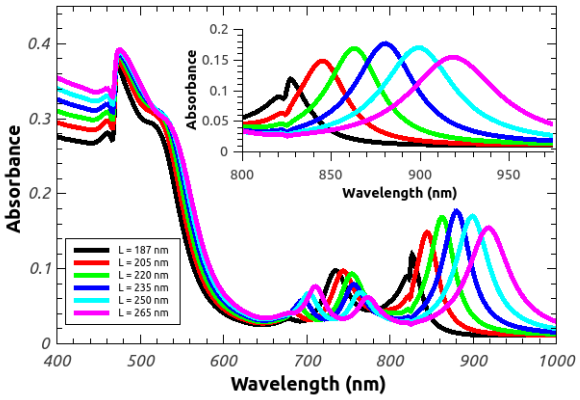

Fig. 7. Dependence of the upper-band-edge (λ_+) on geometrical parameter L. The FEM modeled metallic absorbance for L = 187 nm, 205 nm, 220 nm, 235 nm, 250 nm, 265 nm, and W = 470 nm and T = 50 nm are shown. The inset shows the a magnified view of the LSP resonance mode with the longest wavelength. Note that the upper-band-edge (λ_+) is unaffected by parameter L.

effect on LSP. As T increases, the peak wavelength for the short-wavelength LSP moves slightly, while the absorbance increases.

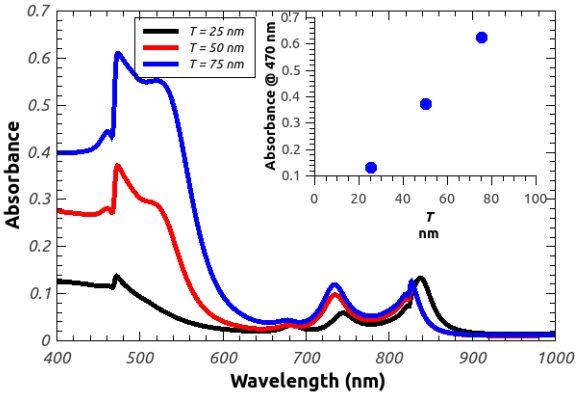

Fig. 8. Dependence of the upper-band-edge (λ_+) on geometrical parameter L. The FEM modeled metallic absorbance for T = {25 nm, 50 nm, 75 nm},L = 187 nm and W = 470 nm are shown. The inset shows a zoomed in view of the LSP resonances.

V. Conclusions

A study is presented to determine the spectral behavior of a nanofabricated metal-semiconductor-metal metallic grating, based on geometrical parameters. Finite element modeling was used to determine the expected spectral response of the nanostructured surface. Strong agreement exists between the calculated absorbance of the metallic structure and the measured photoresponse, corroborating the model. Electrical

measurements may be used as a probe of photonic band gaps, providing a necessary step forward in the integration of optics with electronics. The electronic technique is not limited to detecting photonic band gaps but can be employed in the study of any plasmonic resonant structured surfaces. We observe the upper-band-edge (λ_+) resulting from what is understood to be a photonic band gap occuring at a wavelength approximately equal to the period. Lower intensity, but more geometrically controllable LSP occur at longer wavelengths. Two LSP modes are observed, with locations strongly dependent on L and the height of the shorter wavelength mode strongly dependent on T. The L dependence is understood to be due to the dipole moment of the finger cross section, and the T dependence originates from a decoupling effect between plasmons on the Si-Au and air-Au interfaces. The possibility thus lies open to engineer future device designs to exhibit wavelength selectivity by tuning geometrical parameters. Far-field effects and more rigorous computations of hot carrier injection using a method of nonequilibrium scattering in space and energy. [25] for the study of nanolithographic structured surfaces will form the focus of future work.

ACKNOWLEDGMENT

The authors wish to acknowledge T. Asryan for contributions to COMSOL models.

REFERENCES

[1] A. Poddubny, I. Iorsh, P. Belov, and Y. Kivshar, "Hyperbolic metamaterials," *Nature Photonics*, vol. 7, p. 948, 2013.

[2] P. Li, I. Dolado, F. J. Alfaro-Mozaz, F. Casanova, L. E. Hueso, S. Liu, J. H. Edgar, A. Y. Nikitin, S. Vlez, and R. Hillenbrand, "Infrared hyperbolic metasurface based on nanostructured van der Waals materials," *Science*, vol. 359, no. 6378, pp. 892–896, 2018.

[3] A. A. High, R. C. Devlin, A. Dibos, M. Polking, D. S. Wild, J. Perczel, N. P. de Leon, M. D. Lukin, and H. Park, "Visible-frequency hyperbolic metasurface," *Nature*, vol. 522, p. 192, 2015.

[4] A. J. Hoffman, L. Alekseyev, S. S. Howard, K. J. Franz, D. Wasserman, V. A. Podolskiy, E. E. Narimanov, D. L. Sivco, and C. Gmachl, "Negative refraction in semiconductor metamaterials," *Nature Materials*, vol. 6, p. 946, 2007.

[5] S. Yoo, S. Lee, and Q. H. Park, "Loss-free negative-index metamaterials using forward light scattering in dielectric meta-atoms," *ACS Photonics*, vol. 5, no. 4, pp. 1370–1374, 2018.

[6] I. V. Shadrivov, A. B. Kozyrev, D. W. van der Weide, and Y. S. Kivshar, "Tunable transmission and harmonic generation in nonlinear metamaterials," *Applied Physics Letters*, vol. 93, no. 16, p. 161903, 2008.

[7] J. T. Collins, D. C. Hooper, A. G. Mark, C. Kuppe, and V. K. Valev, "Second-harmonic generation optical rotation solely attributable to chirality in plasmonic metasurfaces," *ACS Nano*, vol. 12, no. 6, pp. 5445–5451, 2018.

[8] W. L. Barnes, T. W. Preist, S. C. Kitson, J. R. Sambles, N. P. K. Cotter, and D. J. Nash, "Photonic gaps in the dispersion of surface plasmons on gratings," *Physical Review B*, vol. 51, no. 16, pp. 11 164–11 167, 1995.

[9] W. L. Barnes, T. W. Preist, S. C. Kitson, and J. R. Sambles, "Physical origin of photonic energy gaps in the propagation of surface plasmons on gratings," *Physical Review B*, vol. 54, no. 9, pp. 6227–6244, 1996.

[10] W. L. Barnes, A. Dereux, and T. W. Ebbesen, "Surface plasmon subwavelength optics," *Nature*, vol. 424, no. 6950, pp. 824–830, 2003.

[11] A. Sobhani, M. W. Knight, Y. Wang, B. Zheng, N. S. King, L. V. Brown, Z. Fang, P. Nordlander, and N. J. Halas, "Narrowband photodetection in the near-infrared with a plasmon-induced hot electron device," *Nature Communications*, vol. 4, p. 1643, 2013.

[12] R. H. Ritchie, E. T. Arakawa, J. J. Cowan, and R. N. Hamm, "Surface-plasmon resonance effect in grating diffraction," *Physical Review Letters*, vol. 21, no. 22, pp. 1530–1533, 1968.

[13] J. A. Porto, F. J. García-Vidal, and J. B. Pendry, "Transmission resonances on metallic gratings with very narrow slits," *Phys. Rev. Lett.*, vol. 83, pp. 2845–2848, Oct 1999.

[14] Q. Cao and P. Lalanne, "Negative role of surface plasmons in the transmission of metallic gratings with very narrow slits," *Phys. Rev. Lett.*, vol. 88, p. 057403, Jan 2002.

[15] C. Girard, "Near fields in nanostructures," *Reports on Progress in Physics*, vol. 68, no. 8, pp. 1883–1933, jul 2005.

[16] W. Rieger, J. J. Heremans, H. Ruan, Y. Kang, and R. Claus, "Yagi-uda nanoantenna enhanced metal-semiconductor-metal photodetector," *Applied Physics Letters*, vol. 113, no. 2, p. 023102, 2018.

[17] J. Yoon, G. Lee, S. H. Song, C.-H. Oh, and P.-S. Kim, "Surface-plasmon photonic band gaps in dielectric gratings on a flat metal surface," *Journal of Applied Physics*, vol. 94, no. 1, pp. 123–129, 2003.

[18] A. V. Zayats, I. I. Smolyaninov, and A. A. Maradudin, "Nano-optics of surface plasmon polaritons," *Physics Reports*, vol. 408, no. 3-4, pp. 131–314, 2005.

[19] E. Yablonovitch, "Photonic band-gap structures," *Journal of the Optical Society of America B*, vol. 10, no. 2, pp. 283–295, 1993.

[20] M. Javaid and T. Iqbal, "Plasmonic bandgap in 1d metallic nanostructured devices," *Plasmonics*, vol. 11, no. 1, pp. 167–173, 2016.

[21] P. B. Johnson and R. W. Christy, "Optical constants of the noble metals," *Phys. Rev. B*, vol. 6, pp. 4370–4379, Dec 1972.

[22] T. Hattori, K. Egawa, S.-i. Ookuma, and T. Itatani, "Intense terahertz pulses from large-aperture antenna with interdigitated electrodes," *Japanese Journal of Applied Physics*, vol. 45, no. No. 15, pp. L422–L424, 2006.

[23] S. K. Gray, "Theory and modeling of plasmonic structures," *The Journal of Physical Chemistry C*, vol. 117, no. 5, pp. 1983–1994, 2013.

[24] D. T. Pierce and W. E. Spicer, "Electronic structure of amorphous si from photoemission and optical studies," *Phys. Rev. B*, vol. 5, pp. 3017–3029, Apr 1972. [Online]. Available: https://link.aps.org/doi/10.1103/PhysRevB.5.3017

[25] A. S. Jermyn, G. Tagliabue, H. A. Atwater, W. A. Goddard, P. Narang, and R. Sundararaman, "Transport of hot carriers in plasmonic nanostructures," *Phys. Rev. Materials*, vol. 3, p. 075201, Jul 2019. [Online]. Available: https://link.aps.org/doi/10.1103/PhysRevMaterials.3.075201

[26] M. W. Knight, H. Sobhani, P. Nordlander, and N. J. Halas, "Photodetection with active optical antennas," *Science*, vol. 332, no. 6030, pp. 702–704, 2011.

[27] C. Zhang, G. Cao, S. Wu, W. Shao, V. Giannini, S. A. Maier, and X. Li, "Thermodynamic loss mechanisms and strategies for efficient hot-electron photoconversion," *Nano Energy*, vol. 55, pp. 164–172, 2019.

5.2 Metal Dependence

The surface plasmon wavelength, λ_{sp}, calculations presented in Chapter 4 indicate that the choice of metal is of secondary importance to the choice of dielectric in a plasmonic structure. However, if a interband transition exists in the metal at the wavelength of interest, then the choice of metal is of primary significance. The nanoscale resonance optoelectronic devices fabricated in this dissertation consist of Cr/Au on Si; Au has an interband transition occurring at free space wavelength, λ_{fs}, 550 nm. If an interband transition occurs, then it is possible to generate hot holes as well as hot electrons. Interband transitions present themselves as absorbance in the metal independent of geometry; an increase in absorbance for free space wavelengths, λ_{fs}, below 550 nm is observed in Au on Si structures as discussed in the previous section. The results presented in the previous section provide evidence that a grating structure effectively cuts off the absorbance at wavelengths below the period of the grating. In order to determine the effects of the grating structure in metals lacking an inter band transition in the visible portion of the spectrum, the absorbance in a uniform thin film and a silver grating were computed using FEM. These results as well as the magnetic field profiles at observed resonances are shown in Fig. 5.1. The presence of a maximum in absorbance occurring at a free space wavelength, λ_{fs}, indicates that not only does the grating cut off the absorbance, but also supports a resonance mode. A bimetallic interdigitated nanoscale resonance structure may provide enhance photodetection and energy harvesting, with an Au electrode producing hot holes and an Ag electrode producing hot electrons. Such a device is proposed in Chapter 6.

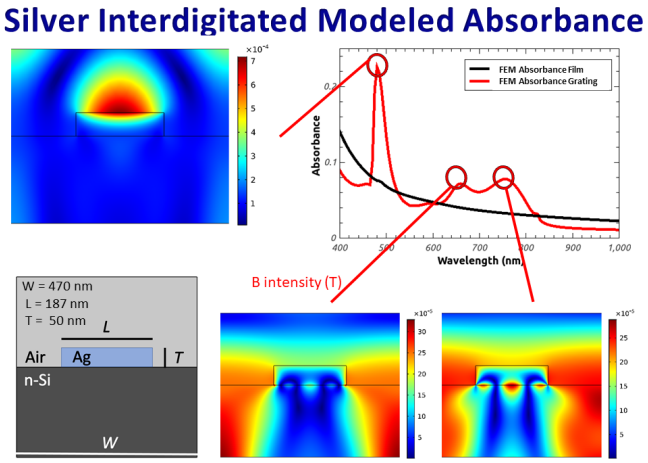

Figure 5.1: Modeled plasmonic resonances observed in Ag interdigitated structure. The black line is the FEM absorbance in a uniform Ag film on and Si substrate, and the red line is FEM absorbance for a grating structure having the geometry pictured to the bottom left. Magnetic field profiles are shown connected to the appropriate absorbance maxima.

5.3 Yagi-Uda Nanoantenna Enhanced Metal-Semiconductor-Metal Photodetector

This section was previously published as: W. Rieger *et al.*, "Yagi-Uda Nanoantenna Enhanced Metal-Semiconductor-Metal Photodetector", Appl. Phys. Lett. **113**, 023102 (2018).

William Rieger was the primary author; as such he was primarily responsible for drafting the manuscript, fabricating devices, characterizing devices, and performing effective wavelength analysis.

Yagi-Uda nanoantenna enhanced metal-semiconductor-metal photodetector

W. Rieger,[1,2] J. J. Heremans,[1,a)] H. Ruan,[2,3] Y. Kang,[2] and R. Claus[2]
[1]*Department of Physics, Virginia Tech, Blacksburg, Virginia 24060, USA*
[2]*NanoSonic, Inc., 158 Wheatland Dr., Pembroke, Virginia 24136, USA*
[3]*Department of Mechanical Engineering, Virginia Tech, Blacksburg, Virginia 24060, USA*

(Received 2 May 2018; accepted 27 June 2018; published online 12 July 2018)

An array of 400 nanolithographic Yagi-Uda antennas on a metal-semiconductor-metal rectifier photodetector demonstrates control of wavelength selectivity and directivity. The nanoantenna array response is obtained using a direct electrical measurement approach. Resonances in rectified photocurrent are detected at the incident electromagnetic radiation of free-space wavelengths 1110 nm and 1690 nm, corresponding to scaled effective wavelengths of 388 nm and 776 nm, respectively. The scaling is consistent with a theory based on plasmonic effects in nanoscale devices at optical frequencies, and the two resonant wavelength modes are found to match at, respectively, full-wavelength and half-wavelength operation of the detector dipole element. Quantum efficiencies are estimated as 5.1% and 3.1% at 1110 nm and 1690 nm wavelengths, respectively, representing a fourfold increase over a device lacking the antenna array. *Published by AIP Publishing*. https://doi.org/10.1063/1.5038339

Nanoantennas operating at optical electromagnetic wavelengths and produced on solid-state substrates using nanofabrication techniques have formed a topic of interest since nanofabrication techniques have enabled their creation. A compelling feature of such nanoantennas lies in the promise to draw from the existing knowledge of RF antennas to design optical devices with functionalities that are difficult to obtain from materials properties alone. Nanoantennas have been studied in the context of focusing electric fields in scanning tunneling microscopy,[1] controlling optical transmission and reflection through optically designed surfaces,[1–4] studying non-linear optics,[5–7] and creating frequency selective photodetectors.[8–12] Yagi-Uda nanoantennas have been of particular interest[13–17] due to the Yagi-Uda geometry being well understood, and having excellent gain and directive properties. The Yagi-Uda geometry further lends itself well to nanofabrication.

Here, we report an electrical characterization of Yagi-Uda based nanoantenna arrays fabricated on a semiconductor surface where Schottky barriers are formed at the antenna-semiconductor interface. Such a structure is built into a metal-semiconductor-metal (MSM) electronically rectifying detector device to collect the photocurrent when the nanoantenna is photoexcited. The approach allows implementation of optically designed surfaces to practical photodetectors to achieve higher functionalities and efficiencies. Two aspects differentiating nanoantennas from macroscopic RF antennas underlie the present work. First, a loss of linearity in antenna scaling with wavelength occurs as wavelength and concomitant antenna element size are reduced. Plasmonic effects dominate at these length scales causing the loss in linearity and must be accounted for in design dimensions. Second, nanoantennas fabricated on substrates have a nonsingular feed point, arising from the impracticality of achieving the necessarily small electrical connections. Most nanoantenna studies to date, with exceptions,[8–12] have focused on optical measurement techniques, with interrogation occurring via optical transmission, reflection, and absorption. Although an effective means of determining resonant behavior, optical measurements limit real-world applicability. Since nanoantennas lack a singular feed point, concepts such as impedance and standing wave ratio, inherent to RF antenna design, now lack definite meaning. Instead, the whole system must be considered to recover equivalent concepts. Despite the differences, concepts of macroscopic RF antennas retain their usefulness to characterize solid-state nanoantennas and a basis for the present work is formed by a theoretical link derived between RF antennas and nanoantennas using the concept of effective wavelengths.

The nanoantenna characterization method used in this work consists of a direct electrical measurement of the rectified photocurrent generated by the nanoantennas, representing a step beyond nanoantenna work relying on optical characterization. While a rectified photocurrent measurement using an indium tin oxide (ITO) film and a back electrode has appeared,[8–12] the present work employs a measurement scheme omitting the ITO layer and directly measuring the photocurrent injected into the Si by the electric field concentrations at the nanoantenna elements. A MSM Schottky junction photodiode is formed, where the nanoantenna elements form one metal electrode, the Si forms the semiconductor, and two macroscopic Au counter contacts deposited on the Si form two other metal electrodes between which a voltage bias is applied. Photocurrent is measured across the resulting MSM diode. Photocurrent rectification from optical frequencies to low frequencies for lock-in amplifier detection (17 Hz) is achieved by the two junctions in the MSM diode, one of which is forward biased and the other reverse biased. Figure 1(a) depicts a schematic of the photocurrent measurements, and Figs. 1(b)–1(e) depicts aspects of the nanoantenna devices and measurements, as explained below. Generation of photocurrent is a multi-step process. This

a)Author to whom correspondence should be addressed: heremans@vt.edu

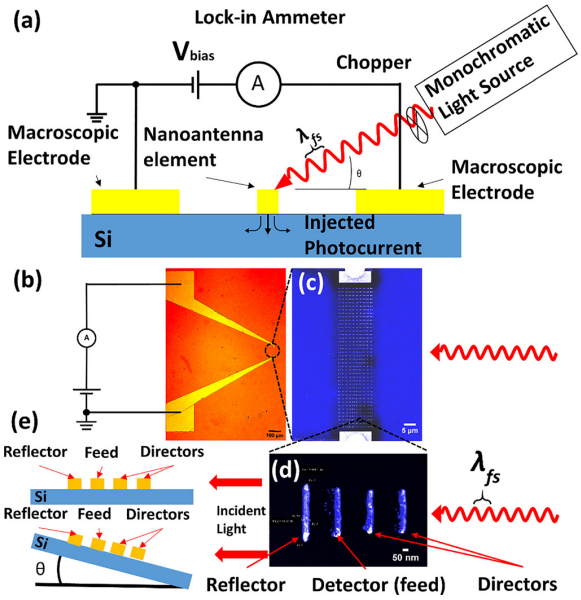

FIG. 1. (a) Schematic of the experimental setup and measurement scheme. Chopped monochromatic light is incident on the device at an angle, θ. (b) Enlarged view of the device highlighting the macroscopic electrodes. (c) SEM micrograph of the entire antenna array, with 400 Yagi-Uda nanoantennas occupying the space between the electrodes. (d) SEM micrograph of a single Yagi-Uda nanoantenna. Each nanoantenna is comprised of 4 elements with dimensions listed in Table I. (e) Side view of the measurement setup indicating angle, θ, of incident monochromatic light.

process begins when the nanoantenna is illuminated with an appropriate wavelength to excite plasmons in the antenna devices. These plasmons can decay along multiple pathways.[18] The possible pathways include transfer of energy to phonons, reradiation, and injection of a hot electron into the metallic structure. If the injected hot electron is sufficiently energetic, it can overcome the Schottky barrier and move to the conduction band of the semiconductor [Fig. 1(a)].

The nanoantennas were fabricated on an n-Si (100) wafer, from which SiO_2 was removed by a buffered oxide etch. Photolithography, deposition of 10 nm Cr and 50 nm Au, and lift-off then created macroscopic electrodes with fingers extending towards the device area [Fig. 1(b)]. These macroscopic electrodes allow electrical connections to the measurement setup [Figs. 1(a) and 1(b)]. Subsequent electron-beam lithography, deposition of 10 nm Cr and 50 nm Au, and lift-off then created an array of 400 individual Yagi-Uda nanoantennas as well as rectangular electrodes flanking the array and overlapping the photolithographic electrodes [Fig. 1(c)]. As reference, a "blank" device was also produced, lacking only the array of nanoantennas. The dimensions of the nanoantenna elements on the active device are listed in Table I, and Fig. 1(d) depicts an individual nanoantenna. Each nanoantenna consists of nanorod elements assuming the roles of directors, reflector, and feed elements, equivalents to the elements of macroscopic Yagi-Uda antennas. In this work, we will refer to the feed element as the detector element, as the nanoantennas are operated in the receiving rather than the transmitting mode. The nanoantennas were initially designed to detect a free-space incident

TABLE I. Design dimensions for the Yagi-Uda nanoantenna elements given $\lambda_{eff} = 776$ nm. Elements have a measured width of 58 nm. Elements have a height of 60 nm (10 nm Cr/50 nm Au). The uncertainty in the measured length across the array is ±5 nm.

Element	Design dimensions	Designed lengths (nm)	Measured lengths (nm)
Reflector	$\lambda_{eff}/1.75$	443	464
Detector	$\lambda_{eff}/2$	388	406
Directors	$\lambda_{eff}/2.25$	345	357
Element spacing	$\lambda_{eff}/3$	258	264

light wavelength λ_{fs} in the IR region of the spectrum, namely, $\lambda_{fs} \sim 1500$ nm. The effective incident wavelength λ_{eff} experienced by the nanoantennas differs from λ_{fs}, as detailed below.[19] Investigating the relation between λ_{eff} and λ_{fs} for Yagi-Uda geometries forms one of the aims of this work. A preliminary estimate of λ_{eff} given $\lambda_{fs} \approx 1500$ nm yields $\lambda_{eff} \approx 776$ nm, and hence $\lambda_{eff} = 776$ nm formed the starting point of the design in Table I. The designed lengths in Table I denote the nominal lithographic dimensions whereas measured lengths were evaluated from SEM micrographs.

The measurement setup consists of a broadband light source, an optical chopper operating at 17 Hz, a monochromator, a 3-axis translation and single-axis rotation sample stage, and a lock-in ammeter. The power density of the incident light is ~ 0.25 W/m^2. Translation adjustments are used to center the device [Figs. 1(a)–1(e)] in the illuminated spot at a constant distance of 10 cm from the monochromator aperture. The rotation axis allows the angle of incidence, θ, of the incident light to vary from the glancing ($\theta \approx 0°$) to normal angle ($\theta = 90°$) to the device plane [Figs. 1(d) and 1(e)]. The sample stage is enclosed in a metal enclosure shielding the photocurrent measurement from ambient light and stray electric fields. The device was biased at 1.0 V DC and the chopped photocurrent was measured by the lock-in amplifier. The incident λ_{fs} was varied from 1000 nm to 2000 nm. Measurements were obtained on both the nanoarray sample and blank sample, each at glancing angle ($\theta \approx 0°$) and at $\theta = 45°$.

Assuming a standard Yagi-Uda antenna directivity,[15–17] at $\theta \approx 0°$ the incident light wave vector is nearly aligned with the main lobe of the Yagi-Uda antenna receiving and transmitting directivity, while at $\theta = 45°$, the incident light wave vector alignment is not expected to coincide with the main lobe or side lobes. Half angular widths of Yagi-Uda antennas are found to be less than 32.5°.[16] Measurements of photocurrent *vs* λ_{fs} are depicted in Figs. 2(a) and 2(b) for $\theta \approx 0°$ and $\theta = 45°$, respectively, for the nanoantenna sample and blank reference sample. Figure 2(a) indicates two resonances for $\theta \approx 0°$, for which photocurrent reaches a maximum in the nanoantenna sample, namely, at $\lambda_{fs} = 1110$ nm and at $\lambda_{fs} = 1690$ nm. As a reference, the photocurrent measurement in the blank sample for $\theta \approx 0°$ does not show resonances [Fig. 2(a)]. Likewise, in contrast to the measurement at $\theta \approx 0°$, data for $\theta = 45°$ does not indicate clear resonances [Fig. 2(b)]. A higher average photocurrent is measured for $\theta = 45°$ indicating that more hot electrons are generated with the 45° illumination. The comparison between data for $\theta \approx 0°$ and data for $\theta = 45°$ is consistent with the expected

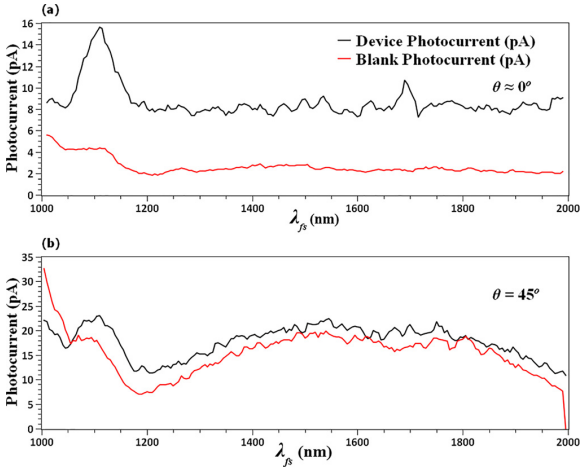

FIG. 2. (a) Photocurrent data *vs* λ_{fs}, for $\theta \approx 0°$. The black line represents the measured photocurrent on the nanoantenna device and the red line on the blank device. The nanoantenna device shows maxima at 1110 nm and 1690 nm corresponding to Yagi-Uda nanoantenna resonances. The blank device does not show resonances. (b) Photocurrent data *vs* λ_{fs}, for $\theta = 45°$. The black line represents the measured photocurrent on the nanoantenna device and the red line on the blank device. Consistent with the directivity of a Yagi-Uda antenna, no discernable maxima appear on a background showing broad features.

directivity of the Yagi-Uda nanoantennas, and the values where resonances are detected are consistent with the scaling properties of nanoantennas, as explained below.

The responsivities of the nanoantenna sample at $\theta \approx 0°$ are estimated at 46 mA/W at $\lambda_{fs} = 1110$ nm and at 31 mA/W at $\lambda_{fs} = 1690$ nm. The resulting quantum efficiencies are estimated at 5.1% and 3.1%, respectively. The responsivities of the blank sample are estimated at 11 mA/W at $\lambda_{fs} = 1110$ nm and at 5.7 mA/W at $\lambda_{fs} = 1690$ nm, yielding estimated quantum efficiencies of 1.2% and 0.64%, respectively. The nanoantenna sample thus shows quantum efficiencies increased fourfold over the blank sample. To improve the quantum efficiencies over this prototype nanoantenna sample, several avenues towards optimization are available, e.g., using the spatial distribution of the response. The array in the present work causes each nanoantenna to cast a shadow on the nanoantennas behind it. Thus, the nanoantennas on the array's leading edge contribute more to the photocurrent. Additionally, the band bending does not fall uniformly over the biased MSM device's cross-section. Further, the nanoantennas nearest the forward biased electrode are expected to contribute more to the photocurrent because the hot electrons are more likely to reach this electrode before experiencing energy loss.[20] The three mentioned effects will give rise to a spatial dependence of the response. The effects can be used towards an optimization of quantum efficiency, by using a lattice other than square to reduce shadowing, by changing the aspect ratio of the array to locate a larger number of nanoantennas closer to the electrodes and within regions of higher band bending, and by increasing the bias voltage[21] such that the hot electrons generated closer to the reverse biased electrode are more likely to reach the forward biased electrode. Additionally, Yagi-Uda antennas show a dependence on polarization, and higher efficiencies will result from a polarized light source at the correct orientation. Since RF Yagi-Uda antennas are very efficient and MSM structures can show high quantum efficiencies,[21] future optimized devices can reach higher quantum efficiencies, while retaining the observed selectivity and directivity.

A useful aspect of RF antenna designs is a linear scaling of antenna geometry with the free-space wavelength, inherent in free-space electromagnetism. This linear scaling fails due to materials properties for λ_{fs} below the millimeter wave region. At these shorter wavelengths, the electric fields in the antenna elements assume a complicated pattern and are described by oscillations of free electrons in or on the surface of the metal antenna structure. These surface plasmons are of particular interest to the study of nanoantennas because they are able to couple to free-space electromagnetic waves.[22,23] The coupling of surface plasmons on a nanoantenna to incident light yields an effective wavelength, namely, the wavelength of free-space electromagnetic radiation that couples to the resonant plasmon oscillation. Theoretically, a scaling exists for these antennas, and a specific relation has been derived for antennas consisting of rod-like elements with a diameter much less than the wavelength of interest.[19] The scaling is derived by forcing a surface plasmon on a rod-like element. The element is considered as a cylindrical wave guide with boundary conditions for TM mode oscillations. Requiring the existence of these modes yields a relation between the free-space incident λ_{fs} and an effective incident wavelength λ_{eff} experienced by the nanoantenna.[19] As an approximation for the present Yagi-Uda nanoantennas, the following relation between λ_{fs} and λ_{eff} is used:[19]

$$\lambda_{eff} = \frac{\lambda_{fs}}{K}\sqrt{\frac{4\pi^2 K\left(R^2/\lambda_{fs}^2\right) z\left(\lambda_{fs}, K\right)}{1 + 4\pi^2 K\left(R^2/\lambda_{fs}^2\right) z\left(\lambda_{fs}, K\right)}} - \lambda_c. \qquad (1)$$

In this expression, K indicates the relative permittivity of the dielectric (assumed uniform) in which the nanoantenna is embedded and λ_c indicates a capacitive contribution depending on the end radius R of the nanorod elements.[19] For perfect hemispherical nanorod ends, theory yields $\lambda_c = 4R$. Since the rod ends of the actual nanoantennas are likely not hemispherical and hence not characterized by fixed R, λ_c will be treated as an adjustable parameter to fit the measurements. Further, K is assumed real for a dielectric, and in the IR range of λ_{fs}, for Si $K \approx 3.5$ is estimated. Yet, the Au nanorods are deposited on Si ($K \approx 3.5$) and are exposed to ambient air ($K = 1$) at their free surfaces. Hence, K is also regarded as an adjustable parameter, with a physically acceptable range of values.

Figure 3 contains representative plots of λ_{eff} *vs* λ_{fs} (nearly straight lines) and indicates the influence of both K (effective dielectric medium) and λ_c (nanorod geometry), thereby highlighting their effect in understanding the measured incident λ_{fs} at resonance in terms of the calculated λ_{eff}. We note that in the relation of λ_{eff} *vs* λ_{fs}, varying K changes the slope and the intercept, while varying λ_c changes the intercept only. Figure 3 highlights the value $\lambda_{eff} = 776$ nm, of relevance if the length of the detector nanorod of each Yagi-Uda nanoantenna corresponds to approximately half λ_{eff}

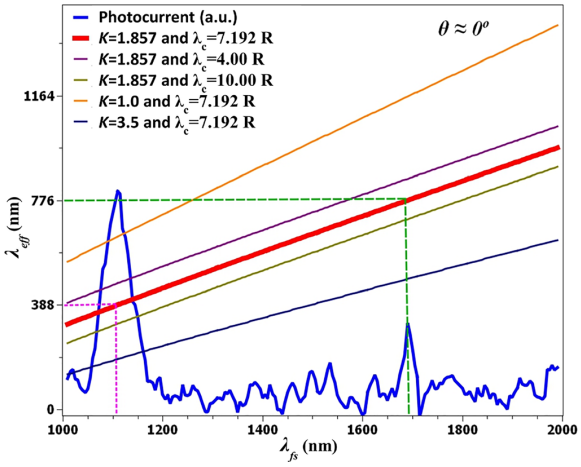

FIG. 3. Glancing angle ($\theta \approx 0^\circ$) photocurrent data *vs* λ_{fs}, superimposed on λ_{eff} *vs* λ_{fs} as calculated from Eq. (1). For $K = 1.857$ and $\lambda_c = 7.192R$, Eq. (1) provides a best-fit correspondence between $\lambda_{eff} = 776$ nm and $\lambda_{eff} = 388$ nm and the two values of λ_{fs} where a photocurrent resonance is observed. For comparison, four other curves of λ_{eff} *vs* λ_{fs} calculated from Eq. (1) are shown, for various K and λ_c bracketing the best-fit values.

(half-wavelength resonant mode or first excited mode operation, the usual design operation for Yagi-Uda antennas), and highlights the value $\lambda_{eff} = 388$ nm, of relevance if the length of the detector nanorod corresponds to approximately a full λ_{eff} (full-wavelength resonant mode or second excited mode operation). In the fabricated nanoantennas, the rod ends are not perfect hemispheres and they possess a textured surface expected to increase the capacitance due to the nanorod ends, resulting in increased λ_c. Regarding K, an effective value $1.0 \leq K \leq 3.5$ is expected as an intermediate value for K between Si and air. As indicated in Fig. 3, Eq. (1) yields a best-fit correspondence (red line) between $\lambda_{eff} = 776$ nm and $\lambda_{eff} = 388$ nm and the two values of λ_{fs}, where a photocurrent resonance is observed (respectively, $\lambda_{fs} = 1110$ nm and $\lambda_{fs} = 1690$ nm) for $K = 1.857$ and $\lambda_c = 7.192R$. The best-fit value $\lambda_c > 4R$ is consistent with expectations and physically reasonable. The best-fit value $1.0 \leq K = 1.86 \leq 3.5$ is also consistent with the nanoantennas experiencing an effective dielectric medium intermediate between Si and air, as mentioned. Hence, Fig. 3 shows that the scaling between λ_{eff} *vs* λ_{fs} implied by Eq. (1) is consistent with the experimental results, when the dielectric environment and geometrical capacitive coupling effects are taken into account. The photocurrent measurements contained in Figs. 2(a) and 2(b) then also form a strong indication that the nanoantenna array shows the wavelength selectivity and the directivity expected from the Yagi-Uda geometry, and that nanoantennas can be used to impart these properties to a photodetector.

In conclusion, the present work advances the study of optical nanoantennas by using a fabrication process which integrates nanoantennas in a metal-Si-metal rectifier photodiode. The Yagi-Uda nanoantennas demonstrate wavelength selectivity and directivity. The wavelength selectivity follows a predictive scaling rule based on plasmonic effects, and is dependent on an effective discontinuous dielectric environment as well as on geometrical effects expressed via capacitive coupling to the environment. Future work can be directed at more refined photocurrent or signal extraction by optimized electron injection, at measuring the sensitivity to polarization of the nanoantennas, and at scaling to wider ranges of wavelengths in the IR and visible regions of the spectrum.

See supplementary material for current-voltage characteristics of the MSM structure and for information about the choice of the voltage bias point.

This work is based on support by the U.S. Navy under Contract No. N68335-13-C-0184 and NASA under Contract No. NNX17CC63P. W. Rieger would like to disclose a financial interest in NanoSonic, Inc. The authors acknowledge Mr. David Allocca and Dr. Robert Romanofsky for the insights and useful discussions of this work.

[1]P. Bharadwaj, B. Deutsch, and L. Novotny, Adv. Opt. Photonics **1**(3), 438–483 (2009).
[2]L. Novotny and N. van Hulst, Nat. Photonics **5**(2), 83–90 (2011).
[3]I. S. Maksymov, I. Staude, A. E. Miroshnichenko, and Y. S. Kivshar, Nanophotonics **1**(1), 65–81 (2012).
[4]X. Ni, N. K. Emani, A. V. Kildishev, A. Boltasseva, and V. M. Shalaev, Science **335**(6067), 427 (2012).
[5]X. Y. Xiong, L. J. Jiang, W. E. Sha, Y. H. Lo, and W. C. Chew, Sci. Rep. **6**, 18872 (2016).
[6]A. C. Lesina, P. Berini, and L. Ramunno, Opt. Mater. Express **7**(5), 1575–1580 (2017).
[7]B. Metzger, M. Hentschel, and H. Giessen, Nano Lett. **17**(3), 1931–1937 (2017).
[8]B. Y. Zheng, Y. Wang, P. Nordlander, and N. J. Halas, Adv. Mater. **26**(36), 6318–6323 (2014).
[9]A. Sobhani, M. W. Knight, Y. Wang, B. Zheng, N. S. King, L. V. Brown, Z. Fang, P. Nordlander, and N. J. Halas, Nat. Commun. **4**, 1643 (2013).
[10]S. Piltan and D. Sievenpiper, J. Appl. Phys. **122**(18), 183101 (2017).
[11]M. W. Knight, H. Sobhani, P. Nordlander, and N. J. Halas, Science **332**(6030), 702–704 (2011).
[12]M. W. Knight, L. Liu, Y. Wang, L. Brown, S. Mukherjee, N. S. King, H. O. Everitt, P. Nordlander, and N. J. Halas, Nano Lett. **12**(11), 6000–6004 (2012).
[13]A. G. Curto, G. Volpe, T. H. Taminiau, M. P. Kreuzer, R. Quidant, and N. F. van Hulst, Science **329**(5994), 930–933 (2010).
[14]T. Kosako, Y. Kadoya, and H. F. Hofmann, Nat. Photonics **4**(5), 312–315 (2010).
[15]L. Ma, J. Lin, Y. Ma, B. Liu, J. Tan, and P. Jin, Opt. Commun. **368**, 197–201 (2016).
[16]I. S. Maksymov, A. R. Davoyan, A. E. Miroshnichenko, C. Simovski, P. Belov, and Y. S. Kivshar, Opt. Commun. **285**(5), 821–824 (2012).
[17]D. Dregely, R. Taubert, J. Dorfmuller, R. Vogelgesang, K. Kern, and H. Giessen, Nat. Commun. **2**(4), 267 (2011).
[18]E. W. McFarland and J. Tang, Nature **421**, 616 (2003).
[19]L. Novotny, Phys. Rev. Lett. **98**(26), 266802 (2007).
[20]Y. Gu, J. P. Romankiewicz, J. K. David, J. L. Lensch, and L. J. Lauhon, Nano Lett. **6**(5), 948–952 (2006).
[21]J. Burm, K. I. Litvin, D. W. Woodard, W. J. Schaff, P. Mandeville, M. A. Jaspan, M. M. Gitin, and L. F. Eastman, IEEE J. Quantum Electron. **31**(8), 1504–1509 (1995).
[22]W. L. Barnes, A. Dereux, and T. W. Ebbesen, Nature **424**, 824 (2003).
[23]A. V. Zayats, I. I. Smolyaninov, and A. A. Maradudin, Phys. Rep. **408**(3–4), 131–314 (2005).

5.4 Yagi-Uda Nanoantenna Structures for Infrared Detection Using Si

William Rieger was the primary author; as such he was primarily responsible for drafting the manuscript, fabricating devices, characterizing devices, and performing effective wavelength analysis.

Yagi-Uda Nanoantenna Structures for Infrared Detection Using Silicon

William T. Rieger Jr.*, Jean J. Heremans*, Hang Ruan†‡, Yuhong Kang† and Richard O. Claus†
*Department of Physics
Virginia Tech, Blacksburg, Virginia 24061
Email:wrieger@vt.edu
†NanoSonic Inc. Pembroke, VA 24136
‡Department of Mechanical Engineering
Virginia Tech, Blacksburg, Virginia 24061

***Abstract*—Detection of light below band gap energies using nanolithographic Yagi-Uda antennas is discussed. Two nonlinear mechanisms contributing to generation of photocurrent are identified and evaluated. Results of a Si near-IR photodetector are presented and application to mid-IR discussed. Additionally, finite element modeling methods are employed.**

I. Introduction

Nanoantennas have been used successfully to increase photodetection beyond the limits of semiconductor material properties. [1][2][3][4]This above band gap detection is possible because of the plasmonic nonlinear conversion of incident radiation; this nonlinear process is responsible for high reported quantum efficiencies. The nonlinear photocurrent generation is caused by at least two phenomena—"hot" electron injection[2] and higher harmonic reradiation.[5][6] When incident light excites surface plasmons in the antenna structure, they may decay along a number of pathways, some of which contribute to the photocurrent. Resonant surface plasmons are capable of transferring large amounts of kinetic energy to valence electrons within the metal—resulting in hot electrons. If these electrons exhibit energies above the metal-semiconductor interface barrier energy then the hot electrons are free to move into the semiconductor. Resonant surface plasmons may also decay by reradiating. The frequency of this reradiated light can be the same as the plasmon resonance or an integer multiple of the original frequency. In this manner near-IR photons are converted to visible via second harmonic reradiation and mid-IR radiation can be converted to visible via third or fourth harmonic reradiation. Here, a Si based Metal-Semiconductor-Metal (MSM) photodiode is used concurrently with an array of 400 nanolithographic Yagi-Uda antennas; an example of these is depicted in Figure 1. The resulting wavelength selectivity and directivity are engineered in the near IR with photon energies below the band gap of Si. Current limiting factors for nanoantenna structures center around the tendency of surface plasmons to decay along pathways that do not contribute to the photocurrent.

II. Methods

Nanoantennas are frequently fabricated on transparent surfaces and interrogated using purely optical methods. Here an electrical interrogation method is employed where the nanoantennas are used as a sensitizing agent in the semiconductor region of a MSM structure. This method uses hot injection methods similar to the ITO-based measurement scheme, however represents a simplification requiring only a metallic monolayer on a silicon substrate. In addition to hot electron injection, second and third harmonic generation may contribute to the measured photocurrent. Electrical characterization of nanoantennas in realistic environments is a necessary step towards their useful application; testing in real life conditions is necessary because much like their RF counterparts, nanoantennas are affected by their environment. In particular the introduction of a dielectric/semiconducting substrate serves to shorten the effective wavelength.

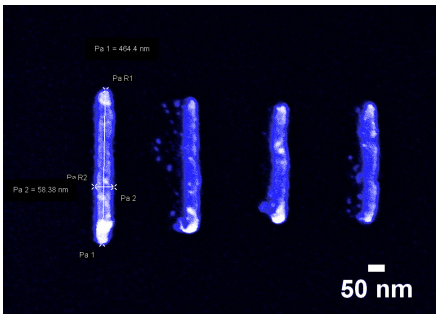

Fig. 1. Single nanolithographic Yagi-Uda antenna. Design and actual dimensions are given in Table I. The measured device includes an array of 400 such devices between the electrodes of a Metal-Semiconductor-Metal photodiode.

A. Fabrication

Devices were fabricated on n-Si $< 100 >$ from which a protective oxide layer was removed using 6:1 buffered oxide etch. A simplified MSM structure was fabricated using photolithography. Thermal evaporation and lift-off were used to obtain 10 nm Cr and 50 nm. Following deposition of the MSM structure an array of 400 Yagi-Uda antennas was patterned using electron beam lithography. Cr/Au was deposited in the same manner as the previous step, leaving a metallic monolayer on the surface of the Si substrate.

TABLE I
DESIGN AND FABRICATED DIMENSIONS FOR ANTENNAS WITHIN AN ARRAY. ELEMENTS ARE 60 NM HIGH AND MEASURED DIMENSIONS HAVE UNCERTAINTY ± 5 NM.

Element	Design Lengths (nm)	Measured Lengths (nm)
Reflector	443	464
Detector	388	406
Director	345	357
Element Spacing	258	264
Element Width	50	58

B. Experimental Setup

Characterization of the antenna array involved use of optical and electrical methods. Optically a collimated white light source was used concurrently with a monochromator from a spectroscope. The output of the spectroscope emitting monochromatic light was directed to be incident to the sample. A 17 Hz chopper was placed in the optical pathway before the monochromator. A stage was fabricated to allow the angle of incidence of light on the sample to be adjusted in the plane orthogonal to the length of the antenna elements. Electrically, the fingers of the MSM photodiode were biased at 1 VDC and the photocurrent was measured using lock-in detection referenced to the chopper. Measurements were obtained at two angles of incidence; glancing—where incident light was aligned with the directivity of the antennas—and 45 degrees—where the incident light was sufficiently far from the antenna directivity to reduce the antenna effect.

C. Finite Element Modeling

In order to predict nanoantenna behavior and calculate effective wavelengths more accessibly, finite element modeling has been used. Modeling efforts use COMSOL Multiphysics Wave Optics Module. Modeled results are solved for in the frequency domain, using a range of angles of incidence and polarization orientations. Material properties are modeled using the Lorentz-Debye model. Preliminary results indicate clear resonances of the modeled structure.

III. RESULTS

Two resonance peaks were identified in the glancing results at 1110 nm and 1690 nm, as observed in Figure 2. These resonances have a harmonic relationship that is consistent with effective wavelength theory.[7] Results at a 45 degree angle do not exhibit these resonances, consistent with the expected Yagi-Uda directivity.[4] Estimated quantum efficiencies are 5.1% and 3.1% for the two resonance peaks, respectively. The non-optimal quantum efficiencies are likely due to the decay of plasmons along pathways that do not contribute to the photocurrent; current research efforts are focused on this aspect.

IV. CONCLUSION

Nanoantennas represent a method of utilizing nonlinear plasmonic effects to generate photocurrent from below

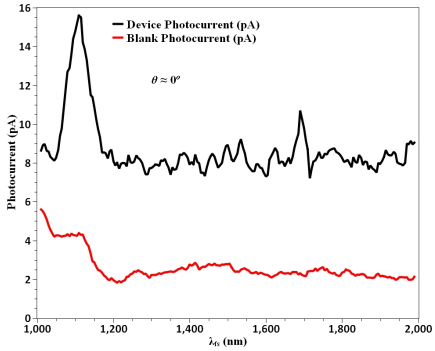

Fig. 2. Results of device illuminated at a glancing angle. The device includes an array of 400 Yagi-Uda nanoantennas as in Figure 1, oriented in such a way that the electrodes do not cast a shadow on the device. Measurements were obtained at a bias of 1 VDC. A "blank" device was also fabricated lacking only the antenna array. Clear resonances can be observed at 1110 nm and 1690 nm

bandgap energy photons. While current work has focused on near-IR where second harmonic generation is sufficient to reach band gap energies, further efforts focus on more efficiently generating third and fourth harmonics allowing mid-IR detection using nanoantennas. Similarly, nanoantenna structures can be employed as novel materials effectively decreasing the band gap energies by a factor of 2 based on second harmonic generation. In addition to reradiation of higher harmonics, hot electron injection also contributes to the photocurrent. Current/future work in this area involves using finite element methods (COMSOL Multiphysics) to computationally determine effective wavelength for realistic structures.

ACKNOWLEDGMENTS

The authors would like to thank Robert Romanofsky for many helpful discussions.

REFERENCES

[1] W. Rieger, J. J.Heremans, H. Ruan, Y. Kang and R. Claus, "Yagi-Uda nanoantenna enhanced metal-semiconductor-metal photodetector," *Applied Physics Letters,* vol. 113, pp. 023102, July 2018.
[2] M. W. Knight, H. Sobhani, P. Nordlander, and N. J. Halas, "Photodetection with Active Optical Antennas," *Science,* vol. 332 no. 6030, pp. 702–704, May 2011.
[3] P. Bharadwaj, B. Deutsch, and L. Novotny, "Optical Antennas," *Advances in Optics and Photonics,* vol. 1, no. 3, pp. 438–483, August 2009.
[4] I. S. Maksymov, I. Staude, A. E. Miroshnichenko, and Y. S. Kivshar, "Optical Yagi-Uda Antennas," *Nanophotonics,* vol. 1, no. 1, pp. 65–81, April 2012.
[5] B. Metzger, M. Hentschel, and H. Giessen, "Probing the Near-Field of Second Harmonic Light around Plasmonic Nanoantennas," *Nano Letters,* vol. 17, no. 3, pp. 1931–1937, February 2017.
[6] A. C. Lesina, P. Berini, and L. Ramunno, "Origin of the Third Harmonic Generation in Plasmonic Nanoantennas," *Optical Materials Express,* vol. 7, no. 5 pp. 1575–1580, May 2017.
[7] L. Novotny, "Antennas for Light," *Physical Review Letters,* vol. 98, no. 26, pp. 266802, February 2007.

Chapter 6

Conclusion

The work described in this dissertation represents a thorough investigation of nanoscale resonant structures for novel optoelectronic sensing applications. The work included developing an experimental process whereby monolithic nanoscale resonance structures were fabricated on semiconducting substrates. Finite element modeling (FEM) was also used to investigate nanoscale resonant optoelectronic devices, and identify the mechanism or mechanisms responsible for observed photoresponses. The fabrication process developed and the device structure employed are simpler than alternative methods; they do not require the use of a transparent conductor (i.e. indium tin oxide) as in alternative optoelectronic methods [61]. This simplification combined a standard monolithic photodetector structure and a metal-semiconductor-metal (MSM) photodiode coupled with hot carrier injection. Because MSM photodiodes consist of a metallic monolayer they may be easily and efficiently integrated into standard CMOS processes. Beyond the practical interest in novel optoelectronic devices, further understanding surface plasmon resonance (SPR), hot carrier generation, and hot carrier transport in metal-semiconductor heterostructures is of significant academic interest. The methods and devices discussed in this dissertation offer a probe of SPR, hot carrier generation, hot carrier transport, and other topics. The optoelectronic characterization method developed consists of a white light source, chopper, collimating lenses, mirrors, a diffraction grating, optical slits, and electronic test equipment. Low noise measurements were achieved through the use of an optical chopper and a lock-in amplifier referenced to the chopper. Using this technique, strongly directive and wavelength selective photocurrents were observed for an array of Yagi-Uda nanoantennas. Maxima in observed photocurrents occurred at free space wavelengths, λ_{fs}, 1110 nm and 1690 nm; these maxima are believed to be harmonically related and correspond to effective wavelengths, λ_{eff}, 388 nm and 776 nm respectively. This harmonic relationship is indicated by the power loss profiles discussed in Chapter 4. A grating structure was also studied within the visible portion of the spectrum. The use of a plasmonic structure resonant in the visible region of the spectrum and existing on a Si substrate is unique, contrasting to the majority of the published literature as well as to previously discussed Yagi-Uda devices which operate at energies smaller than the band

gap energy. Moreover, a broadening of the optical bandwidth has been observed in a grating based detector. By introducing a grating having a period of 470 nm onto an Si substrate a maximum in photovoltage was observed at approximately 500 nm. By comparing the observed photovoltage with FEM modeled absorbances both in the metal structure, and the Si substrate, it is clear that the photovoltage is due to both hot carriers generated in the metal and electron-hole pairs produced in the substrate. While the FEM model approach used in this dissertation is not able to directly compute photocurrents or photovoltages, the FEM absorbances and electromagnetic field profiles provide valuable insight into carrier generation mechanisms. Through comparison with literature measured photocurrents in grating structures it is evident that FEM absorbances in the metal are in good qualitative agreement with experiment. This agreement supports the understanding that photocurrents originate from hot carrier generation in the metal. Comparison of experimentally measured photovoltage with FEM absorbance in the 470 nm grating device indicates that hot carrier generation in the metal is not the only contributing mechanism. Non-negligible absorbance in the Si suggests that electron-hole pairs are being produced in the Si. The experimental photovoltage was in good qualitative agreement with the sum of the FEM absorbances in the metal and Si.

6.1 Future Work

The next logical step in the continuation of this work is the modification of the preliminary modeling work by Jermyn et al. [71] into a specific, quantitative model for nanoscale resonance optoelectronic devices. The new model will consist of three main pieces: a DFT based material model, FEM electric field profiles, and state-resolved hot carrier generation and transport. Figure 6.1 depicts the three model pieces and how they interconnect. The probability of hot carrier generation is driven by two main factors: the local electric field intensity, and the available electronic states within the material. This can be expressed as [71]:

$$P(t=0) = \frac{1}{h}\vec{E}(\vec{r}) \cdot Im\bar{\epsilon}(\omega, s) \cdot \vec{E}(\vec{r}) \tag{6.1}$$

where $\bar{\epsilon}$ is the dielectric constant tensor of the material from a specified state, $s = n\vec{k}$. n is the band index, and $\vec{k}$ the state momentum. $P(t=0)$ is the probability that a hot carrier will be generated in state s, position $\vec{r}$, for light of incident frequency ω. Hot carrier generation can occur directly, when the electric field transfers the appropriate energy and momentum to excite an electron or hole into a more energetic vacant state. Indirect hot carrier generation is also possible. Indirect hot carrier generation occurs when lattice vibrations (phonons) interact with the electron and electric field to provide energy or momentum to facilitate an electron or hole to be excited into a vacant more energetic state. The dielectric tensor, $\bar{\epsilon}$, is in general anisotropic, and may be computed by DFT. The electric field $\vec{E}(\vec{r})$ in equation 6.1 will be calculated using FEM. Equation 6.1 provides the state-resolved initial hot carrier

distribution. Information about the time evolution of the hot carriers requires knowledge of the transport properties in the material. These can be calculated in the form of the collision matrix and the collision integral. These account for both electron-electron scattering as well as electron-phonon scattering. The photocurrent should be equal to the flux of of hot carriers incident on the metal-semiconductor surface with energy above the barrier energy times the charge of the carrier.

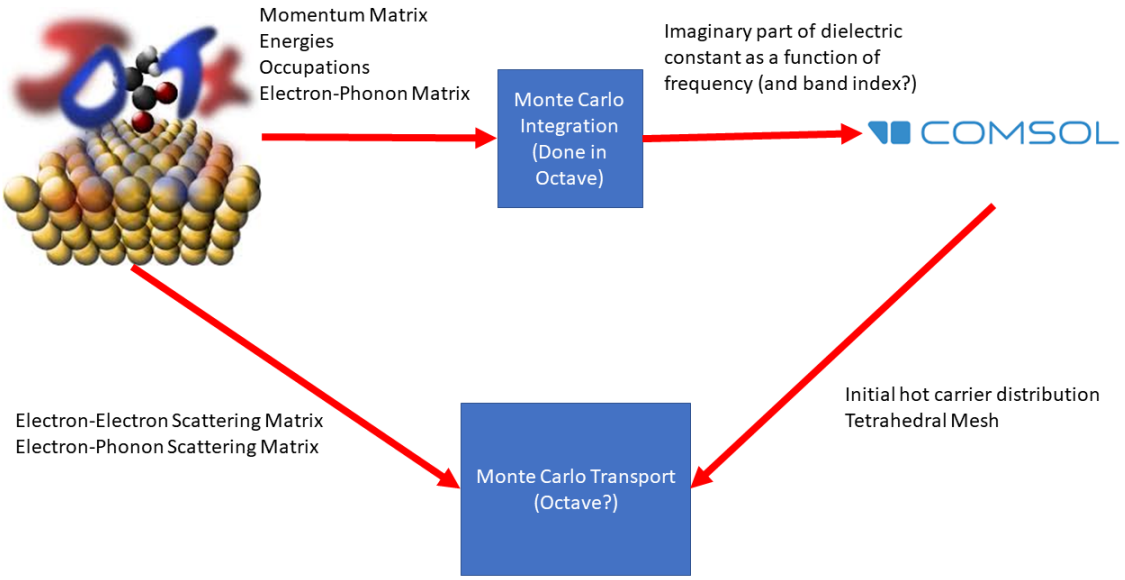

Figure 6.1: Schematic representation of proposed total model based on Jermyn *et al.* [71]. Open source DFT software (JDFTx) will be used to determine the state-resolved material properties. COMSOL® will be used as in this dissertation to compute electric field profiles. The blue boxes indicate code that will have to be developed to compute the initial distribution of hot carriers, and their time evolution.

6.2 Optimized Device

The lessons learned over the course of this dissertation have been compiled into a new proposed device. This optimized device takes the form of three main pieces: an electrode that is optimized for hole generation, an electrode that is optimized for hot electron generation, and a high-mobility semiconducting substrate. Such a device is shown in Fig. 6.2. The hot electron producing electrode should be a metal that does not have an interband transition at the energy of the incident light. By contrast, the hot hole producing electrode should be a metal or heavily doped semiconductor that does have an interband transition at the energy

of the incident light. The high-mobility semiconducting substrate may be a two-dimensional material such as a transition metal dichalcogenide.

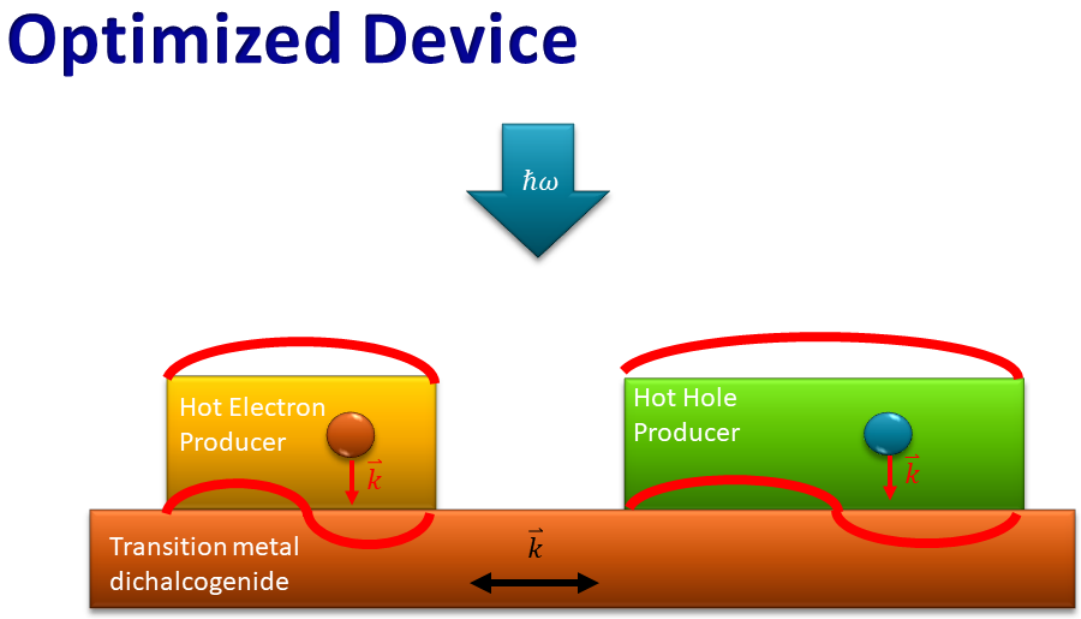

Figure 6.2: Schematic representation of an optimized nanoscale resonance optoelectronic sensor based on lessons learned in this dissertation. The three main elements are: an efficient hot hole producing electrode (right), and efficient hot electron producing electrode (left), and a high in-plane mobility transport layer where the electrons and holes recombine.

Bibliography

[1] R. W. Wood. On a remarkable case of uneven distribution of light in a diffraction grating spectrum. *Proceedings of the Physical Society of London*, 18(1):269–275, 1902.

[2] T. W. Ebbesen, H. J. Lezec, H. F. Ghaemi, T. Thio, and P. A. Wolff. Extraordinary optical transmission through sub-wavelength hole arrays. *Nature*, 391:667, 1998.

[3] W. L. Barnes, Alain Dereux, and T. W. Ebbesen. Surface plasmon subwavelength optics. *Nature*, 424:824, 2003.

[4] J. Aizpurua, G. W. Bryant, L. J. Richter, F. J. García de Abajo, B. K. Kelley, and T. Mallouk. Optical properties of coupled metallic nanorods for field-enhanced spectroscopy. *Physical Review B*, 71(23), 2005.

[5] S. Iyer. *Effects of surface plasmons in subwavelength metallic structures*. Thesis, KTH Royal Institute of Technology, 2012.

[6] M. Beruete, I. Campillo, J. S. Dolado, J. E. Rodriguez-Seco, E. Perea, F. Falcone, and M. Sorolla. Very low-profile "bull's eye" feeder antenna. *Antennas and Wireless Propagation Letters*, 4(1):365–368, 2005.

[7] T. Ishi, J. Fujikata, K. Makita, T. Baba, and K. Ohashi. Si nano-photodiode with a surface plasmon antenna. *Japanese Journal of Applied Physics*, 44(No. 12):L364–L366, 2005.

[8] P. Mühlschlegel, H.-J. Eisler, O. J. F. Martin, B. Hecht, and D. W. Pohl. Resonant optical antennas. *Science*, 308(5728):1607–1609, 2005.

[9] G. W. Bryant, F. J. García de Abajo, and J. Aizpurua. Mapping the plasmon resonances of metallic nanoantennas. *Nano Letters*, 8(2):631–636, 2008.

[10] A. G. Curto, G. Volpe, T. H. Taminiau, M. P. Kreuzer, R. Quidant, and N. F. van Hulst. Unidirectional emission of a quantum dot coupled to a nanoantenna. *Science*, 329(5994):930–933, 2010.

[11] O. Sorias, A. Kelrich, R. Gladstone, D. Ritter, and M. Orenstein. Epitaxial nanoflag photonics: Semiconductor nanoemitters grown with their nanoantennas. *Nano Letters*, 17(10):6011–6017, 2017.

[12] P. Bharadwaj, B. Deutsch, and L. Novotny. Optical antennas. *Advances in Optics and Photonics*, 1(3), 2009.

[13] A. Bonakdar. *Far-Field to Near-Field Coupling for Enhancing Light-Matter Interaction*. Thesis, Northwestern University, 2016.

[14] V. Giannini, A. I. Fernández-Domínguez, S. C. Heck, and S. A. Maier. Plasmonic nanoantennas: Fundamentals and their use in controlling the radiative properties of nanoemitters. *Chemical Reviews*, 111(6):3888–3912, 2011.

[15] D. Dregely, R. Taubert, J. Dorfmuller, R. Vogelgesang, K. Kern, and H. Giessen. 3d optical Yagi-Uda nanoantenna array. *Nature Communications*, 2(4):267 (7 pp.), 2011.

[16] J. Kim, Y. Roh, S. Cheon, J. Choe, J. Lee, J. Lee, H. Jeong, U. J. Kim, Y. Park, I. Y. Song, Q. H. Park, S. W. Hwang, K. Kim, and C. Lee. Babinet-inverted optical Yagi–Uda antenna for unidirectional radiation to free space. *Nano Letters*, 14(6):3072–3078, 2014.

[17] T. Kosako, Y. Kadoya, and H. F. Hofmann. Directional control of light by a nano-optical Yagi–Uda antenna. *Nature Photonics*, 4(5):312–315, 2010.

[18] L. Ma, J. Lin, Y. Ma, B. Liu, J. Tan, and P. Jin. Yagi–Uda optical antenna array collimated laser based on surface plasmons. *Optics Communications*, 368:197–201, 2016.

[19] I. S. Maksymov, A. R. Davoyan, A. E. Miroshnichenko, C. Simovski, P. Belov, and Y. S. Kivshar. Multifrequency tapered plasmonic nanoantennas. *Optics Communications*, 285(5):821–824, 2012.

[20] Ivan S. Maksymov, Isabelle Staude, Andrey E. Miroshnichenko, and Yuri S. Kivshar. Optical Yagi-Uda nanoantennas. *Nanophotonics*, 1(1), 2012.

[21] E. G. Mironov, A. Khaleque, L. Liu, I. S. Maksymov, and H. T. Hattori. Enhancing weak optical signals using a plasmonic Yagi-Uda nanoantenna array. *IEEE Photonics Technology Letters*, 26(22):2236–2239, 2014.

[22] X. Y. Xiong, L. J. Jiang, W. E. Sha, Y. H. Lo, and W. C. Chew. Compact nonlinear Yagi-Uda nanoantennas. *Scientific Reports*, 6:18872, 2016.

[23] W. Rieger, J. J. Heremans, H. Ruan, Y. Kang, and R. Claus. Yagi-Uda nanoantenna enhanced metal-semiconductor-metal photodetector. *Applied Physics Letters*, 113(2):023102, 2018.

[24] M. N. Gadalla. *Nano Antenna Integrated Diode (Rectenna) For Infrared Energy Harvesting*. Thesis, King Abdullah University of Science and Technology, 2013.

[25] A. M. Ghanim, M. Hussein, M. F. O. Hameed, A. Yahia, and S. S. A. Obayya. Highly directive hybrid Yagi-Uda nanoantenna for radition emission enhancement. *IEEE Photonics Journal*, 8(5):1–12, Oct 2016.

[26] A. Alu and N. Engheta. Enhanced directivity from subwavelength infrared/optical nano-antennas loaded with plasmonic materials or metamaterials. *IEEE Transactions on Antennas and Propagation*, 55(11):3027–3039, Nov 2007.

[27] W. L. Barnes, T. W. Preist, S. C. Kitson, and J. R. Sambles. Physical origin of photonic energy gaps in the propagation of surface plasmons on gratings. *Physical Review B*, 54(9):6227–6244, 1996.

[28] X. Ni, N. K. Emani, A. V. Kildishev, A. Boltasseva, and V. M. Shalaev. Broadband light bending with plasmonic nanoantennas. *Science*, 335(6067):427, 2012.

[29] S. Ogawa, J. Komoda, K. Masuda, and M. Kimata. Wavelength selective wideband uncooled infrared sensor using a two-dimensional plasmonic absorber. *Optical Engineering*, 52(12):1 – 6, 2013.

[30] C. W. Berry and M. Jarrahi. Principles of impedance matching in photoconductive antennas. *Journal of Infrared, Millimeter, and Terahertz Waves*, 33(12):1182–1189, 2012.

[31] T. A. Milligan. *Modern antenna design*. John Wiley & Sons, 2005.

[32] E. W. Van Stryland, V. N. Mahajan, M. Bass, C. DeCusatis, C. A. MacDonald, and G. Li. *Handbook of optics*. McGraw-Hill, 2010.

[33] F. A. Miranda. Overview of the communications and intelligent systems division at the NASA Glenn Research Center. Published Online, 2019. https://ntrs.nasa.gov/search.jsp?R=20190033428. Retreived 11 March 2020.

[34] H. Chen, A. J. Taylor, and N. Yu. A review of metasurfaces: physics and applications. *Reports on Progress in Physics*, 79(7):076401, 2016.

[35] M. K. Hedayati and M. Elbahri. Review of metasurface plasmonic structural color. *Plasmonics*, 12(5):1463–1479, 2017.

[36] A. Poddubny, I. Iorsh, P. Belov, and Y. Kivshar. Hyperbolic metamaterials. *Nature Photonics*, 7:948, 2013.

[37] P. Li, I. Dolado, F. J. Alfaro-Mozaz, F. Casanova, L. E. Hueso, S. Liu, J. H. Edgar, A. Y. Nikitin, S. Vélez, and R. Hillenbrand. Infrared hyperbolic metasurface based on nanostructured van der Waals materials. *Science*, 359(6378):892–896, 2018.

[38] A. A. High, R. C. Devlin, A. Dibos, M. Polking, D. S. Wild, J. Perczel, N. P. de Leon, M. D. Lukin, and H. Park. Visible-frequency hyperbolic metasurface. *Nature*, 522:192, 2015.

[39] A. J. Hoffman, L. Alekseyev, S. S. Howard, K. J. Franz, D. Wasserman, V. A. Podolskiy, E. E. Narimanov, D. L. Sivco, and C. Gmachl. Negative refraction in semiconductor metamaterials. *Nature Materials*, 6:946, 2007.

[40] S. Yoo, S. Lee, and Q. H. Park. Loss-free negative-index metamaterials using forward light scattering in dielectric meta-atoms. *ACS Photonics*, 5(4):1370–1374, 2018.

[41] W. L. Barnes, T. W. Preist, S. C. Kitson, J. R. Sambles, N. P. K. Cotter, and D. J. Nash. Photonic gaps in the dispersion of surface plasmons on gratings. *Physical Review B*, 51(16):11164–11167, 1995.

[42] A. Sobhani, M. W. Knight, Y. Wang, B. Zheng, N. S. King, L. V. Brown, Z. Fang, P. Nordlander, and N. J. Halas. Narrowband photodetection in the near-infrared with a plasmon-induced hot electron device. *Nature Communications*, 4:1643, 2013.

[43] R. H. Ritchie, E. T. Arakawa, J. J. Cowan, and R. N. Hamm. Surface-plasmon resonance effect in grating diffraction. *Physical Review Letters*, 21(22):1530–1533, 1968.

[44] A. V. Zayats and I. I. Smolyaninov. Near-field photonics: surface plasmon polaritons and localized surface plasmons. *Journal of Optics A: Pure and Applied Optics*, 5(4):S16, 2003.

[45] A. Kramer, F. Keilmann, B. Knoll, and R. Guckenberger. The coaxial tip as a nano-antenna for scanning near-field microwave transmission microscopy. *Micron*, 27(6):413–417, 1996.

[46] L. Langelüddecke, P. Singh, and V. Deckert. Exploring the nanoscale: fifteen years of tip-enhanced raman spectroscopy. *Applied Spectroscopy*, 69(12):1357–1371, 2015.

[47] S. Mukherjee, F. Libisch, N. Large, O. Neumann, L. V. Brown, J. Cheng, J. B. Lassiter, E. A. Carter, P. Nordlander, and N. J. Halas. Hot electrons do the impossible: Plasmon-induced dissociation of H2 on Au. *Nano Letters*, 13(1):240–247, 2013.

[48] P. Christopher, H. Xin, and S. Linic. Visible-light-enhanced catalytic oxidation reactions on plasmonic silver nanostructures. *Nature Chemistry*, 3(6):467, 2011.

[49] R. L. Olmon, B. Slovick, T. W. Johnson, D. Shelton, S. Oh, G. D. Boreman, and M. B. Raschke. Optical dielectric function of gold. *Physical Review B*, 86:235147, Dec 2012.

[50] A. V. Zayats, I. I. Smolyaninov, and A. A. Maradudin. Nano-optics of surface plasmon polaritons. *Physics Reports*, 408(3):131 – 314, 2005.

[51] J. M. Pitarke, V. M. Silkin, E. V. Chulkov, and P. M. Echenique. Theory of surface plasmons and surface-plasmon polaritons. *Reports on Progress in Physics*, 70(1):1–87, 2007.

[52] L. Novotny. Effective wavelength scaling for optical antennas. *Physical Review Letters*, 98(26):266802, 2007.

[53] C. D. Geddes, editor. *Reviews in Plasmonics 2015*. Springer International Publishing, 2016.

[54] M. E. Stewart, C. R. Anderton, L. B. Thompson, J. Maria, S. K. Gray, J. A. Rogers, and R. G. Nuzzo. Nanostructured plasmonic sensors. *Chemical Reviews*, 108(2):494–521, 2008.

[55] A. V. Kabashin, P. Evans, S. Pastkovsky, W. Hendren, G. A. Wurtz, R. Atkinson, R. Pollard, V. A. Podolskiy, and A. V. Zayats. Plasmonic nanorod metamaterials for biosensing. *Nature Materials*, 8(11):867–71, 2009.

[56] J. M. Yi, A. Cuche, E. Devaux, C. Genet, and T. W. Ebbesen. Beaming visible light with a plasmonic aperture antenna. *ACS Photonics*, 1(4):365–370, 2014.

[57] T. H. Johnson. Lead Salt Detectors And Arrays PbS And PbSe. In William L. Wolfe, editor, *Infrared Detectors*, volume 0443, pages 60 – 94. SPIE, 1983.

[58] J. K. Sheu, S. J. Chang, C. H. Kuo, Y. K. Su, L. W. Wu, Y. C. Lin, W. C. Lai, J. M. Tsai, G. C. Chi, and R. K. Wu. White-light emission from near uv ingan-gan led chip precoated with blue/green/red phosphors. *IEEE Photonics Technology Letters*, 15(1):18–20, Jan 2003.

[59] L. Polavarapu, J. Pérez-Juste, Q. Xu, and L. M. Liz-Marzán. Optical sensing of biological, chemical and ionic species through aggregation of plasmonic nanoparticles. *Journal of Matererials Chemistry C*, 2:7460–7476, 2014.

[60] N. A. Rubin, G. D'Aversa, P. Chevalier, Z. Shi, W. T. Chen, and F. Capasso. Matrix fourier optics enables a compact full-stokes polarization camera. *Science*, 365(6448), 2019.

[61] M. W. Knight, H. Sobhani, P. Nordlander, and N. J. Halas. Photodetection with active optical antennas. *Science*, 332(6030):702–704, 2011.

[62] H. A. Atwater and A. Polman. Plasmonics for improved photovoltaic devices. *Nature Materials*, 9(3):205–13, 2010.

[63] J.M. Shannon. Control of schottky barrier height using highly doped surface layers. *Solid-State Electronics*, 19(6):537 – 543, 1976.

[64] P. Bharadwaj, A. Bouhelier, and L. Novotny. Electrical excitation of surface plasmons. *Physical Review Letters*, 106(22):226802, 2011.

[65] S. P. Gurunarayanan, N. Verellen, V. S. Zharinov, F. James Shirley, V. V. Moshchalkov, M. Heyns, J. Van de Vondel, I. P. Radu, and P. Van Dorpe. Electrically driven unidirectional optical nanoantennas. *Nano Letters*, 17(12):7433–7439, 2017.

[66] A. Kabiri, E. Girgis, and F. Capasso. Buried nanoantenna arrays: Versatile antireflection coating. *Nano Letters*, 13(12):6040–6047, 2013.

[67] D. W. Peters, C. M. Reinke, P. S. Davids, J. F. Klem, D. Leonhardt, J. R. Wendt, J. K. Kim, and S. Samora. Nanoantenna-enabled midwave infrared focal plane arrays. In *38th Conference on Infrared Technology and Applications, April 23, 2012 - April 27, 2012*, volume 8353. SPIE, 2012.

[68] L. Yongqian, G. Yongjun, S. Lei, W. Binbin, X. Zheng, and Z. Zili. Plasmonic absorption nanoantenna for frequency selective mid-infrared detection. In *Electro-Optical and Infrared Systems: Technology and Applications X, 23-24 Sept. 2013*, volume 8896, page 88960E (8 pp.). SPIE.

[69] G. N. Malheiros-Silveira and H. E. Hernández-Figueroa. Excitation of metallic coplanar waveguide by dielectric resonator nanoantenna. In *2015 SBMO/IEEE MTT-S International Microwave and Optoelectronics Conference (IMOC)*, pages 1–3.

[70] A. Aubry, D. Y. Lei, A. I. Fernandez-Dominguez, Y. Sonnefraud, S. A. Maier, and J. B. Pendry. Plasmonic light-harvesting devices over the whole visible spectrum. *Nano Letters*, 10(7):2574–9, 2010.

[71] A. S. Jermyn, G. Tagliabue, H. A. Atwater, W. A. Goddard, P. Narang, and R. Sundararaman. Transport of hot carriers in plasmonic nanostructures. *Physical Review Materials*, 3:075201, Jul 2019.

[72] B. Y. Zheng, Y. Wang, P. Nordlander, and N. J. Halas. Color-selective and cmos-compatible photodetection based on aluminum plasmonics. *Advanced Materials*, 26(36):6318–23, 2014.

[73] S. E. El-Zohary, A. A. Azzazi, H. Okamoto, T. Okamoto, M. Haraguchi, and M. A. Swillam. Resonance-based integrated plasmonic nanosensor for lab-on-chip applications. *Journal of Nanophotonics*, 7(1):073077, 2013.

[74] A. G. Brolo. Plasmonics for future biosensors. *Nature Photonics*, 6(11):709, 2012.

[75] T. W. Ebbesen, H. J. Lezec, H. F. Ghaemi, T. Thio, and P. A. Wolff. Extraordinary optical transmission through sub-wavelength hole arrays. *Nature*, 391:667, 1998.

[76] H. F. Ghaemi, T. Thio, D. Grupp, T. W. Ebbesen, and H. J. Lezec. Surface plasmons enhance optical transmission through subwavelength holes. *Physical Review B*, 58(11):6779, 1998.

[77] A. C. Lesina, P. Berini, and L. Ramunno. Origin of third harmonic generation in plasmonic nanoantennas. *Optical Materials Express*, 7(5):1575–1580, 2017.

[78] B. Metzger, M. Hentschel, and H. Giessen. Probing the near-field of second-harmonic light around plasmonic nanoantennas. *Nano Letters*, 17(3):1931–1937, 2017.

[79] E. Aslan and M. Turkmen. Novel dual-band resonator nanoantenna array for infrared detection applications. *Sensors and Materials*, 25(9):653–665, 2013.

[80] Jamie M. Fitzgerald, Sam Azadi, and Vincenzo Giannini. Quantum plasmonic nanoantennas. *Physical Review B*, 95(23):235414, 2017.

[81] A. Wang, P. Hsu, Y. Chen, and J. Cai. Effects of nanoscale features on infrared radiative properties of heavily doped silicon complex gratings. *Science China Technological Sciences*, 53(8):2207–2214, 2010.

[82] S. T. Koev, A. Agrawal, H. J. Lezec, and V. A. Aksyuk. An efficient large-area grating coupler for surface plasmon polaritons. *Plasmonics*, 7(2):269–277, 2011.

[83] L. Li, D. Y. Xiong, Z. Tang, J. Wen, N. Li, P. P. Chen, and Z. Q. Zhu. High efficiency optical coupling in long wavelength quantum cascade infrared detector via quasi-one-dimensional grating plasmonic micro-cavity. *Journal of Applied Physics*, 121(8):083102, 2017.

[84] C. W. Berry, N. Wang, M. R. Hashemi, M. Unlu, and M. Jarrahi. Significant performance enhancement in photoconductive terahertz optoelectronics by incorporating plasmonic contact electrodes. *Nature Communications*, 4:1622, 2013.

[85] T. Hattori, K. Egawa, S. Ookuma, and T. Itatani. Intense terahertz pulses from large-aperture antenna with interdigitated electrodes. *Japanese Journal of Applied Physics*, 45(No. 15):L422–L424, 2006.

[86] S. Lepeshov, A. Gorodetsky, A. Krasnok, E. Rafailov, and P. Belov. Enhancement of terahertz photoconductive antenna operation by optical nanoantennas. *Laser and Photonics Reviews*, 11(1), 2017.

[87] S. Lepeshov, A. Gorodetsky, A. Krasnok, N. Toropov, T. A. Vartanyan, P. Belov, A. Alú, and E. U. Rafailov. Boosting terahertz photoconductive antenna performance with optimised plasmonic nanostructures. *Scientific Reports*, 8(1):1–7, 2018.

[88] G. Matthäus, S. Nolte, R. Hohmuth, M. Voitsch, W. Richter, B. Pradarutti, S. Riehemann, G. Notni, and A. Tünnermann. Microlens coupled interdigital photoconductive switch. *Applied Physics Letters*, 93(9):091110, 2008.

[89] S. S. Mousavi, P. Berini, and A. Stohr. Surface plasmon nanoantenna-based photodetector with terahertz electrical bandwidth. In *2014 International Topical Meeting on Microwave Photonics, MWP 2014 and the 9th Asia-Pacific Microwave Photonics Conference, APMP 2014, October 20, 2014 - October 23, 2014*, pages 427–429. Institute of Electrical and Electronics Engineers Inc.

[90] S. Winnerl. Scalable microstructured photoconductive terahertz emitters. *Journal of Infrared, Millimeter, and Terahertz Waves*, 33(4):431–454, 2011.

[91] N. T. Yardimci and M. Jarrahi. 3.8 mw terahertz radiation generation through plasmonic nano-antenna arrays. In *2015 IEEE International Symposium on Antennas and Propagation & USNC/URSI National Radio Science Meeting*, pages 2113–2114.

[92] N. T. Yardimci and M. Jarrahi. High sensitivity terahertz detection through large-area plasmonic nano-antenna arrays. *Scientific Reports*, 7:42667, 2017.

[93] R. Zhang, X. G. Guo, C. Y. Song, M. Buchanan, Z. R. Wasilewski, J. C. Cao, and H. C. Liu. Metal-grating-coupled terahertz quantum-well photodetectors. *IEEE Electron Device Letters*, 32(5):659–661, 2011.

[94] F. F. Masouleh, N. Das, and H. R. Mashayekhi. Assessment of amplifying effects of ridges spacing and height on nano-structured msm photo-detectors. *Optical and Quantum Electronics*, 47(2):193–201, 2014.

[95] F. F. Masouleh, N. Das, and H. R. Mashayekhi. Optimization of light transmission efficiency for nano-grating assisted msm-pds by varying physical parameters. *Photonics and Nanostructures - Fundamentals and Applications*, 12(1):45–53, 2014.

[96] S. Piltan and D. Sievenpiper. Optical rectification using geometrical field enhancement in gold nano-arrays. *Journal of Applied Physics*, 122(18), 2017.

[97] Z. Yu, G. Veronis, S. Fan, and M. L. Brongersma. Design of midinfrared photodetectors enhanced by surface plasmons on grating structures. *Applied Physics Letters*, 89(15), 2006.

[98] R. Grote, R. M. Osgood, J. E. Spanier, and B. Nabet. Optimization of a surface plasmon enhanced metal-semiconductor-metal photodetector on gallium arsenide. In *Frontiers in Optics 2010/Laser Science XXVI*. Optical Society of America, 2010.

[99] S. Campione, L. K. Warne, R. E. Jorgenson, P. S. Davids, and D. W. Peters. Simulations of realistic multifunctional nanoantenna enabled detectors. In *2017 International Applied Computational Electromagnetics Society Symposium - Italy (ACES)*, pages 1–2, March 2017.

[100] W. Hsu, H. Ling, S. Wang, and C. Lee. Characteristics of surface plasmon coupled quantum well infrared photodetectors. *Journal of Applied Physics*, 121(24):244503, 2017.

[101] H. Sobhani Khakestar. *Plasmonic Manipulation of Light for Sensing and Photovoltaic Applications*. Thesis, Rice University, 2012.

[102] M. W. Knight, L. Liu, Y. Wang, L. Brown, S. Mukherjee, N. S. King, H. O. Everitt, P. Nordlander, and N. J. Halas. Aluminum plasmonic nanoantennas. *Nano Letters*, 12(11):6000–4, 2012.

[103] B. K. Singh and A. C. Hillier. Surface plasmon resonance enhanced transmission of light through gold-coated diffraction gratings. *Analytical Chemistry*, 80(10):3803–3810, 2008.

[104] V. M. Shalaev, C. Douketis, J. T. Stuckless, and M. Moskovits. Light-induced kinetic effects in solids. *Physical Review B*, 53(17):11388–11402, 1996.

[105] P. R. Berger. Metal-semiconductor-metal photodetectors. In Aland K. Chin, Niloy K. Dutta, Kurt J. Linden, S. C. Wang, S. C. Wang, and Niloy K. Dutta, editors, *Testing, Reliability, and Applications of Optoelectronic Devices*, volume 4285, pages 198 – 207. International Society for Optics and Photonics, SPIE, 2001.

[106] L. Novotny and N. van Hulst. Antennas for light. *Nature Photonics*, 5(2):83–90, 2011.

[107] P. Yla-Oijala, D. C. Tzarouchis, E. Raninen, and A. Sihvola. Characteristic mode analysis of plasmonic nanoantennas. *IEEE Transactions on Antennas and Propagation*, 65(5):2165–2172, 2017.

[108] E. J. Zeman and G. C. Schatz. An accurate electromagnetic theory study of surface enhancement factors for silver, gold, copper, lithium, sodium, aluminum, gallium, indium, zinc, and cadmium. *The Journal of Physical Chemistry*, 91(3):634–643, 1987.

[109] M. Lahav, A. Vaskevich, and I. Rubinstein. Biological sensing using transmission surface plasmon resonance spectroscopy. *Langmuir*, 20(18):7365–7367, 2004.

[110] S. Choi and K. Sarabandi. Efficient nanoantenna simulation for IR energy harvesting and detection devices. In *31st General Assembly and Scientific Symposium of the International Union of Radio Science, URSI GASS 2014, August 16, 2014 - August 23, 2014*. Institute of Electrical and Electronics Engineers Inc.

[111] P. B. Johnson and R. W. Christy. Optical constants of the noble metals. *Physical Review B*, 6:4370–4379, Dec 1972.

[112] D. T. Pierce and W. E. Spicer. Electronic structure of amorphous si from photoemission and optical studies. *Physical Review B*, 5:3017–3029, Apr 1972.

[113] J. D. Jackson. *Classical Electrodynamics, 3rd Edition*. John Wiley & Sons, 1962.

Appendix A

Surface Plasmon Polariton Derivation

The ensuing discussion of Surface Plasmon Polaritons is heavily inspired from the seminal reports Zayats *et al.* [50] and Pitarke *et al.* [51].

For TM polarized incident light we have in the dielectric ($z > 0$):

$$\vec{H}_d = \begin{pmatrix} 0 \\ H_{dy} \\ 0 \end{pmatrix} e^{ikx - \kappa_z^{(d)} z - i\omega t} \tag{A.1}$$

and

$$\vec{E}_d = \begin{pmatrix} E_{dx} \\ 0 \\ E_{dz} \end{pmatrix} e^{ikx - \kappa_z^{(d)} z - i\omega t} \tag{A.2}$$

in the metal ($z < 0$):

$$\vec{H}_m = \begin{pmatrix} 0 \\ H_{my} \\ 0 \end{pmatrix} e^{ikx + \kappa_z^{(m)} z - i\omega t} \tag{A.3}$$

and

$$\vec{E}_m = \begin{pmatrix} E_{mx} \\ 0 \\ E_{mz} \end{pmatrix} e^{ikx + \kappa_z^{(m)} z - i\omega t} \tag{A.4}$$

Applying Ampere's Law:

$$\nabla \times \vec{H} = \epsilon \frac{1}{c^2} \frac{\partial \vec{E}}{\partial t} \tag{A.5}$$

$$\nabla \times \vec{H}_d = \begin{pmatrix} -\kappa \\ 0 \\ ik \end{pmatrix} H_{dy} e^{ikx - \kappa_z^{(d)} z - i\omega t} \tag{A.6}$$

$$\nabla \times \vec{H}_m = \begin{pmatrix} -\kappa \\ 0 \\ ik \end{pmatrix} H_{my} e^{ikx + \kappa_z^{(m)} z - i\omega t} \tag{A.7}$$

$$\frac{\partial \vec{E}_d}{\partial t} = -i\omega \begin{pmatrix} E_{dx} \\ 0 \\ E_{dz} \end{pmatrix} e^{ikx - \kappa_z^{(d)} z - i\omega t} \tag{A.8}$$

$$\frac{\partial \vec{E}_m}{\partial t} = -i\omega \begin{pmatrix} E_{mx} \\ 0 \\ E_{dz} \end{pmatrix} e^{ikx - \kappa_z^{(m)} z - i\omega t} \tag{A.9}$$

Then

$$\begin{pmatrix} E_{dx} \\ 0 \\ E_{dz} \end{pmatrix} = \begin{pmatrix} -\kappa_z^{(d)} \\ 0 \\ ik \end{pmatrix} \frac{H_{dy} c^2}{i\omega\epsilon} \tag{A.10}$$

$$\begin{pmatrix} E_{mx} \\ 0 \\ E_{mz} \end{pmatrix} = \begin{pmatrix} \kappa_z^{(m)} \\ 0 \\ ik \end{pmatrix} \frac{H_{my} c^2}{i\omega\epsilon} \tag{A.11}$$

Requiring a solution to the wave equation:

$$\nabla^2 \vec{E} = \frac{\epsilon}{c^2} \frac{\partial^2 \vec{E}}{\partial t^2} \tag{A.12}$$

Gives:

$$\kappa_z^{(d)} = \sqrt{k - \epsilon^{(d)} \frac{\omega^2}{c^2}} \tag{A.13}$$

$$\kappa_z^{(m)} = \sqrt{k - \epsilon^{(m)}(\omega) \frac{\omega^2}{c^2}} \tag{A.14}$$

Applying Boundary Conditions:

$$H_{dy}\frac{\kappa_z^{(d)}}{\epsilon^{(d)}} + H_{my}\frac{\kappa_z^{(m)}}{\epsilon^{(m)}(\omega)} = 0 \tag{A.15}$$

and

$$H_{dy} - H_{my} = 0 \tag{A.16}$$

And requiring a non trivial solution:

$$\begin{vmatrix} -1 & 1 \\ \frac{\kappa_z^{(d)}}{\epsilon^{(d)}} & \frac{\kappa_z^{(m)}}{\epsilon^{(m)}(\omega)} \end{vmatrix} = 0 \tag{A.17}$$

Gives:

$$\frac{\kappa_z^{(d)}}{\epsilon^{(d)}} + \frac{\kappa_z^{(m)}}{\epsilon^{(m)}(\omega)} = 0 \tag{A.18}$$

Finally:

$$k = k_0\sqrt{\frac{\epsilon^{(d)}\epsilon^{(m)}(\omega)}{\epsilon^{(d)} + \epsilon^{(m)}(\omega)}} \tag{A.19}$$

Or in terms of wavelength:

$$\lambda_{SP} = \lambda_0\sqrt{\frac{\epsilon^{(d)} + \epsilon^{(m)}(\omega)}{\epsilon^{(d)}\epsilon^{(m)}(\omega)}} \tag{A.20}$$

Appendix B

Mathematica® Source

```
Plot [{Sqrt[1 + 2 k^2 - Sqrt[1 + 4 k^4]]/Sqrt[2], 1/Sqrt[2]}, {k, 0,
  4}, PlotRange -> Full,
 PlotLegends -> {"SPP on Bulk Material",
   "\[Omega]=\[Omega]p/(1-\!\(\*SuperscriptBox[\(\[Epsilon]\), \
\((1)\)]\)\!\(\*SuperscriptBox[\()\), \(1/2\)]\)"},
 AxesLabel -> {"\!\(\*FractionBox[\(k\\\\c\), \(\[Omega]p\)]\)",
   "\[Omega]/\[Omega]p"}, PlotStyle -> {Thickness[0.008]}]
Plot [{Sqrt[1 + 2 k^2 - Sqrt[1 + 4 k^4]]/Sqrt[2], Sqrt[
  12 + 13 k^2 - Sqrt[144 + 264 k^2 + 169 k^4]]/(2 Sqrt[6]), 1/Sqrt[2],
   1/Sqrt[13]}, {k, 0, 4}, PlotRange -> Full,
 PlotLegends -> {"SPP Above Thin Film", "SPP Below Thin Film",
   "\[Omega]=\[Omega]p/(1+\!\(\*SuperscriptBox[\(\[Epsilon]\), \
\((1)\)]\)\!\(\*SuperscriptBox[\()\), \(1/2\)]\)",
   "\[Omega]=\[Omega]p/(1+\!\(\*SuperscriptBox[\(\[Epsilon]\), \
\((s)\)]\)\!\(\*SuperscriptBox[\()\), \(1/2\)]\)"},
 AxesLabel -> {"\!\(\*FractionBox[\(k\\\\c\), \(\[Omega]p\)]\)",
   "\[Omega]/\[Omega]p"}, PlotStyle -> {Thickness[0.008]}]
Plot [{\[Lambda] Sqrt[(2 - ((2.15*10^6 \[Lambda])/( 3 10^8))^2)/(
   1 - ((2.15*10^6 \[Lambda])/( 3 10^8))^2)], \[Lambda] Sqrt[(
   2 - ((2.911*10^6 \[Lambda])/( 3 10^8))^2)/(
   1 - ((2.911*10^6 \[Lambda])/( 3 10^8))^2)]}, {\[Lambda], 200, 800},
  AxesLabel -> {"\[Lambda]",
   "\!\(\*SubscriptBox[\(\[Lambda]\), \(SP\)]\)"},
 PlotLegends -> {"Au-Air", "Al-Air"},
 PlotStyle -> {Thickness[0.008]}]
Plot [{\[Lambda] Sqrt[(2 - ((2.15*10^6 \[Lambda])/( 3 10^8))^2)/(
   1 - ((2.15*10^6 \[Lambda])/( 3 10^8))^2)], \[Lambda] Sqrt[(
   1.5^2 + 1 - ((2.15*10^6 \[Lambda])/(
```

```
     3 10^8))^2)/((1 - ((2.15*10^6 \[Lambda])/(
       3 10^8))^2) 1.5^2)]}, {\[Lambda], 200, 800},
 AxesLabel -> {"\[Lambda]",
   "\!\(\*SubscriptBox[\(\[Lambda]\), \(SP\)]\)"},
 PlotLegends -> {"Air-Au", "Glass-Au"},
 PlotStyle -> {Thickness[0.008]}]
Plot [{f[k], F[k], 1/Sqrt[2], 1/Sqrt[13]}, {k, 0, 4},
 PlotRange -> Full,
 PlotLegends -> {"SPP Above Thin Film", "SPP Above Thin Film",
   "\[Omega]=\[Omega]p/(1+\!\(\*SuperscriptBox[\(\[Epsilon]\), \
\((1)\)]\)\!\(\*SuperscriptBox[\()\), \(1/2\)]\)",
   "\[Omega]=\[Omega]p/(1+\!\(\*SuperscriptBox[\(\[Epsilon]\), \
\((s)\)]\)\!\(\*SuperscriptBox[\()\), \(1/2\)]\)"},
 AxesLabel -> {"\!\(\*FractionBox[\(k\\\\c\), \(\[Omega]p\)]\)",
   "\[Omega]/\[Omega]p"}]
Plot [{\[Lambda] Sqrt[(2 - ((2.15*10^6 \[Lambda])/( 3 10^8))^2)/(
   1 - ((2.15*10^6 \[Lambda])/( 3 10^8))^2)], \[Lambda] Sqrt[(
   2 - ((2.911*10^6 \[Lambda])/( 3 10^8))^2)/(
   1 - ((2.911*10^6 \[Lambda])/( 3 10^8))^2)]}, {\[Lambda], 1540,
  1560}, AxesLabel -> {"\[Lambda]",
   "\!\(\*SubscriptBox[\(\[Lambda]\), \(SP\)]\)"},
 PlotLegends -> {"Au", "Al"},
 GridLines -> {{{1550, Red}}, {{1546.55, Red}, {1543.66, Red}}}]
Plot [{\[Lambda] Sqrt[(2 - ((2.15*10^6 \[Lambda])/( 3 10^8))^2)/(
   1 - ((2.15*10^6 \[Lambda])/( 3 10^8))^2)], \[Lambda] Sqrt[(
   2.2^2 + 1 - ((2.15*10^6 \[Lambda])/(
     3 10^8))^2)/((1 - ((2.15*10^6 \[Lambda])/(
       3 10^8))^2) 2.2^2)]}, {\[Lambda], 1540, 1560},
 AxesLabel -> {"\[Lambda]",
   "\!\(\*SubscriptBox[\(\[Lambda]\), \(SP\)]\)"},
 PlotLegends -> {"Air", "PDDA"}]
Plot [{\[Lambda] Sqrt[(2 - ((2.15*10^6 \[Lambda])/( 3 10^8))^2)/(
   1 - ((2.15*10^6 \[Lambda])/( 3 10^8))^2)], \[Lambda] Sqrt[(
   2 - ((2.911*10^6 \[Lambda])/( 3 10^8))^2)/(
   1 - ((2.911*10^6 \[Lambda])/( 3 10^8))^2)]}, {\[Lambda], 200,
  2000}, AxesLabel -> {"\[Lambda] (nm)",
   "\!\(\*SubscriptBox[\(\[Lambda]\), \(SP\)]\) (nm)"},
 PlotLegends -> {"Au-Air", "Al-Air"},
 PlotStyle -> {Thickness[0.008]}]
Plot [{\[Lambda] Sqrt[(2 - ((2.15*10^6 \[Lambda])/( 3 10^8))^2)/(
   1 - ((2.15*10^6 \[Lambda])/( 3 10^8))^2)], \[Lambda] Sqrt[(
   1.5^2 + 1 - ((2.15*10^6 \[Lambda])/(
```

```
    3 10^8))^2)/((1 - ((2.15*10^6 \[Lambda])/(
      3 10^8))^2) 1.5^2)], \[Lambda] Sqrt[(
  2.2^2 + 1 - ((2.15*10^6 \[Lambda])/(
    3 10^8))^2)/((1 - ((2.15*10^6 \[Lambda])/(
      3 10^8))^2) 2.2^2)]}, {\[Lambda], 200, 2000},
AxesLabel -> {"\[Lambda](nm)",
  "\!\(\*SubscriptBox[\(\[Lambda]\), \(SP\)]\) (nm)"},
PlotLegends -> {"Air-Au", "Glass-Au", "PDDA-Au"},
PlotStyle -> {Thickness[0.008]}]
```

Appendix C

Mask Designs

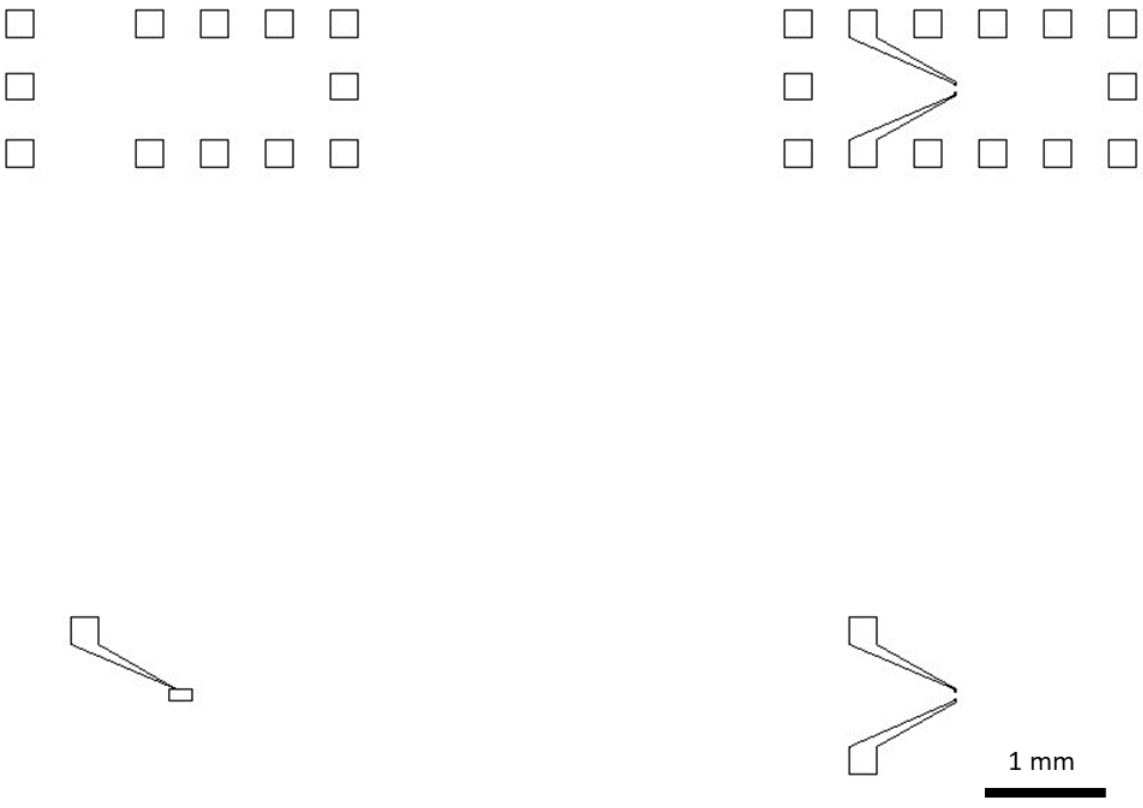

Figure C.1: Outline of photolithography mask used to define macroscopic electrodes. The area outside the closed polygons is shaded with an opaque material, and a positive photolithography procedure is used with this mask. The outline in the bottom right corner is the outline used for the devices discussed in this dissertation.

Figure C.2: The outline used with NPGS software to perform the alignment between macroscopic electrodes and nanoscale features, as described in Chapter 2.

Figure C.3: The pattern used with NPGS and E-beam lithography to expose the Yagi-Uda array on the device as discussed in Chapter 2.